AD NUMBER
AD818693
LIMITATION CHANGES
TO: **Approved for public release; distribution is unlimited.**
FROM: **Distribution authorized to U.S. Gov't. agencies and their contractors; Critical Technology; JUN 1967. Other requests shall be referred to Air Force Institute of Technology, Attn: AFIT-SE, Wright-Patterson AFB, OH 45433. This document contains export-controlled technical data.**
AUTHORITY
AFIT ltr, 22 Jul 1971

AD818693

AIR FORCE INSTITUTE OF TECHNOLOGY

AF INSTITUTE OF TECHNOLOGY

AIR UNIVERSITY
UNITED STATES AIR FORCE

SCHOOL OF ENGINEERING

WRIGHT-PATTERSON AIR FORCE BASE, OHIO

DISCLAIMER NOTICE

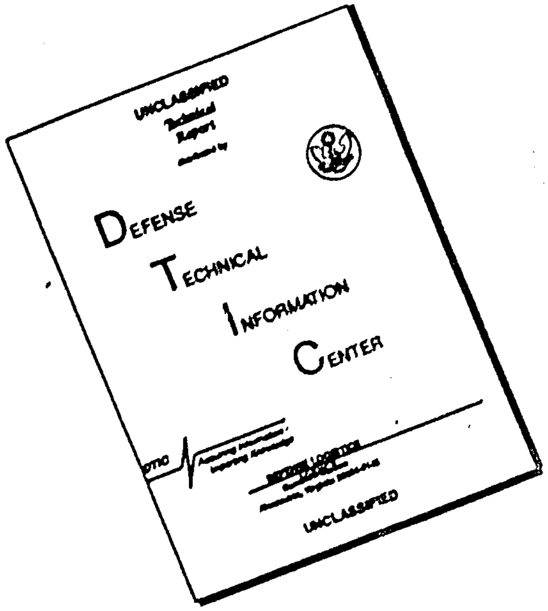

THIS DOCUMENT IS BEST QUALITY AVAILABLE. THE COPY FURNISHED TO DTIC CONTAINED A SIGNIFICANT NUMBER OF PAGES WHICH DO NOT REPRODUCE LEGIBLY.

FLOW FIELD, DRAG, AND HEAT TRANSFER
OF A HEATED CYLINDER
IN A SUBSONIC CROSSFLOW OF AIR

THESIS

GAM/ME/67-10 Jerome R. Jarcy
Capt USAF

AFLC-WPAFB-AUG 67 35

FLOW FIELD, DRAG, AND HEAT TRANSFER
OF A HEATED CYLINDER
IN A SUBSONIC CROSSFLOW OF AIR

THESIS

Presented to the Faculty of the School of Engineering of
the Air Force Institute of Technology
Air University
in Partial Fulfillment of the
Requirements for the Degree of
Master of Science

By

Jerome R. Jarcy, B.S. M.E.
Capt USAF

Graduate Aeronautical - Mechanical Engineering

June 1967

Preface

This report is the result of an investigation suggested by Dr. Ward C. Roman, Thermo-Mechanics Laboratory, Aerospace Research Laboratory.

A large amount of data obtained during preliminary testing has been excluded, because the cylinder used failed before a complete set of data was taken. The author hopes the results and appendices contained herein indicate the direction for further study.

I extend my appreciation to Mr. Franz Huber of the Flight Dynamics Laboratory, who designed the inlet for the wind tunnel. I also thank my faculty advisor, Dr. Harold E. Wright, the faculty of the Mechanical Engineering Department, and Mr. Erick E. Soehngen, Director, Thermo-Mechanics Laboratory, Aerospace Research Laboratories.

Many of the devices used in this study were made during the preliminary tests. To this end, the assistance of the technicians in the Thermo-Mechanics Laboratory is gratefully acknowledged.

Jerome R. Jarcy

Contents

Contents

List of Figures

Figure		Page

List of Symbols

Symbol	Quantity	Units
C	total drag coefficient	
c	calibration constant	
d	diameter	inches
D	drag	lbf
E	voltage	volts
F	force	lbf
I	current	amperes
L	length of cylinder	inches
M	momentum flux	lbm-ft/sec^2
$\overline{Nu}$	Nusselt Number	
P	pressure	inches H_2O
P_a	atmospheric pressure	inches Hg
q	dynamic pressure	inches H_2O
$\overline{R}$	universal gas constant	ft-lbf/lbm-^oR
R	resistance	ohms
Re	Reynold's Number	
T	temperature	^oF
V	velocity	ft/sec
x	distance normal to free-stream flow	inches
y	distance parallel to free-stream flow	inches
β	blockage correction factor	
ϵ	emmisivity	
θ	pitch angle	degrees

Symbol	Quantity	Units
μ	viscosity	lbm/ft-sec
σ	Stefan-Botlzmann constant	Btu/hr-ft^2 $^oR^4$
τ	shear stress	lbf/inch^2

Subscripts

a	atmospheric
c	corrected
cyl	cylinder
d	drag
f	film
p	pressure
s	static
t	total
w	wall
x	normal to free-stream flow
y	parallel to free-stream flow
∞	free stream

Abstract

In this study flow field, drag and heat transfer characteristics of a mica cylinder heated by nichrome ribbon were investigated. Measurements were performed in a wind tunnel at velocities of 40 to 160 fps, and at heat input rates of zero to 188 Btu/hr-inch^2. Average cylinder surface temperatures ranged from 250°F to 1100°F above atmospheric temperature. Cylinder surface pressure distributions indicate the flow is subcritical and separation is laminar. Pressure drag was satisfactorily calculated from cylinder pressure distributions. Total and dynamic pressure distributions in the wake showed an increased depression with increased rate of heat input. Heat transfer data correlated satisfactorily with Douglas and Churchill.

FLOW FIELD, DRAG, AND HEAT TRANSFER OF A HEATED CYLINDER IN A SUBSONIC CROSSFLOW OF AIR

I. Introduction

In this study the drag, surrounding flow field, and heat transfer of a moderately heated cylinder in a subsonic crossflow of air were investigated. The diagnostic studies of the flow field include total and dynamic pressure profiles upstream and downstream of the cylinder, and circumferential temperature and pressure distributions around the cylinder. The drag and heat transfer were determined by evaluation of pressure and temperature measurements on and about a hollow mica cylinder uniformly wrapped with nichrome ribbon. The cylinder is oriented vertically in a horizontal wind tunnel (six-inch-by-eight-inch cross section) with the axis of the cylinder normal to the airflow (crossflow). Tests were performed at low subsonic velocities, and the flow was considered incompressible.

Background

This study was performed for three reasons. First, data concerning the variation of drag with cylinder temperature could not be found in the literature (Ref 31:32). Because of this, speculation exists that the drag of a heated cylinder may change as the surface temperature is increased beyond a certain undetermined limit. Second,

the flow field around a heated cylinder is of interest because of the similarity of the wake of a heated cylinder to an electric arc. Roman and Meyers obtained downstream velocity profiles for an electric arc and for four bluff bodies. They found that the velocity profile behind an electric arc was closer to the velocity profile behind a heated cylinder than for other bluff bodies (Ref 31:32-37). Third, there is a possible application of drag and flow field data of a cylinder in a heat exchanger. If the drag decreases when the cylinder is heated beyond a certain limit, this may result in increased efficiency. Information on the wake width may also indicate at what position downstream another cylinder could be most effectively located.

Previous investigations were limited to the study of drag and surrounding flow field near ambient temperatures (Ref 32:16,19). Pressure distributions around the circumference of a heated cylinder are given by several references (Ref 9:161;32:19). One previous investigation by Van Der Hegge Zijnen notes an explanation by Goukman, et al, that the increase in rate of heat transfer was due to a correspondingly increased drag coefficient (Ref 41:206). Likewise, Reynolds' analogy for a flat plate shows that skin friction increases with an increase in rate of heat transfer. A few other investigations have been performed with nichrome ribbon wound about cylinders, but temperature differences were small ($\leq 100^{o}F$) (Ref 12,13).

Objectives

The overall objective of this investigation was to obtain drag, flow field, and heat transfer data for a highly heated cylinder, i.e., at temperatures approaching 2500°F. The specific objectives were:

1. To modify an existing wind tunnel and develop the test apparatus and instrumentation.
2. To evaluate cylinder specimens.
3. To determine characteristics (velocity profiles) of the wake at different velocities and rates of heating.
4. To determine whether drag increases or decreases with an increase in rate of heating.

Theoretical Considerations

The theoretical basis for this study consists of a heat balance on the cylinder and an impulse-momentum balance on a control volume containing the cylinder.

A heat balance on the cylinder can be written as follows: (ohmic heat generated by current I) = (heat convected to airstream)+(heat radiated to tunnel walls)+(heat lost by axial conduction along cylinder to tunnel walls)+ (heat lost by free convection from inner walls of cylinder)

A schematic diagram of the forces and momentum fluxes in a control volume containing the cylinder is shown in Appendix E. The governing equation is (Summation of forces parallel to the stream) = (Change in momentum of the air-

flow per unit time) or, simply,

$$\Sigma F_y = \Delta M$$

where F is a force and M is the momentum flux. After substituting total, static, and dynamic pressure forces, the governing equation may be reduced to

$$\frac{F_{cyl}}{L} = \Sigma(P_{t1}-P_a)\,\Delta x - \Sigma(P_{t2}-P_a)\,\Delta x + \Sigma(q_1-q_2)\,\Delta x$$

where the terms on the right side of the equation contain only total, atmospheric and dynamic pressures.

II. Apparatus and Instrumentation

The wind tunnel, test cylinders used, their mounting, and probes used are discussed in this section. Power supply and instrumentation are discussed in Appendix I.

Wind Tunnel

The wind tunnel consists of the inlet section, test section, diffuser, and blower as shown in Figure H-1. The blower "pulls" air through the inlet past the test section. After passing the test section, the air enters the diffuser and the blower respectively. The blower then expels the air to the atmosphere outside the laboratory through a vertical duct. Additional description of the wind tunnel is in Appendix M.

Test Cylinders

The test cylinders were hollow tubes formed of mica and wrapped with nichrome ribbon (Figs H-5, H-6, and H-7). The mica cylinders (commercially procured) were formed by rolling a thin continuous sheet of mica on a cylindrical spindle. A thin coating of shellac was simultaneously applied.

At mid-length of each cylinder four thermocouples (iron-constantan, diameter = 0.010 inches) and one pressure tap (diameter = 0.059 inches) were inserted through the cylinder wall (Fig H-12). The four thermocouple junctions were laid on the outer surface of the mica cylinders at

90 degree intervals around the circumference. The pressure tap was inserted in the cylinder surface directly above one of the thermocouple junctions. The nichrome ribbon (Ni-Chrome V produced by the Driver Harris Co.) was wound around the cylinder in a spiral. The ribbon pressed the thermocouple junctions against the mica in this manner. As the helix of nichrome ribbon approached the ends of the cylinder, the ribbon was wound at greater intervals (Fig H-6). This decreased the number of turns of ribbon per inch and helped prevent heat buildup at the tunnel walls.

Three different cylinders were used. They were designated cylinders A, B, and C and were respectively 0.497, 0.64, and 1.05 inches in diameter. Cylinder B was used in preliminary testing, and cylinders A and C provided the test data contained in this study.

Cylinder Mounting

Figures H-8 through H-11 indicate the method for mounting the cylinders in the wind tunnel walls. Figures H-4 and H-5 shows cylinder A mounted in the tunnel. Figures H-10 and H-11 are sketches depicting the mounting technique that allowed use of different size cylinders and permitted cylinder rotation. Any size cylinder up to the maximum inner diameter of the bearing could be used with an appropriate Teflon bushing.

Probes

An aspirating probe, a five-hole pressure probe, and

a three-hole pressure probe with an internally contained thermocouple were used. The aspirating probe was designed and constructed in anticipation of high temperature measurements. It is discussed in Appendix A. The five-hole and three-hole probes were used together for preliminary testing, one upstream and one downstream of the cylinder. After considerable testing, a velocity difference of 3% was determined between the two so use of the five hole probe was discontinued.

The primary flow measuring device was the three-hole pressure probe supplied by the United Sensor and Control Corporation. Figures H-16 and H-17 show construction and hookup of the probe. Figure C-1 is a copy of the calibration curves furnished by the company. Figure H-14 shows mounting of the probe, the traversing mechanism, and the mechanism to change yaw angle. Additional information is in Appendices J and K.

III. Experimental Procedure

Experimental procedure and fixed test parameters are discussed in this section. Preliminary tests using cylinder B are discussed in Appendix C.

Testing of cylinders A and C was performed with electrical current (I) set at zero, approximately 4.1 amperes and approximately 6.15 amperes (Table I). For each current flow, tests were run at 40, 80, 120 and 160 fps.

Probing stations used were one upstream (Hole C), and three downstream (Fig 1). For both cylinders, the first downstream probe station was located just outside the area of flow reversal behind the cylinder. For cylinder A, downstream probe stations were 3.23, 6.76, and 12.8 diameters downstream of cylinder centerline. For cylinder C, downstream probe stations were 3.63, 5.59, and 7.01 diameters downstream.

The actual test procedure was as follows. First, the cloth inlet was cleaned daily with a vacuum cleaner. The butterfly valve on the blower was set to the approximate desired velocity, usually the lowest, and the blower was turned on. The three-hole probe was inserted in probe station C (Fig H-14) with the pressure openings at the tunnel centerline in order to determine exact tunnel speed. In early tests current was supplied to the nichrome ribbon 15 minutes after start; in later tests (particularly at the highest amperage) current was supplied to the nichrome ribbon when the blower was started in order to hasten

stabilization of cylinder temperature. The cylinder pressure tap was rotated to the forward stagnation point of the cylinder, so the thermocouples were located at 90^{o} interval from the stagnation point (Fig H-12). Recording of data was begun in one-half to one hour after starting tunnel. Barometric pressure, inlet temperature, voltage and amperage through the nichrome, and the four cylinder thermocouple temperatures, were monitored throughout the run.

Pressures indicated by the three-hole probe were recorded from the three manometers (Fig H-17). The manometer pressure difference, P_2-P_3, was zeroed within an indication of $\pm$0.20 inches H_2O ($\pm$.05 inches H_2O actual pressure) on the 15-degree slant manometer by changing the yaw angle of the probe. The other two manometers were checked every ten seconds for a change of 0.01 inches H_2O indicated on the 15-degree slant manometer. This is actually less than 0.0025 inches H_2O on a vertical manometer. When these two manometers were stable, simultaneous readings of the three manometers and of the Honeywell temperature recorder were taken. The probe was then moved to the next position. Measurements were taken at three points close to the wall and at three points near the geometric centerline of the tunnel to determine minimum points in the wake. Six other measurements were taken at other points to define the rest of the pressure curve. After traversing all four stations, the cylinder was rotated. Readings of the four thermocouples on the cylinder

and the surface pressure were taken at 10 or 15 degree increments. Once the cylinder pressure characteristics were determined, readings were taken at 30 degree increments. At the end of these measurements, the three-hole probe was re-inserted in probe station C at the centerline and its pressures re-recorded. Midway in the probe traverses, and at the end of all runs, barometric pressure, inlet temperature, cylinder temperature, amperage, and voltage were recorded.

IV. Discussion of Results

The results discussed in this section are the momentum calculations, cylinder surface pressure distributions, and pressure drag coefficient. The dynamic and total pressure distributions of both cylinders A and C are discussed and compared. Heat transfer correlation is contained in Appendix G. Probe errors are discussed in Appendix K.

Momentum Calculations

The drag, D, on the cylinder was computed using the equation:

$$\frac{D_{cyl}}{L} = \frac{F_{cyl}}{L} = \Sigma(P_{t1}-P_a)\,\Delta x - \Sigma(P_{t2}-P_a)\,\Delta x + \Sigma(q_1 q_2)\,\Delta x$$

Derivation is in Appendix E. For the summations a planimeter was used to measure the areas of each of the total and dynamic pressure curves in Appendix F. The coefficient of drag, C_d, was computed from the relationship:

$$C_d = \frac{F_{cyl}/L}{q\ d}$$

where q is dynamic pressure as measured upstream at the tunnel centerline, and d is cylinder diameter.

Calculation of C_d by the momentum deficit method gave coefficients ranging from effectively zero to approximately one. Since C_d is approximately 1.15 in the Reynold's number range tested, the results of these calculated are obviously in error and are not listed in this

report. The coefficient for cylinder A increased (in most cases) with distance downstream of the cylinder, but no definite trend was noticed with cylinder C. The fact that cylinder C had twice the blockage area as cylinder A may have given rise to doubtful pressure readings by the probe. The value of C_d for cylinder A at 12.8 diameters downstream averaged about 0.5. Considering that the rate of increase of C_d diminishes slightly as the flow proceeds downstream, it is estimated that probing at least 30 diameters downstream may possibly give a proper drag coefficient.

A possible explanation for the inability to measure drag by the momentum deficit is based on the fact that a large part of the drag is caused by rotational losses (vorticity). Pope states that drag caused by rotational losses does not appear as a loss in linear momentum in the flow direction (Ref 29:168). He further restricts his statement to stalled airfoils or airfoils with flaps down, which implies that it is impossible to measure the drag of any body which causes the flow to separate and become rotational. Robinson supports this conclusion when he refers to a cylinder as a "blunt" body (Ref 30:62). Unfortunately, this study was initially based on the method given by Schlichting (Ref 32:Ch 25), who makes no mention of restrictions to his method. He does, however, limit his figures and examples to airfoil shapes. The general conclusion is that drag cannot be measured by the momentum method for bluff bodies, except possibly at large distances

downstream.

Cylinder Surface Pressure Distributions

A typical circumferential pressure distribution curve is shown in Figure B-1. The ordinate (P_{cyl}-P_a) and the projected degree scale were selected for convenience in computing the pressure drag coefficient. P_{cyl} is cylinder surface pressure and P_a is atmospheric static pressure outside the tunnel. All measured pressure distributions are qualitatively the same, except where slippage occurred and the plot is asymmetric. The slippage, as referred to in this report, was the difference in degree between the actual circumferential location of the pressure tap and the location indicated by the compass pointer (Fig H-12). Cause of slippage is discussed under Pressure Drag Coefficient.

Comparison of Figure B-1 with Figure 6-24 in (Ref 8: 161) shows that the flow, Reynold's number and pressure distribution are subcritical. This indicates that the boundary layer is laminar, and that laminar separation occurs at approximately 82 degrees from the stagnation point. Examination of the 70-degree point on both figures shows that they coincide closely. The remainder of the curves are qualitatively the same. Comparison of Figure B-1 with other references shows good agreement (Ref 34: 1264;41:221). The basic difference between references is that (Ref 8:161) shows a discontinuity in the slope of the pressure curves at the 70-degree point, while the others

listed do not.

Pressure Drag Coefficient

The pressure drag coefficient C_{dp} is plotted versus the free stream Reynold's number in Figures B-2 and B-3. Appendix B illustrates the method which was used to calculate the pressure drag coefficient. The results are shown to be in close agreement with the total drag coefficient (Ref 32:16), if the skin friction drag is assumed small. Geidt states that form (pressure) drag constitutes in general 98 percent or more of the total drag, for a Reynold's number of 70, 800 to 219,000 (Ref 12:725,726). The Reynold's number for the tests in this report ranged from 9,870 to 84,200.

The drag coefficients for cylinder C (at $Re > 6x10^4$, $I \approx 4.1a.$) are high because the mica cylinder slipped in its Teflon bushing while being rotated. This slippage occured after approximately 25 hours of testing above 500°F. The cause of the slippage was enlarging of the slot in the mica cylinder by the wedge, which was inserted in the mica cylinder so that it would rotate with the degree pointer. The slot enlarged because the mica could not resist the pressures of the wedge after prolonged heating. This prolonged heating forced the shellac, which binds the sheets of mica together, to the surface of the cylinder. The shellac was then swept away by the airstream. Because of this, the mica cylinder had little resistance to a force in a direction tangent to the circumference of the cylinder,

and so the wedge crushed it. The error in reading the degree of rotation was as high as 25 degrees between actual circumferential location of the pressure tap and the location indicated by the compass pointer. Although the error was checked and compensated for before each rotation, the error did not remain constant during a 360-degree rotation. This was serious in the two cases mentioned and resulted in a noticeable error when pressure distributions and pressure drag coefficient were computed.

Dynamic and Total Pressure Distributions

Dynamic and total pressure distributions across the tunnel were drawn for each traverse made with cylinders A and C (Figures 2 through 49). Total pressure curves were drawn because they were the most accurate pressure measurements taken. Dynamic pressure curves, rather than velocity curves, were drawn to avoid the error introduced in computing density. The flow field in the wake of the cylinder had a continuously varying pressure and, when heated, a continuously varying temperature. The thermocouple in the three hole probe indicated its maximum temperatures in the wake. For cylinder A, the maximum was 95°F; for cylinder C, the maximum was 108°F. However, there may be considerable conduction and radiation errors, and the true temperature may be considerably higher. Because the primary interest of this study was drag rather than velocity profiles, only dynamic pressure curves were drawn. Velocity, V, can be estimated from the equation:

$$V = (2q/\rho)^{\frac{1}{2}}$$

where q is dynamic pressure and is obtained from Figures 2 through 49. The density, ρ, can be estimated from the perfect gas law, using a temperature equal to T_a and a pressure equal to the total pressure minus dynamic pressure.

In the following discussion dynamic, q, and total pressure, $(P_t - P_a)$, curves will be compared at each test velocity for I = 0 amperes, $I \approx 4.1$ amperes; and $I \approx 6.15$ amperes (Figs 2 through 49).

Test velocities will be nominally referred to as 40, 80, 120, and 160 fps, but the computed tunnel velocities differed slightly from the nominal velocities.

Cylinder A. At 40 fps an increase or decrease in the width of the wake of the q curve could not be determined. Comparison of the q curves for different heating rates showed a decrease in q throughout the wake for a increase in cylinder heating. When the q curves are compared with the total pressure curves, a depression in static pressure is evident in the wake. An increase in thermocouple temperature in the wake was also measured. The decrease in pressure and the increase in temperature in the wake results in a decrease in density. Since $V = (2q/\rho)^{\frac{1}{2}}$, the velocity at a fixed point in the wake tends to decrease less with a decrease in both q and ρ than with a decrease in q alone.

The $(P_t - P_a)$ curves at 40 fps have the same depression

tendency, but not as pronounced. The (P_t-P_a) curves for I = 0 amps indicate a lower value than the (P_t-P_a) curves for I 4.1 amps and I 6.15 amps. This lower total pressure is attributed to a dust collecting on the parachute cloth inlet. The dust deposits act to clog the inlet and produce a total pressure loss. The 40 fps test for I = 0 amps was the last of the four velocities tested at I = 0 amps and, therefore, the cloth had the greatest buildup of dust. At the other two heating rates, the 40 fps tests were run first to hasten stabilization of the cylinder temperature and little buildup of dust on the inlet occurred. The difference in total pressures at the upstream centerline amounted to 0.136 inches H_2O. The dynamic pressure curves were not noticeably affected. The conclusion is that dust on the cloth inlet causes a decrease in static pressure with reference to a recently vacuumed inlet. To correct for this the cloth inlet was vacuumed daily.

At 80 fps the q curves behaved similar to those in the 40 fps test, i.e., decreased q in the wake with increased heating. The total pressure curves showed the same effect of dust collection as for the 40 fps tests. The difference in total pressures measured at upstream centerlines was 0.306 inches H_2O. In addition there was a slight variation between the q curves of the two higher heating rates. Since these last two tests were performed on different days, variation was attributed to changes in atmospheric pressure and temperature.

At 120 fps the q curves showed the same characteristics as the 40 and 80 fps curves, except that the decrease of q in the wake was somewhat erratic. Upon reexamination of both the 80 and 120 fps q curves, it was discovered that the q curve at the first downstream station decreases very little with the increase from I = 0 amps to $I \approx 4.1$ amps. However, at $I \approx 6.15$ amps a significant decrease was noticed. At the other downstream station the q curve decreased significantly at $I \approx 4.1$ amps and remained almost identical at $I \approx 6.15$ amps. The total pressure curves at 120 fps were similar to the total pressure curves at 80 fps. Again, dust collection on the inlet caused a 0.4 inches H_2O difference in total pressures at upstream centerlines.

At 160 fps there were varying differences between the entire set of upstream and downstream total pressure and dynamic pressure curves. The upstream centerline velocities computed were 158.1, 159.2, and 161 fps. If these differences are combined with the variances in atmospheric pressure and temperature, an exact correlation of these total pressure curves is impossible. Since dynamic pressure varies as the square of velocity, an exact comparison of the dynamic pressure was also impossible.

For all dynamic and total pressure curves of cylinder A, there was no definite change in the width of the wake at the same probe station and velocity, when the heating rate was increased.

Cylinder C. As for cylinder A, dynamic and total pressure curves were examined for each velocity at I = 0 amps, $I \approx 4.1$ amps, and $I \approx 6.15$ amps.

At 40 fps only slight differences in total and dynamic pressure curves for all heating rates were discernible. This was observed upon separate examination of each probe station for all 3 heating rates.

At 80 fps an exact correlation of the q curves is impossible, because the upstream centerline velocity at the two higher heating rates was 82.6 fps compared to 79.1 at the lowest or zero heating rate. Examination showed that the total pressure curves for all three heating rates were almost the same, and that those for the two highest heating rates were almost identical.

At 120 fps, the q curves for cylinder C show the same tendency as the q curves for cylinder A, i.e., a decrease in q in the wake with a increase in the heating rate. Total pressure curves also followed this pattern, but in a different manner. The total pressure curves indicated a greater decrease in the wake when the heating was increased from $I \approx 4.1$ amps to $I \approx 6.15$ amps, than when heating was increased from I = 0 amps to $I \approx 4.1$ amps.

At 160 fps no correlation in the q curves or $(P_t - P_a)$ curves was possible because velocity varied from 159.5 to 165.5 fps and atmospheric conditions had changed significantly.

As for cylinder A, there was no definite change in

the width of the wake at the same probe station and velocity, when the heating rate was increased. It is possible in this investigation that the wall may not permit a noticeable widening of the wake unless the test conditions (V, P_a, T_a) could be closely duplicated and the tests were specifically directed at measuring the width of the wake.

V. Conclusions

The following conclusions are summarized from the discussion of results:

1) Drag of a cylinder cannot be measured by the momentum method, except possibly at large distances downstream.
2) Cylinder pressure distribution shows that the flow is subcritical and separation is laminar.
3) Pressure drag coefficients show close agreement with Schlichting's total drag coefficient curve (Ref 32:16), provided that slippage is considered.
4) When a cylinder is heated, the value of the dynamic and total pressures in the wake of the cylinder decreases as compared to a zero heating rate.
5) Use of a probe with small orifices and long time constant should be avoided, but the probe should have small overall size.

VI. Recommendations

Recommendations concerning the wind tunnel, cylinders, and probes are contained in this section.

Wind Tunnel

The wind tunnel should be calibrated to check flow conditions throughout. The calibration is considered complete when the velocity variation in the plane normal to the tunnel axis, the longitudinal static pressure variation, flow angularity, turbulence level, and fluctuations are known (Ref 28:11). Static ports for the tunnel wall should be made so any future pressure probe used may be checked.

The wind tunnel may be too small for cylinders as large as cylinders C. In this wind tunnel, cylinders with small diameters (cylinders A and B) should be used in preference to cylinder C.

The present test section is too short to attempt to measure drag by the momentum method. An additional section of rectangular duct should be inserted between the test section and the diffuser. A rake should also be procured, if measurement of drag by the momentum method is attempted again.

Some other means of measuring drag should be considered, i.e., strain gages, force balances, or other mechanical means. Strain gages would work well in a uniform temperature environment, but use near a heated cylinder may be impossible. Conventional use of wind tunnel force

balances using wires attached to the model may not be possible because of the small magnitude of the drag forces. For C_d = one, cylinder diameter = one inch, and velocity = 40 fps, the drag per inch length is 0.105 lbf per inch. This latter situation would also pose an end effect problem and the tare and interference of supports may be of the same magnitude as the drag itself.

Test Cylinders

If the same type of mica cylinder is used, several modifications are needed. The cylinder should be wound uniformly with the nichrome ribbon to as close to the wall supporting the cylinder as possible. This may necessitate use of a material other than Teflon for a bushing or use of a smaller bearing. Some separation and insulation between the nichrome and the thermocouple lead wires must be provided, especially in the case of a cylinder as small as cylinder A. Allowance must also be made to prevent heat buildup in the center of the cylinder and possible distortion of the cylinder. In lieu of the iron-constantan thermocouples, chromel-alumel thermocouples of sufficiently large diameter should be used to prevent breakage. Lead wire should be long enough to reach instrumentation without use of a terminal board or spot welding. Since the surface of the nichrome oxidizes and the mica becomes weaker with prolonged heating, test should be carefully planned for short run times and several cylinders should be available.

The use of another type of cylinder should be considered. A nichrome cylinder or the "Globar" made by the Carborundum Company are possibilities.

Three-Hole Probe

A probe with larger orifices and a shorter time constant needs to be used. A Prandtl-type probe of the same diameter as the three hole probe would have larger orifices and reduce the time constant considerably. One disadvantage is that the removable plates would have to be remachined to allow entrance of an L-shaped Prandtl probe and a removable bushing provided.

A method of timing the pressure changes should be used if the probe chosen has a long time constant. Professor H. C. Larsen, Head of the Department of Aeronautical Engineering, who was consulted near the completion of testing, has proposed a system using valves, a time delay switch, and a Polaroid camera to reduce pressure measurement time of probes with long time constants.

Bibliography

1. Comings, E. W., et al. "Air Turbulence and Transfer Processes - Flow Normal to Cylinders" Industrial and Engineering Chemistry. 40:1076-1082 (1948).

2. Dean, R. C., et al. Aerodynamic Measurements. Massachusetts Institute of Technology. Gas Turbine Laboratory, 1953.

3. Deaver, F. K., et al. "Heat Transfer from an Oscillating Horizontal Wire to Water." Journal of Heat Transfer, Trans. ASME, Series C, 84:251-256 (August 1962).

4. Delany, N. K. and N. E. Sorensen. Low-Speed Drag of Cylinders of Various Shapes. NACA Technical Note 3038. Washington: National Advisory Committee for Aeronautics, 1953.

5. Dommasch, D. O., et al. Airplane Aerodynamics (Third Edition). New York: Pitman Publishing Corporation, 1961.

6. Douglas, W. J. M. and S. W. Churchill. "Recorrelation of Data for Convective Heat Transfer between Gases and Single Cylinders with Large Temperature Differences." Chemical Engineering Progress Symposium Series, 52: 23-28 (1956).

7. Driver-Harris Co. Designing Nichrome V-Nichrome-Chromax Heating Elements. Technical Catalogue NCR-58. Harrison, New Jersey:1958.

8. Eckert, E. R. G., and R. M. Drake Jr. Heat Mass and Transfer (Second Edition). New York: McGraw-Hill Book Company, Inc., 1959.

9. Eckert, E. R. G., and E. Soehngen. "Distribution of Heat Transfer Coefficients Around Circular Cylinders in Crossflow at Reynolds Numbers From 20 to 500." Transactions of the American Society of Mechanical Engineers, 74:343-347 (April, 1952).

10. Fand, R. M. "Heat Transfer By Forced Convection From A Cylinder to Water in Crossflow." International Journal of Heat and Mass Transfer, 8:995-1010 (1965).

11. Fand, R. M., et al. "The Local Heat Transfer Coefficient Around a Heated Horizontal Cylinder in an Intense Sound Field." Journal of Heat Transfer, Trans.

ASME, Series C., 84:245-250 (August, 1962).

12. Giedt, W. H. "Effect of Turbulence Level of Incident Air Stream on Local Heat Transfer and Skin Friction on a Cylinder." Journal of the Aeronautical Sciences, 18:725-730+ (November, 1951).

13. -----. "Investigation of Variation of Point Unit Heat Transfer Coefficient Around a Cylinder Normal to an Air Stream." Transactions of the American Society of Mechanical Engineers, 71:375-381 (May, 1949).

14. Goldsmith, A., et al. Handbook of Thermophysical Properties of Solid Materials. Volume III: Ceramics. New York: Macmillan Co., 1961.

15. Hebert, P. E. Determination of the Average Heat Transfer Coefficient From A Cylinder in a Crossflow to a Hydrocarbon Polymer of High Viscosity. Thesis. Wright-Patterson AFB, Ohio: Air Force Institute of Technology, 1957.

16. Johnson, B. V., and J. R. Hartnett. "Heat Transfer From a Cylinder in Crossflow With Transpiration Cooling." Journal of Heat Transfer, Trans. ASME, Series C, 85:173-179 (May, 1963).

17. Keenan, J. H. and J. Kaye. Gas Tables. New York: John Wiley and Sons, Inc., 1954.

18. Kestin, J. and P. F. Maeder. "Influence of Turbulence on Transfer of Heat From Cylinders." NACA Technical Note No. 4018. Washington: National Advisory Committee for Aeronautics, October, 1957.

19. Kestin, J., et al. "The Influence of Turbulence on the Transfer of Heat to Cylinders near the Stagnation Point." Journal of Applied Mathematical Physics, 12:115-130 (1961).

20. Kreith, Frank. Principles of Heat Transfer (Second Edition). Scranton, Pennsylvania: International Textbook Company, 1966.

21. Maltby, R. L. Flow Visualization in Wind Tunnels Using Indicators. AGARDograph 70. Paris, France: North Atlantic Treaty Organization Advisory Group for Aeronautical Research and Development, April, 1962.

22. McAdams, William H. Heat Transmission (Third Edition). New York: McGraw-Hill Book Company, Inc., 1954.

23. Moffat, R. J. "Gas Temperature Measurement" in Temperature Its Measurement and Control in Science and Industry Volume 3 edited by Charles M. Herzfeld. New York Reinhold Publishing Corp., 1962, pp. 553-572.

24. Mullikin, H. F. "Gas Temperature Measurement and the High Velocity Thermocouple," in Temperature Its Measurement and Control in Science and Industry edited by American Institute of Physics. New York: Reinhold Publishing Corporation, 1941, pp. 775-804.

25. Pankhurst, R. C. and D. W. Holder. Wind Tunnel Techniques. London: Sir Isacc Pitman & Sons, Ltd., 1952.

26. Perkins, H. C. Jr., and G. Leppert, "Forced Convection Heat Transfer From a Uniformly Heated Cylinder." Journal of Heat Transfer, Trans. ASME, Series C, 84:257-263 (August, 1962).

27. -----. "Local Heat Transfer Coefficients on a Uniformly Heated Cylinder." International Journal Heat and Mass Transfer, 7:143-158 (1964).

28. Pope, Alan. Wind-Tunnel Calibration Techniques AGARDograph 54. Paris, France: North Atlantic Treaty Organization, Advisory Group for Aeronautical Research and Development, April 1961.

29. -----. Wind Tunnel Testing (Second Edition). New York: John Wiley and Sons, Inc., 1961.

30. Robinson, R. F. and D. H. Novak. Introduction to Wind Tunnel Testing (Second Edition). Lafayette, Indiana: Shaw's Letter Shop, 1952.

31. Roman, W. C. and T. W. Myers. Investigation of Electric Arc Interaction with Aerodynamic and Magnetic Fields. ARL 66-0191. Wright-Patterson Air Force Base, Ohio: Aerospace Research Laboratories, United States Air Force, September 1966.

32. Schlichting, Herman. Boundary Layer Theory (Fourth Edition). New York: McGraw-Hill Book Company, Inc., 1960.

33. Schmidt, E. and K. Wenner. Heat Transfer over the Circumference of a Heated Cylinder in Tranverse Flow. NACA Technical Memorandum 1050. Washington: National Advisory Committee for Aeronautics, 1943.

34. Schuh, H., and B. Persson. "Heat Transfer on Cylinders Exposed to Free-Jet Flow." International Journal of Heat and Mass Transfer, 7:1257-1271 (1964).

35. Seban, R. A. "The Influence of Free Stream Turbulence on the Local Heat Transfer From Cylinders." Journal of Heat Transfer, Trans. ASME, Series C, 82: 101-107 (May, 1960)

36. Silverstein, A. and S. Katzoff. "A Simplified Method for Determining Wing Profile Drag in Flight." Journal of the Aeronautical Sciences, 1:295-301 (1940).

37. Sogin, H. H. Heat Transfer From the Rear of Bluff Objects to a Low Speed Air Stream. ARL 62-361. Tulane University, New Orleans, Louisiana: Aeronautical Research Laboratories, Office of Aerospace Research, United States Air Force.

38. Sparrow, E. M. Radiation Heat Transfer. Belmont, California: Brooks Publishing Co., 1966.

39. Tewfik, O. E., et al. "Measurements of Heat Transfer from a Cylinder with Air Injection into a Turbulent Boundary Layer." 63-HT-45. Presented at American Society of Mechanical Engineering Heat Transfer Conference, Boston, Massachusetts, 1963.

40. United Sensor and Control Corporation. Bulletins T-1 and T-2. Watertown, Massachusetts: 1966.

41. Van Der Hegge Zijnen, B. G. "Heat Transfer From Horizontal Cylinders to a Turbulent Air Flow," Applied Scientific Research, Section A, 7:205-223. (1958).

42. -----. "Modified Correlation Formulae for the Heat Transfers By Natural and By Forced Convection From Horizontal Cylinders." Applied Scientific Research, Section A, 6:129-140 (1956).

43. Wilkes, G. B. Heat Insulation. New York: John Wiley and Sons, Inc., 1950.

Appendix A

Aspirated Probe

The aspirated probe is a thermocouple probe, through which the gas whose temperature is to be measured is caused to flow at a higher rate than free stream (Refs 23 and 24). Its primary use, is in situations where heat by radiation is an important factor, i.e., large differences between gas temperature and wall temperature, or a highly radiant heat source. The high temperature for which this probe was designed did not occur in this investigation. However, since future investigations may be made at higher temperatures than encountered here, the design is presented here (Figure A-1) along with a short explanation of its operation.

Aspirating or forcing the air to flow faster through the probe than it does in the free-stream, causes the convection heat transfer between the junction and the air to be increased. Whether the probe is heated or cooled by the outer environment (heated cylinders and walls), an increase in the rate of heat transfer by aspiration will cause the junction to read closer to the true gas temperature. For example, if the tubing, in which the probe is located, is heated above gas temperature, the tubing will in in turn radiate more heat to the thermocouple junction, causing the junction to indicate a temperature higher than gas temperature. Now if the flow rate past the thermo-

couple is increased, the gas will cool the junction causing the thermocouple to indicate a temperature closer to gas temperature.

The tubing was covered with Teflon tape to provide some insulation between the stainless steel tubing and the aluminum foil. The aluminum foil was used because it has a low emissivity, i.e., $\epsilon = 0.087$ (Ref 22:477).

The recommendation for use of the Teflon and the aluminum foil is that of Mr. Franz Huber of the Flight Dynamics Laboratory at Wright Field, Dayton, Ohio. The use of aluminum foil is also mentioned in (22:262).

A definite improvement on this design would be to increase the diameter of the tubing, so that more air may be forced past the thermocouple.

The most probable reason for the failure of the aspirating probe is that not enough air could be forced past the thermocouple. This indicates that an aspirated probe is more suitable to high pressure flows, so that the hot gas itself will provide the flow through the aspirating probe without a need for a vacuum pump.

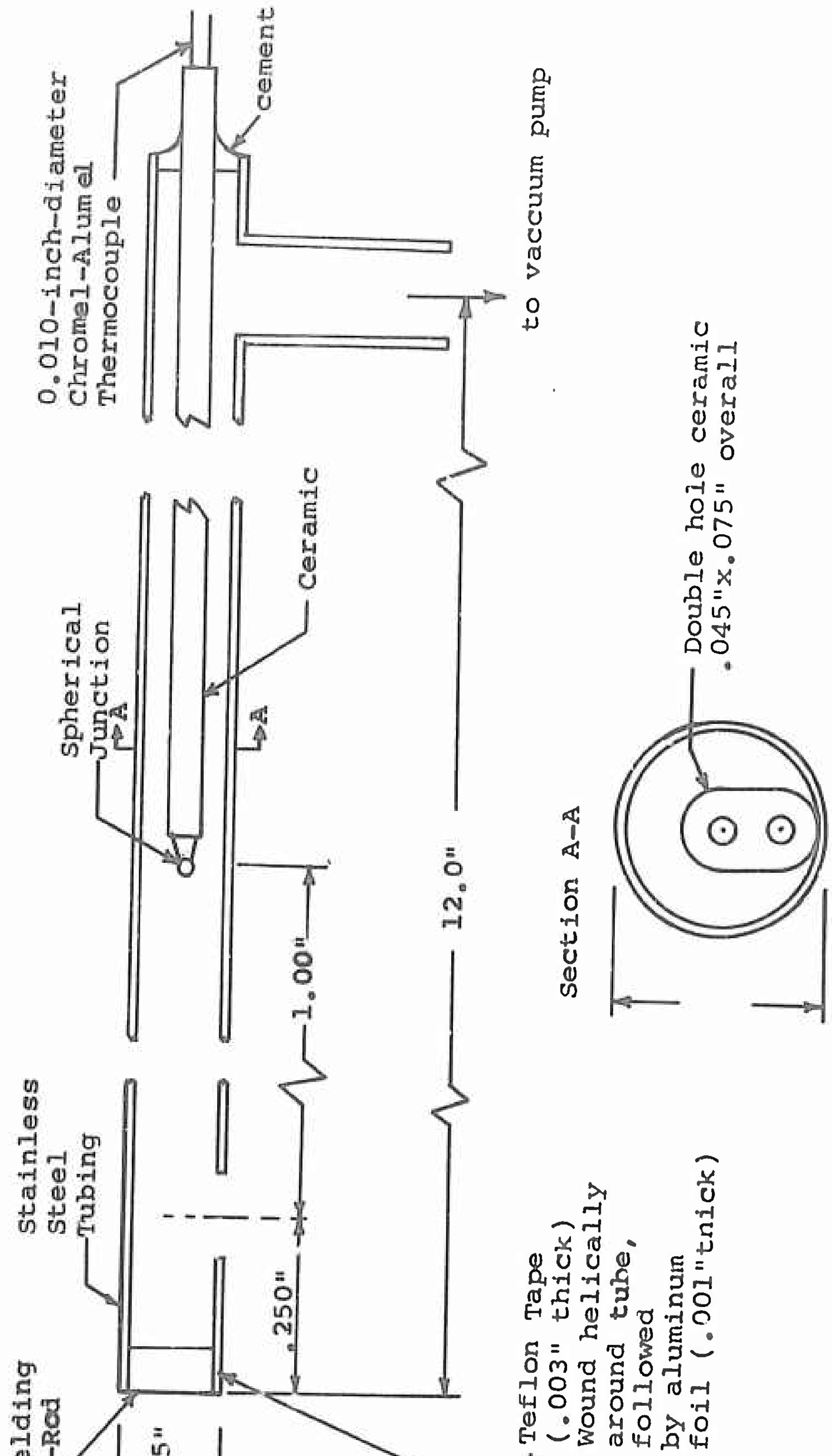

Figure A-1

Sketch of Aspirating Probe

Appendix B

Calculation of the Pressure Drag Coefficient

The pressure drag coefficient, C_{dp}, is calculated from the formula

$$C_{dp} = \frac{D_p/L}{q\ d}$$

where D_p/L is the pressure drag per unit length of cylinder, q is the upstream dynamic pressure at tunnel centerline, and d is the diameter of the cylinder.

The pressure drag, D_p, was computed by measuring the areas under the cylinder pressure distribution curve (such as Figure B-1) with a planimeter. Figure B-1 is a plot of the pressures measured by a tap on the cylinder surface versus the position of the tap as projected on a diameter normal to the free stream flow. In this manner each point represents a pressure force projected onto the diameter. The total pressure force on the front half of the cylinder is represented by the area between the ordinate axis and the curve labeled 270→360 and 0→90; the total pressure force on the rear half of the cylinder is represented by the area between the degree axis and the curve labeled 90→270. The pressure drag is the difference of these two quantities.

A corrected pressure drag coefficient, C_{dp_c} was computed from the formula

$$C_{dp_c} = \frac{D_p/L}{q_c \ d}$$

where $q_c = q\ (1+2\beta)$. The correction factor, β, can be found in Appendix I.

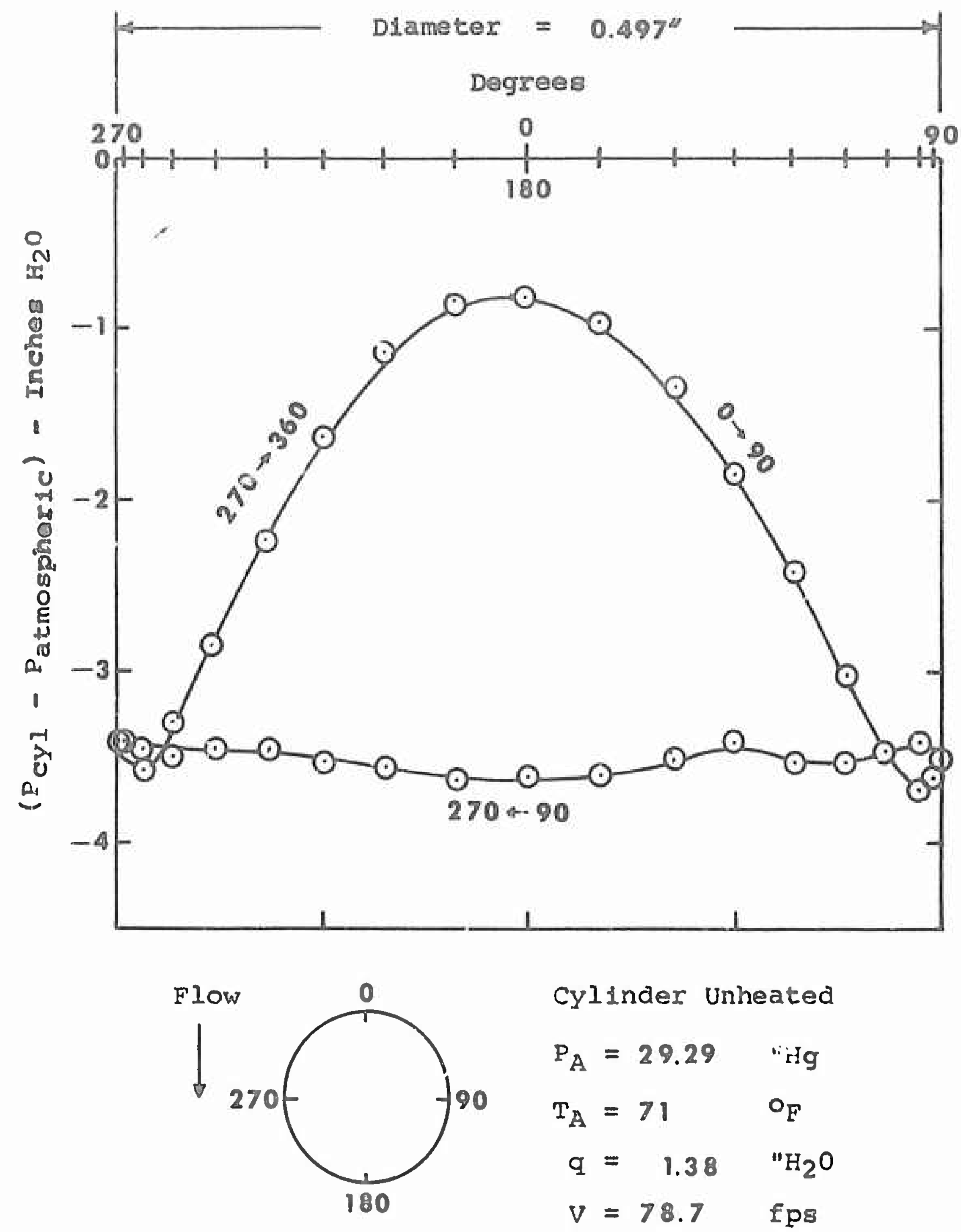

Figure B-1

Cylinder Wall Pressure

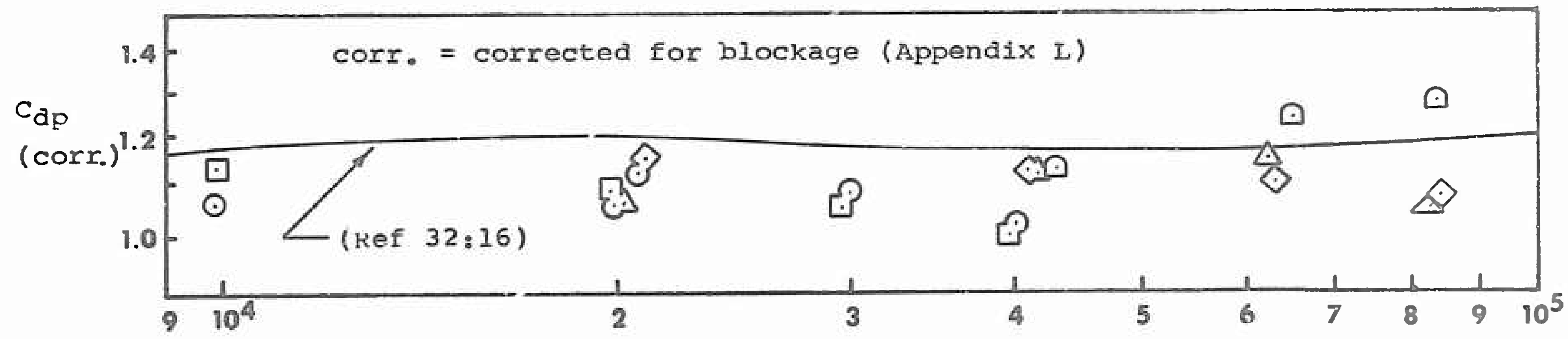

$Re_\infty = \rho_\infty V_\infty D/\mu_\infty$

Figure B-2

Pressure Drag Coefficient (corr.) vs. Reynold's Number

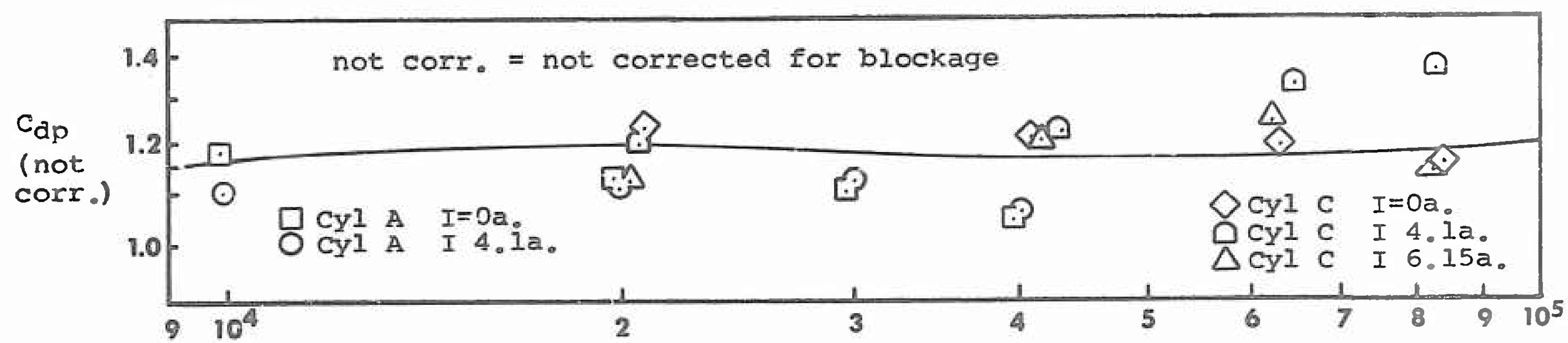

$Re_\infty = \rho_\infty V_\infty D/\mu_\infty$

Figure B-3

Pressure Drag Coefficient vs. Reynold's Number

Appendix C
Calibration Data for Three-Hole Probe

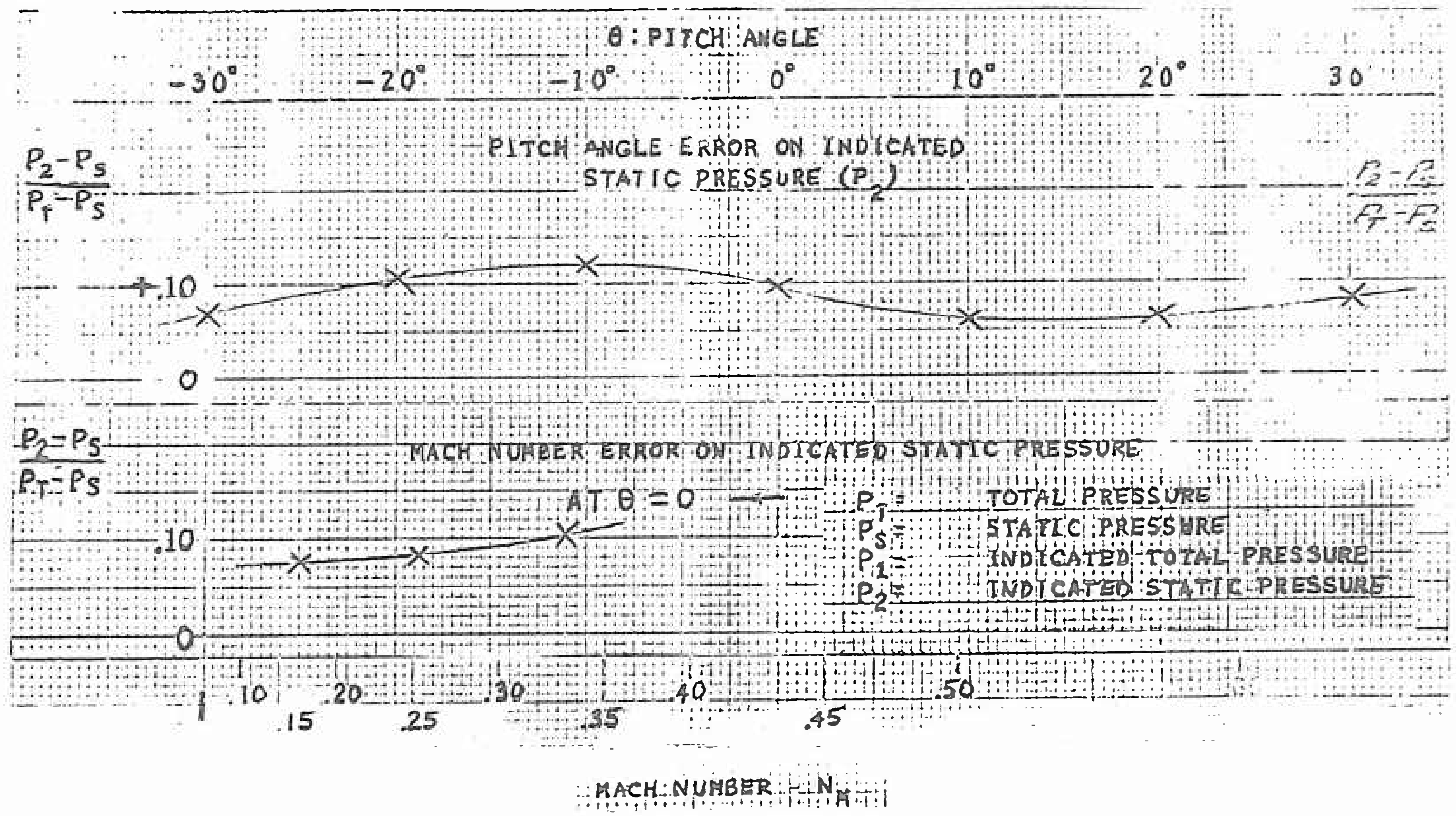

Figure C-1

Calibration Data for Three-Hole Probe with Thermocouple

(Probe Type YCT, Serial No. A-146, Diam. = 0.156 inches, Length = 12" inches, Chromel-Alumel Thermocouple, United Sensor and Control Corp.: Watertown, Mass.)

Appendix D

Design of the Octagonal Inlet

The following principles explain the design of the octagonal inlet as understood by the author. The front face and eight sides approximate a hemisphere (Fig D-1). If the air were entering the outer curved surface of a hemisphere, the air would travel the same distance to the center of the hemisphere. The air would be uniformly compressed together with no viscous shear, and, consequently, no vorticity. The cloth covering the front face and sides is of high porosity nylon parachute cloth, which has a loss of 0.5 inches H_2O when air passes through it at 150 cubic feet per minute per square foot of cloth.

The purpose of the cloth is to prevent any random vorticity (disturbances) in the air from initially entering the tunnel. The vanes (Figs D-2 and D-3) continue to prevent any vorticity from developing and direct the air into the centerline and parallel with the axis of the tunnel. The vanes do not extend all the way to the center of the back face because the dynamic pressure is increasing and the vanes may disturb the flow. A section is cut out of the large vanes so the vanes do not extend into this area, which is the entrance to the bellmouth. This cut-out section approximates a semi-circle, and its trailing edges are gently tapered to prevent separation and turbulence caused by a blunt edge. Since the vanes are cut out where the airspeed is still small, any blunt edge left on the

taper will have little effect. Once the air passes this point, no other devices (i.e., vanes) are used.

The contraction portion of the inlet, into which the air next passes, has also been modified. Originally this was the only part of the inlet, and it had a double contraction. Since the tunnel was not in operation when chosen for this study, the only reason the author could surmise for the double contraction was that it allowed insertion of honeycomb air straighteners. As the idea behind the new inlet is low turbulence, the honeycomb section, which may add turbulence, was removed. The double contraction was converted into a single smooth contraction by inserting a sheet metal plate, filling the surface discontinuities with an epoxy, and sanding until a smooth uninterrupted surface was obtained (Fig D-1).

The inlet is the design of Mr. Franz Huber, of the Flight Dynamics Laboratory at Wright Patterson AFB, Ohio, in cooperation with the author.

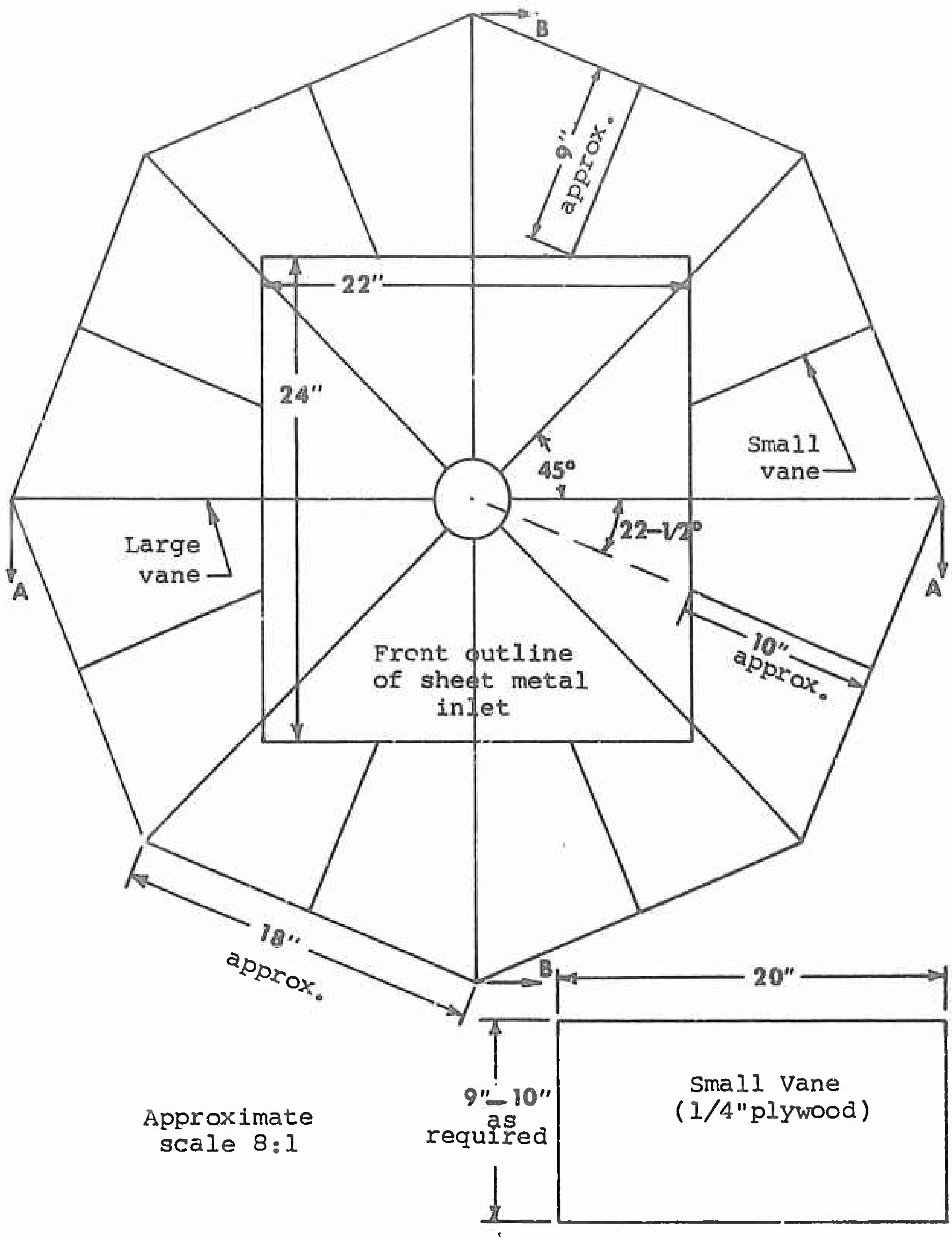

Figure D-1

Front View Sketch of Octagonal Inlet

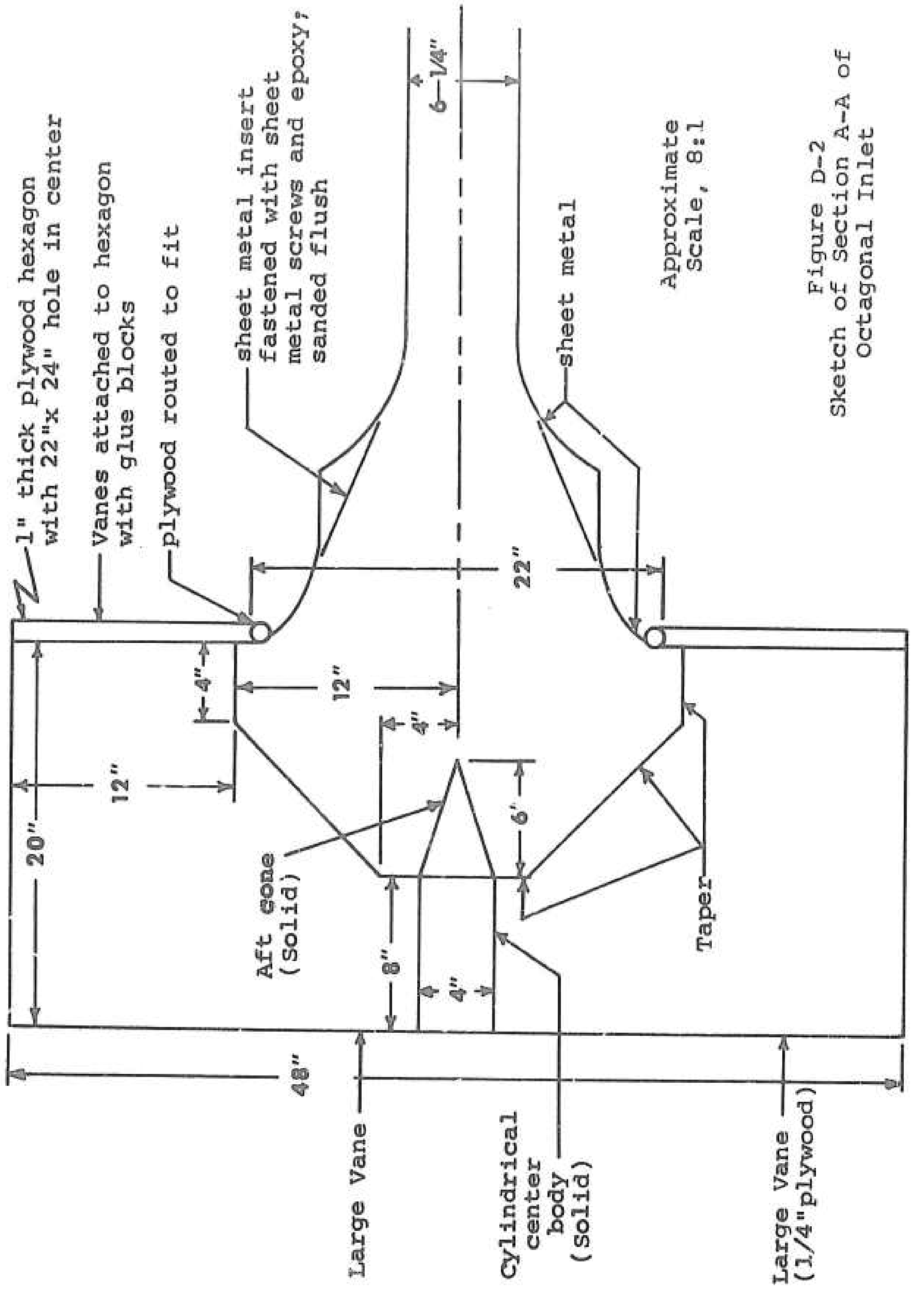

Figure D-2
Sketch of Section A-A of Octagonal Inlet

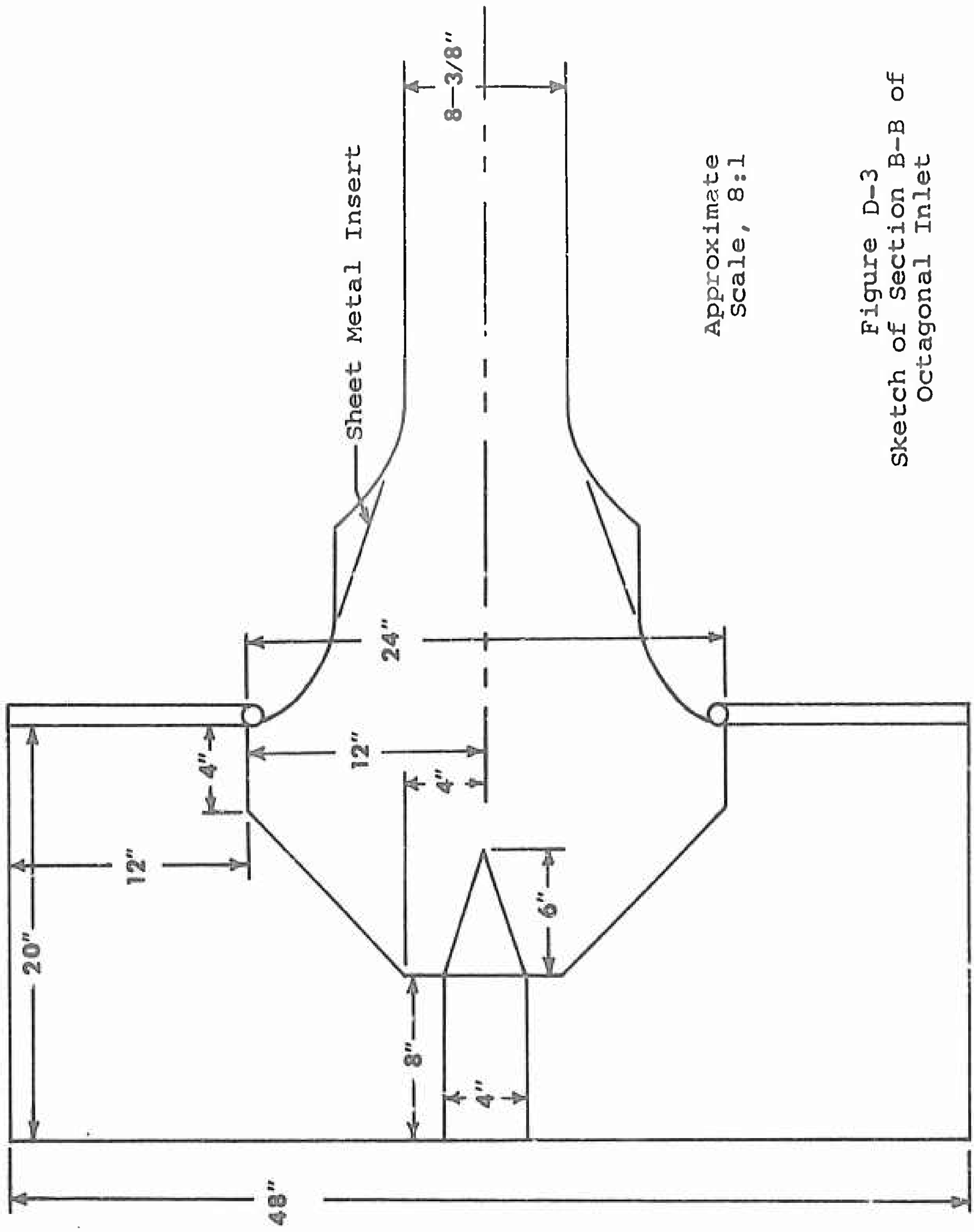

Approximate
Scale, 8:1

Figure D-3
Sketch of Section B-B of
Octagonal Inlet

Appendix E

Development of the Working Momentum Equation for Drag Calculations

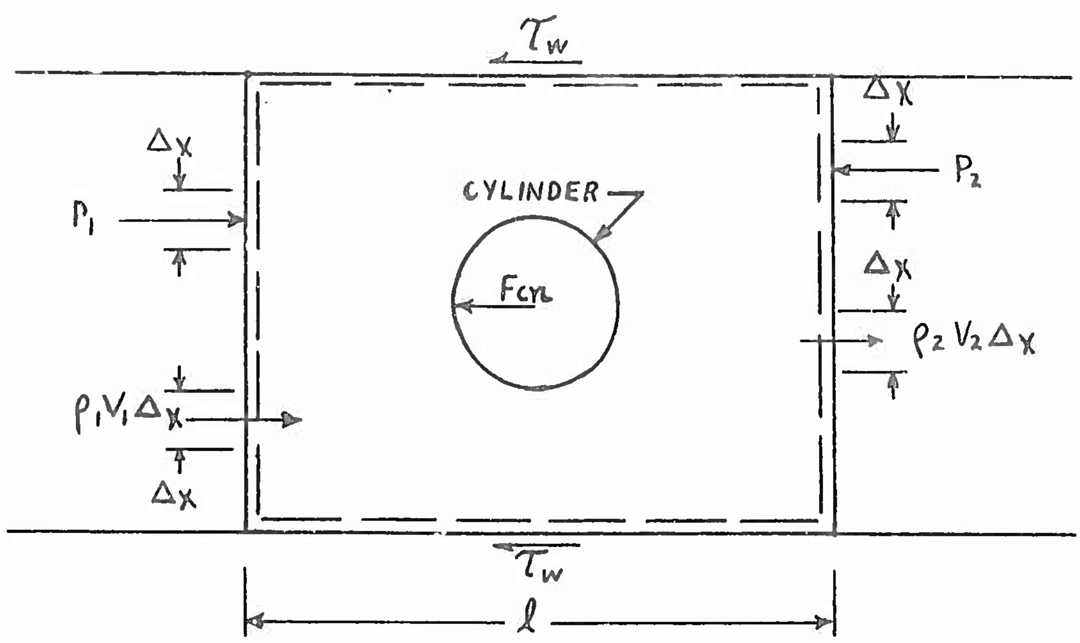

Figure E-1

Control Volume containing Cylinder

From Newton's law or impulse-mometum considerations: (Summation of forces in X direction) =

(Rate of change in momentum of the airflow)

or: $\Sigma F_y = \Delta M$. Considering the control volume (shown in a horizontal cross section in Figure E-1) per unit depth; this equation results in

$$\Sigma P_1 \Delta X - \Sigma P_2 \Delta X - \frac{F_{cyl}}{L} - 2 \tau_w l = \Sigma(\rho_2 V_2 \Delta X)V_2 - \Sigma(\rho_1 V_1 \Delta X)V_1$$

where p is static pressure, (F_{cyl}/L) is the force that the cylinder exerts on the airflow (and is numerically equal to the drag of the cylinder) per unit depth, τ_w is the wall

shear stress, ρ is density, and V is velocity. Assuming $-_{w}$ is small compared to other terms, one obtains, after regrouping,

$$\frac{F_{cyl}}{L} = \Sigma(P_1-P_2)\,\Delta X + \Sigma(\rho_1 V_1{}^2 - \rho_2 V_2{}^2)\,\Delta X.$$

Now, since the dynamic pressure, q, equals (1/2) V^2, or 2q equals V^2. Substituting yields

$$\frac{F_{cyl}}{L} = \Sigma(P_1-P_2)\,\Delta X + \Sigma(2q_1-2q_2)\,\Delta X.$$

Rewriting yields

$$\frac{F_{cyl}}{L} = \Sigma(P_1+q_1+q_1)\,\Delta X - \Sigma(P_2+q_2+q_2)\,\Delta X.$$

Introducing

$$P_t = P + 1/2\,\rho V^2 = P + q$$

where P_t is total pressure, into the last momentum equation yields

$$\frac{F_{cyl}}{L} = \Sigma(P_{t1}+q_1)\,\Delta X - \Sigma(P_{t2}+q_2)\,\Delta X.$$

Since P_t-P_a is measured directly (P_a is atmospheric pressure outside the tunnel), adding and substracting P_a gives the final useful result:

$$\frac{F_{cyl}}{L} = \Sigma\left[(P_{t1}-P_a) + q_1\right]\Delta X - \Sigma\left[(P_{t2}-P_a) + q_2\right]\Delta X$$

Appendix F

Graphical Presentation of Dynamic and Total Pressure Distributions

Figures 2 through 49 depict dynamic pressure, q, and total pressure minus atmospheric pressure, $P_t - P_a$, versus the distance, x, from the tunnel wall. The location of $x = 0$ is shown in Figure 1. Figure 1 shows the location of the probe stations for cylinders A and C and the symbol by which they are designated on Figures 2 through 49. The velocity, V, listed on each figure is the velocity computed from pressure measurements at the centerline of the upstream probe station. The velocity, V, was computed by the equation

$$V = (2q/\rho)^{\frac{1}{2}}$$

where q is the dynamic pressure, and ρ is the density. The density is calculated from the perfect gas law with the temperature, T_a, specified on each figure, and the static pressure equal to the difference between total and dynamic pressures at the centerline. The heating rate per inch of cylinder length, I^2R/L, is also indicated, so the pressure profiles of different heating rates can be compared.

Atmospheric pressure, P_a, and ambient temperature, T_a, are listed. Note that free stream temperature, T_∞, is assumed equal to T_a, but free stream static pressure, P_∞, is not equal to P_a. Upstream P_∞ is equal to total pressure minus dynamic pressure measured at tunnel centerline. Downstream wall static pressure at any point can be esti-

mated by subtracting dynamic pressure from total pressure at a point near the wall where both curves are flatest.

Figures 2 through 49 are arranged with cylinder A comprising the first half and cylinder C comprising the second half. The curves are further arranged according to velocity, i.e. 40, 80, 120, and 160 fps respectively. For each velocity, the curves are arranged in order of ascending heating rates. Further, the total pressure curves immediately precede the dynamic pressure curves for that velocity and heating rate.

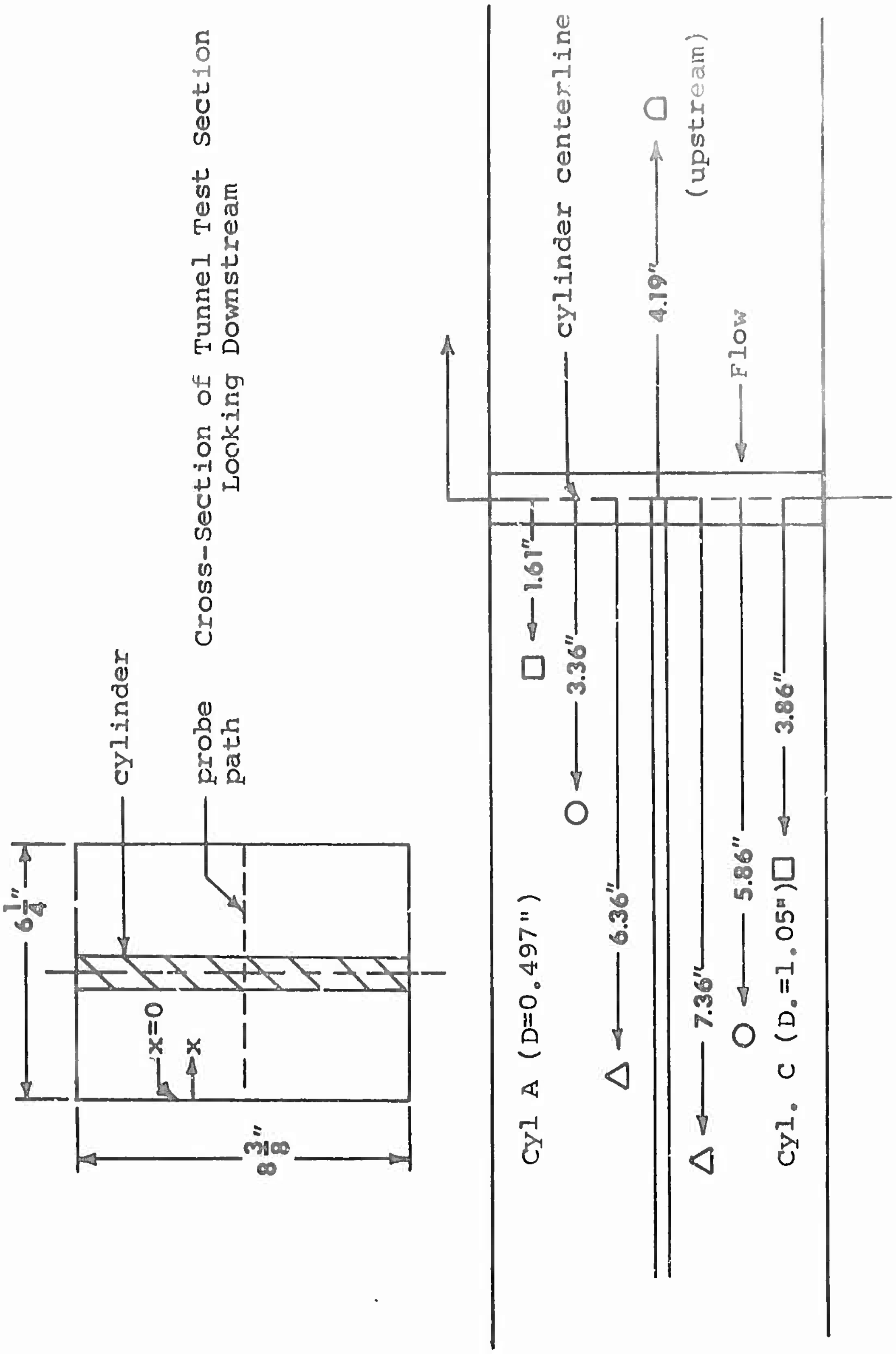

Figure 1
Location and Symbol Designation of Probe Stations

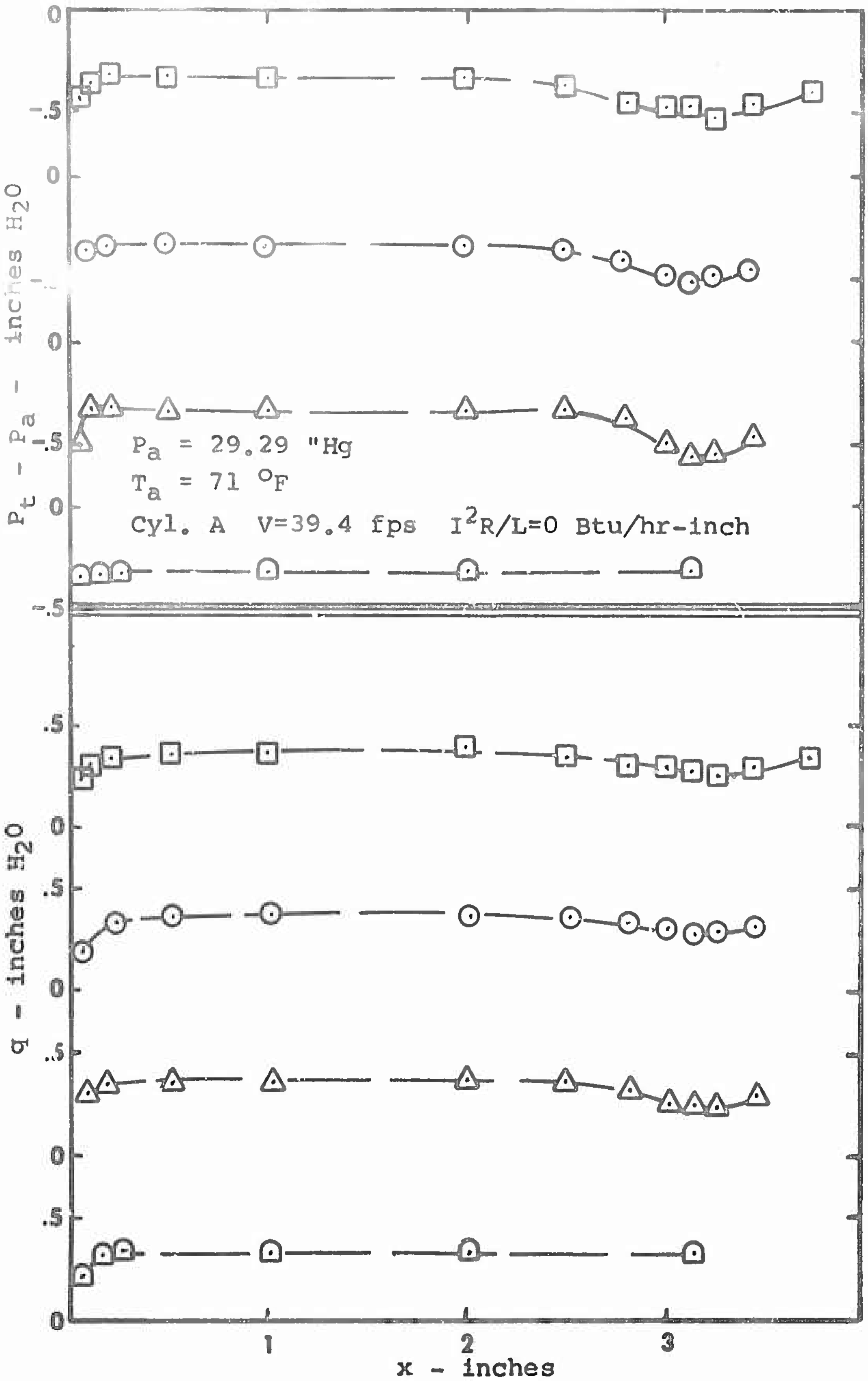

Figures 2 and3
Total Pressure minus Atmospheric Pressure
vs. Distance from Wall and
Dynamic Pressure vs. Distance from Wall

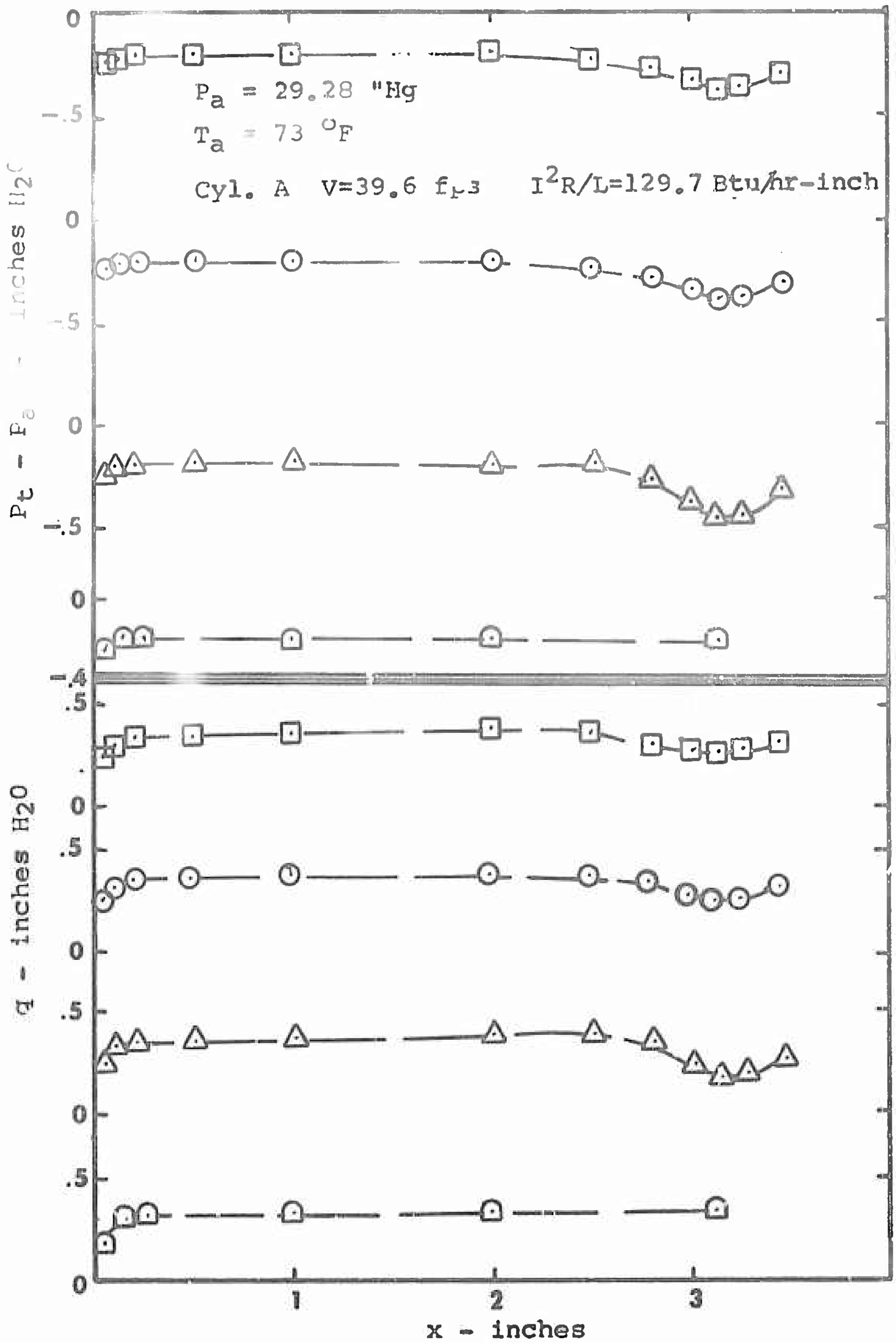

Figures 4 and 5

Total Pressure minus Atmospheric Pressure
vs. Distance from Wall and
Dynamic Pressure vs. Distance from Wall

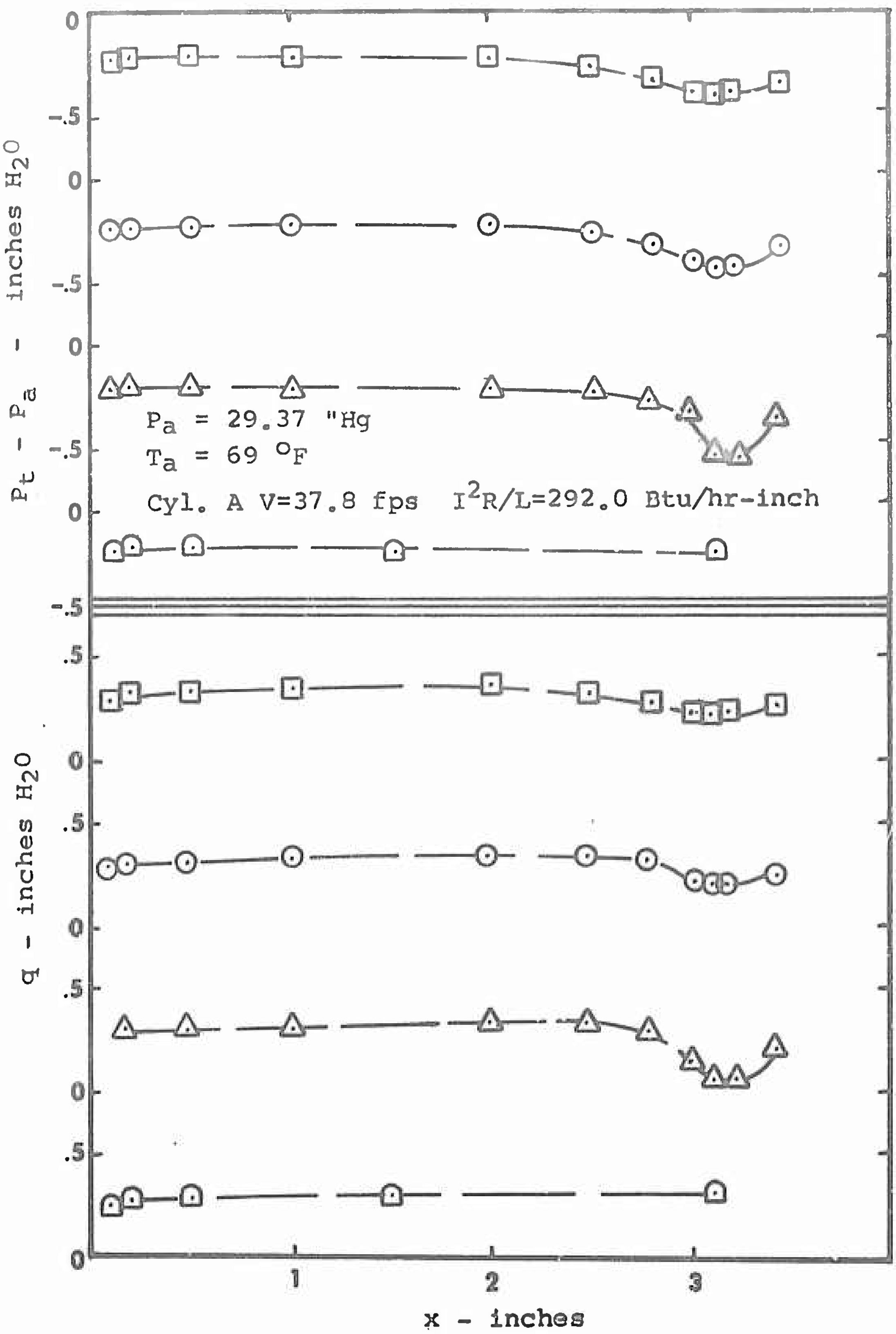

Figures 6 and 7
Total Pressure minus Atmospheric Pressure
vs. Distance from Wall and
Dynamic Pressure vs. Distance from Wall

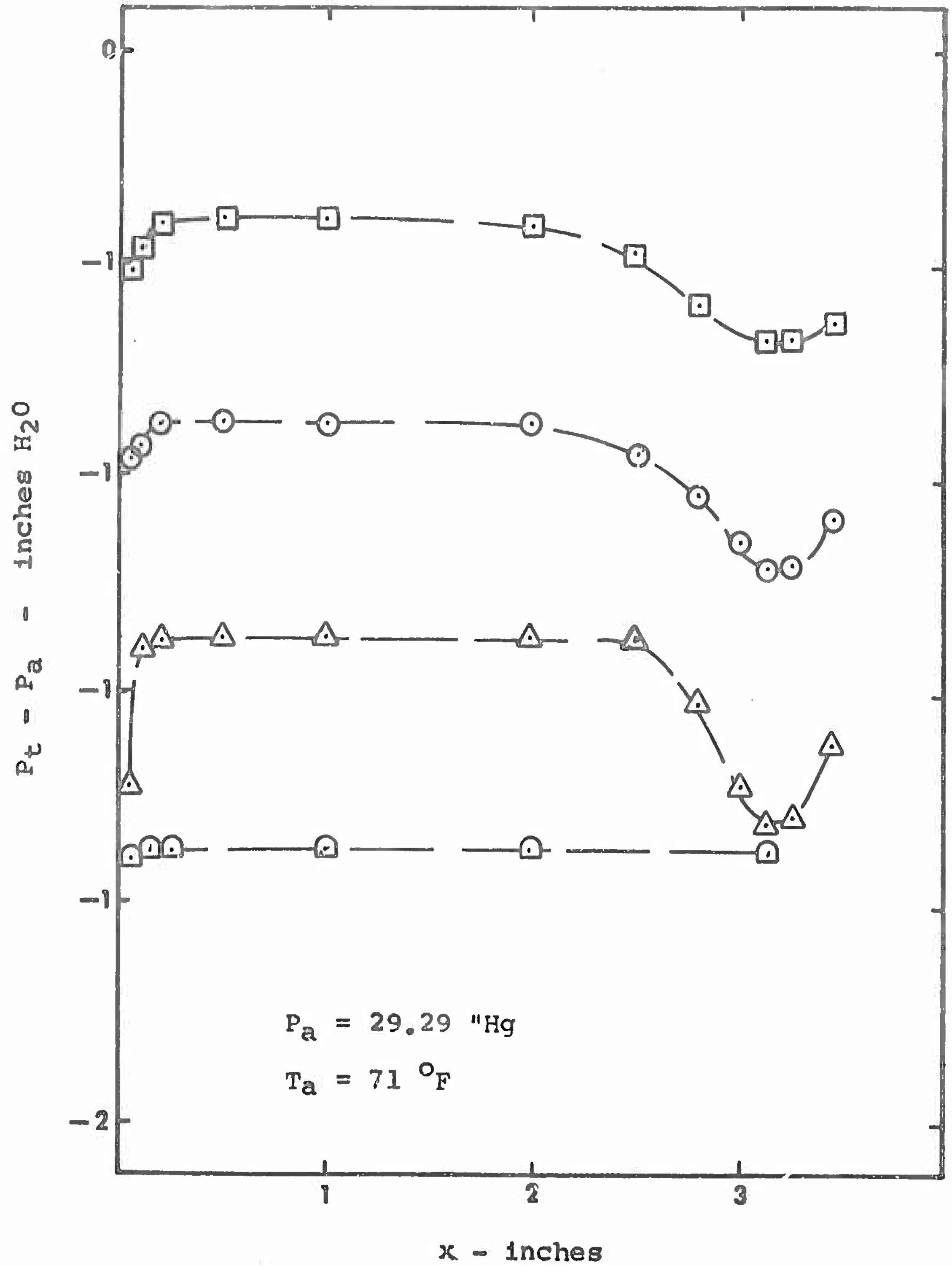

Figure 8

Total Pressure minus Atmospheric Pressure
vs. Distance from Wall

Cyl. A   V = 79 fps I^2R/L = 0 Btu/hr-inch

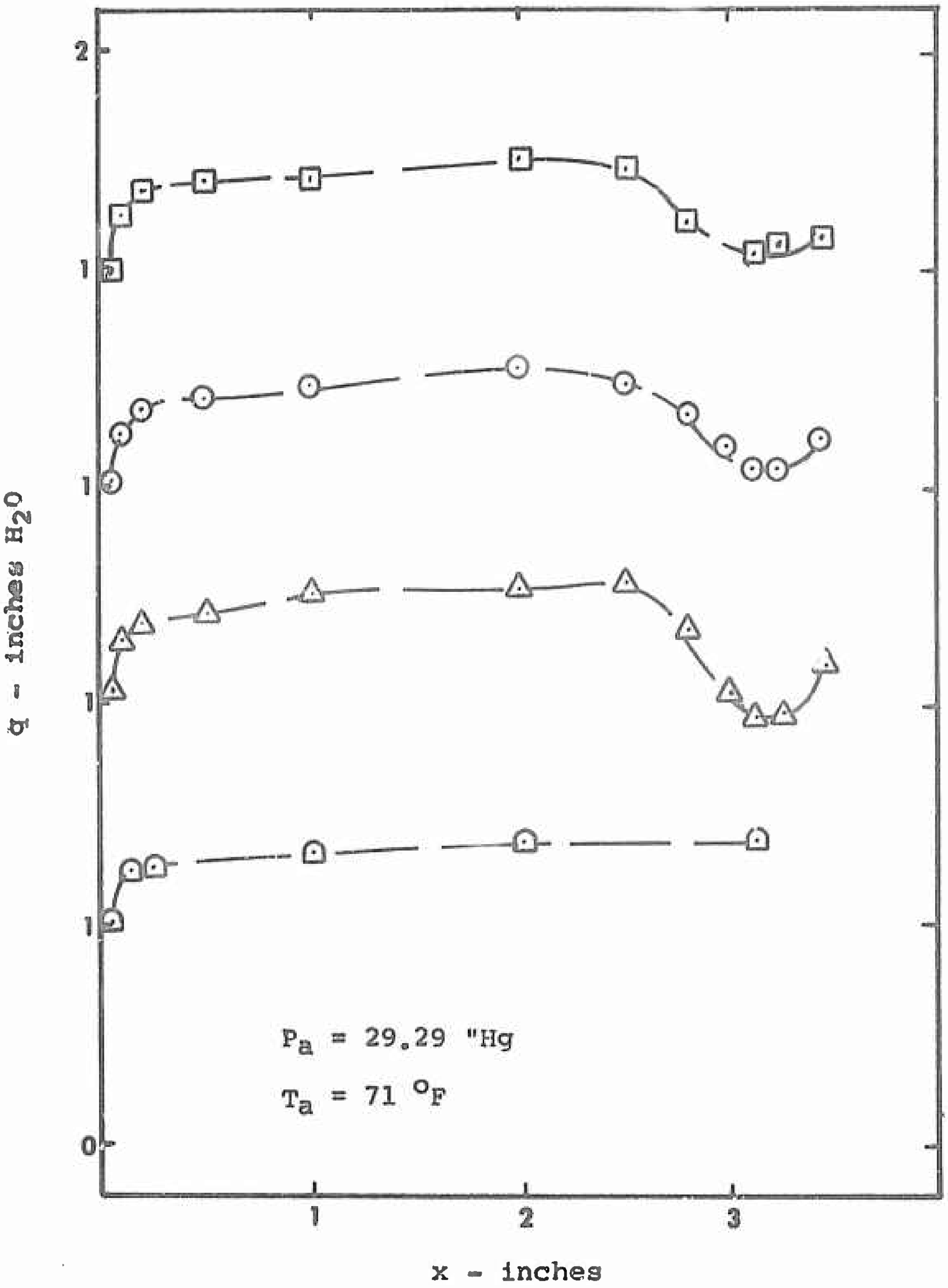

Figure 9

Dynamic Pressure vs. Distance from Wall

Cyl. A V = 79 fps I^2R/L = 0 Btu/hr-inch

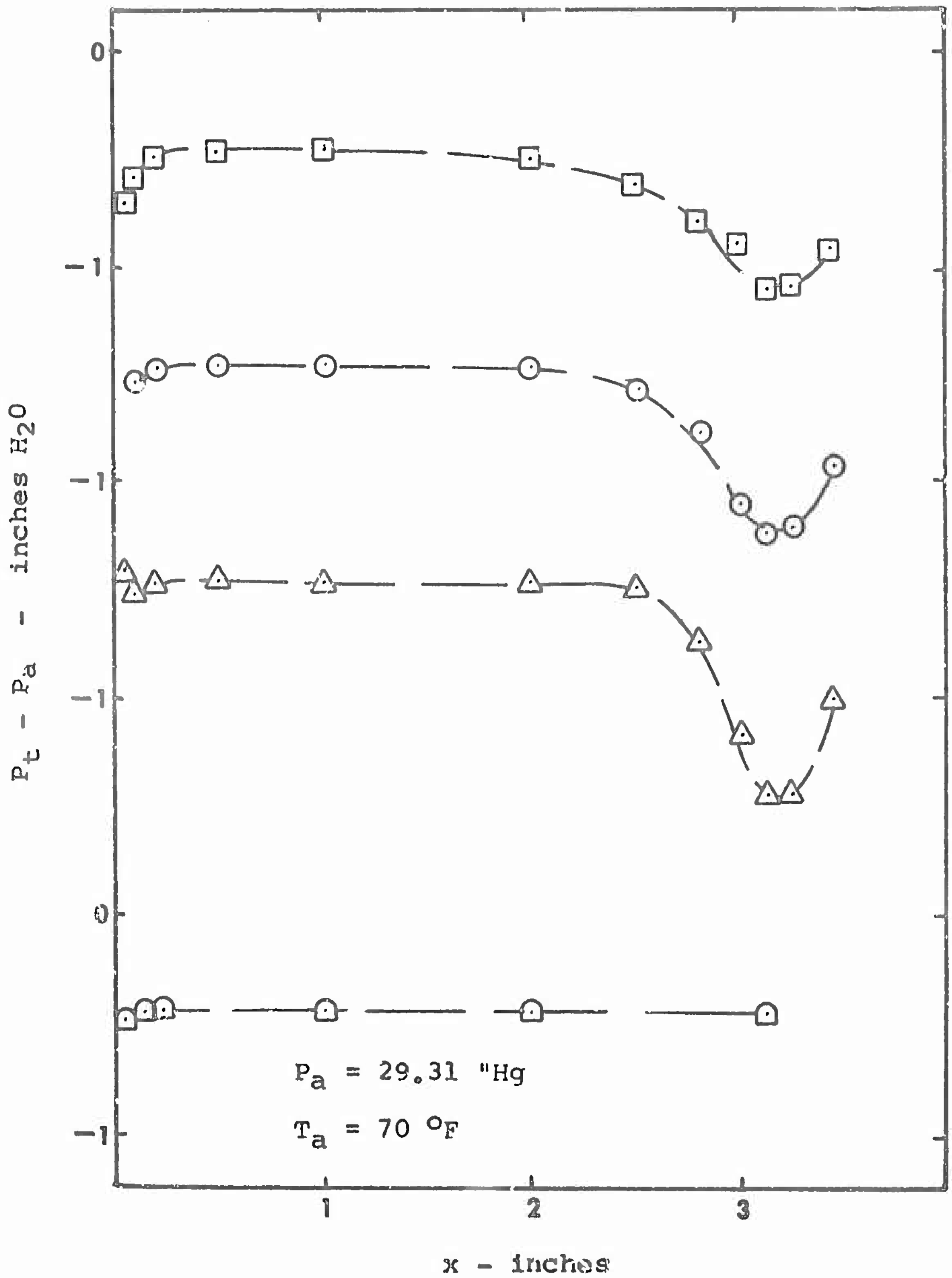

Figure 10

Total Pressure minus Atmospheric Pressure
vs. Distance from Wall

Cyl. A V = 79 fps I^2R/L = 128.2 Btu/hr-inch

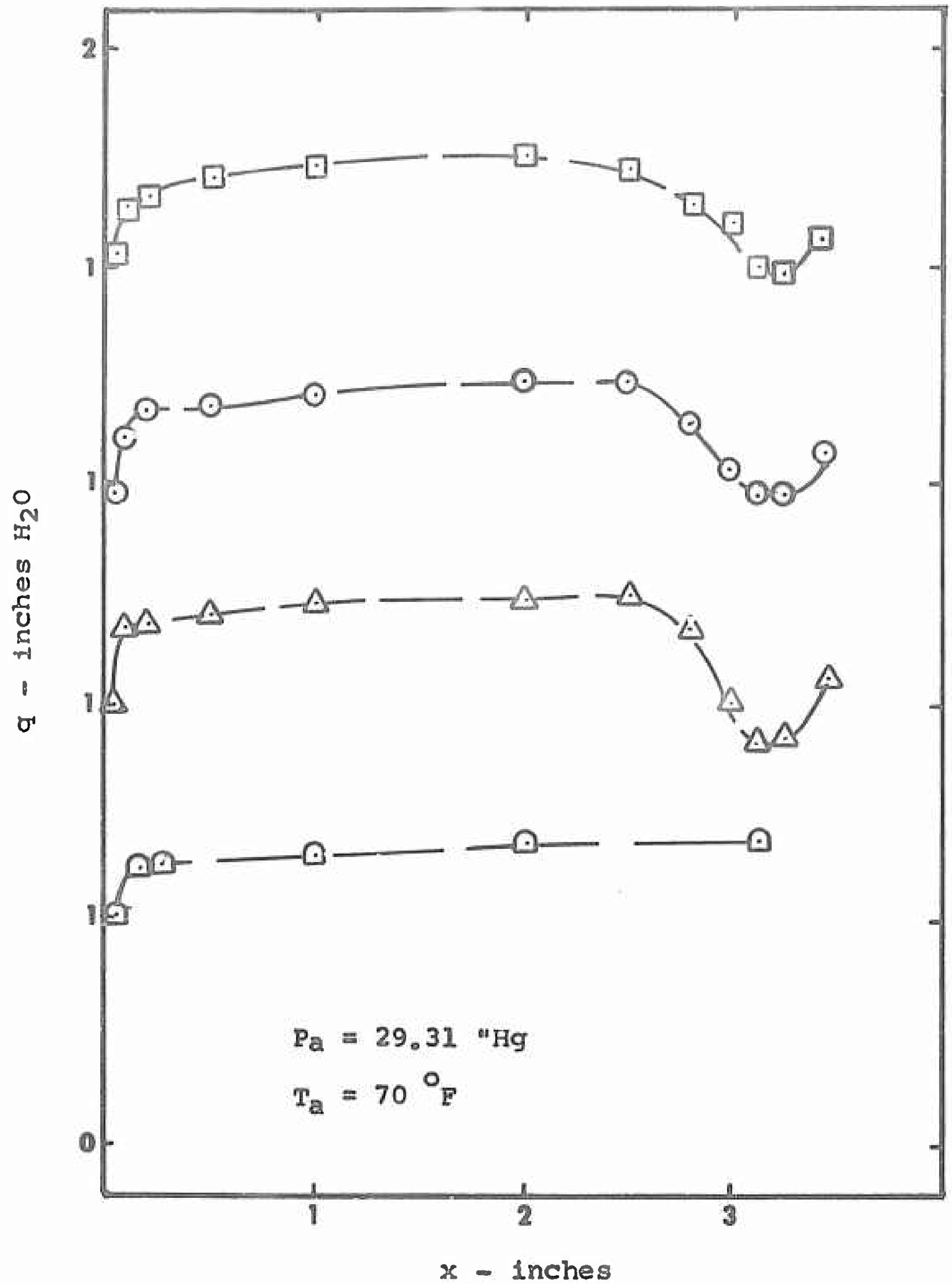

Figure 11

Dynamic Pressure vs. Distance from Wall

Cyl. A V = 79 fps I^2R/L = 128.2 Btu/hr-inch

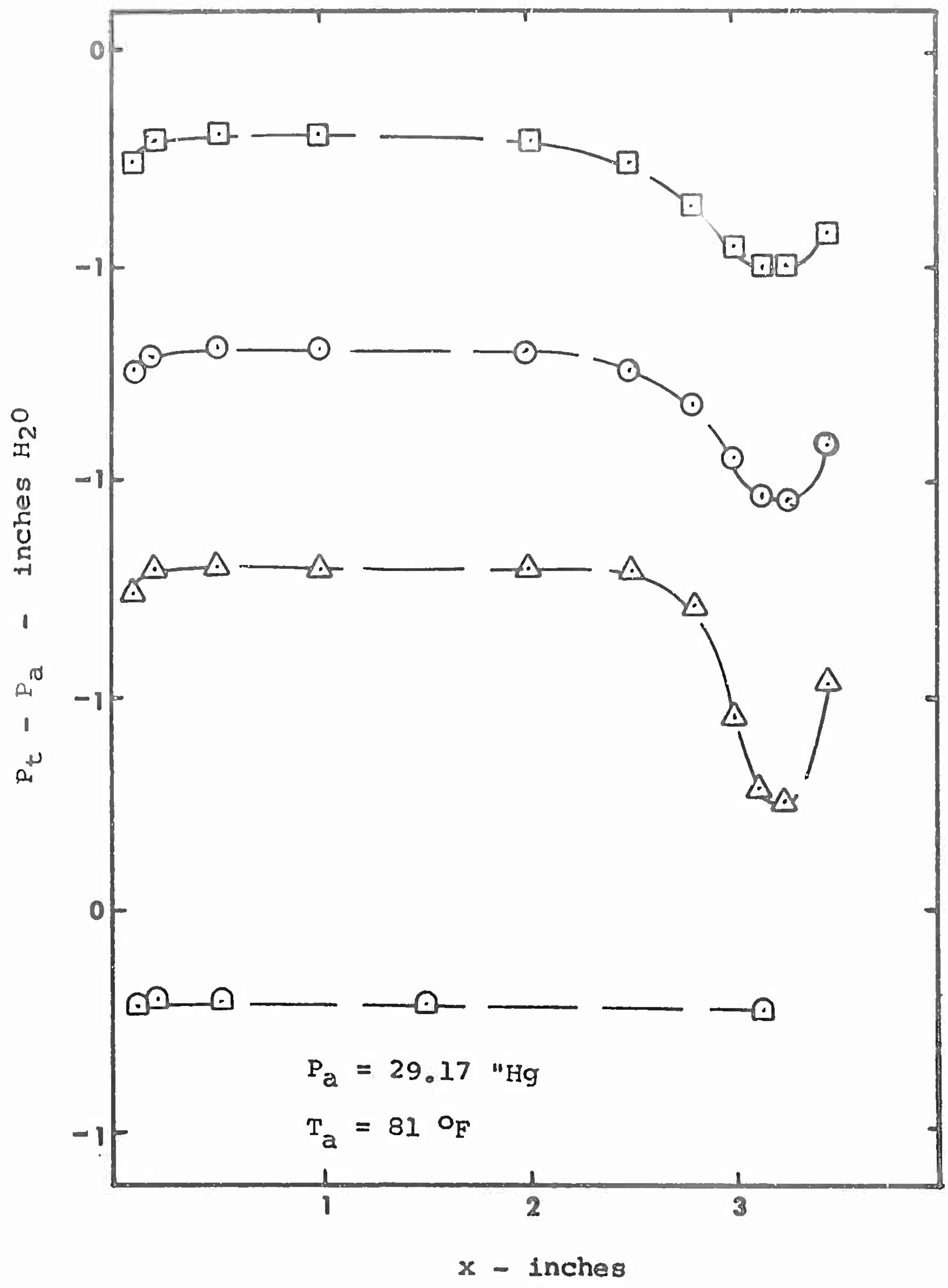

Figure 12

Total Pressure minus Atmospheric Pressure vs. Distance from Wall

Cyl. A V = 79.2 fps I^2R/L = 293.0 Btu/hr-inch

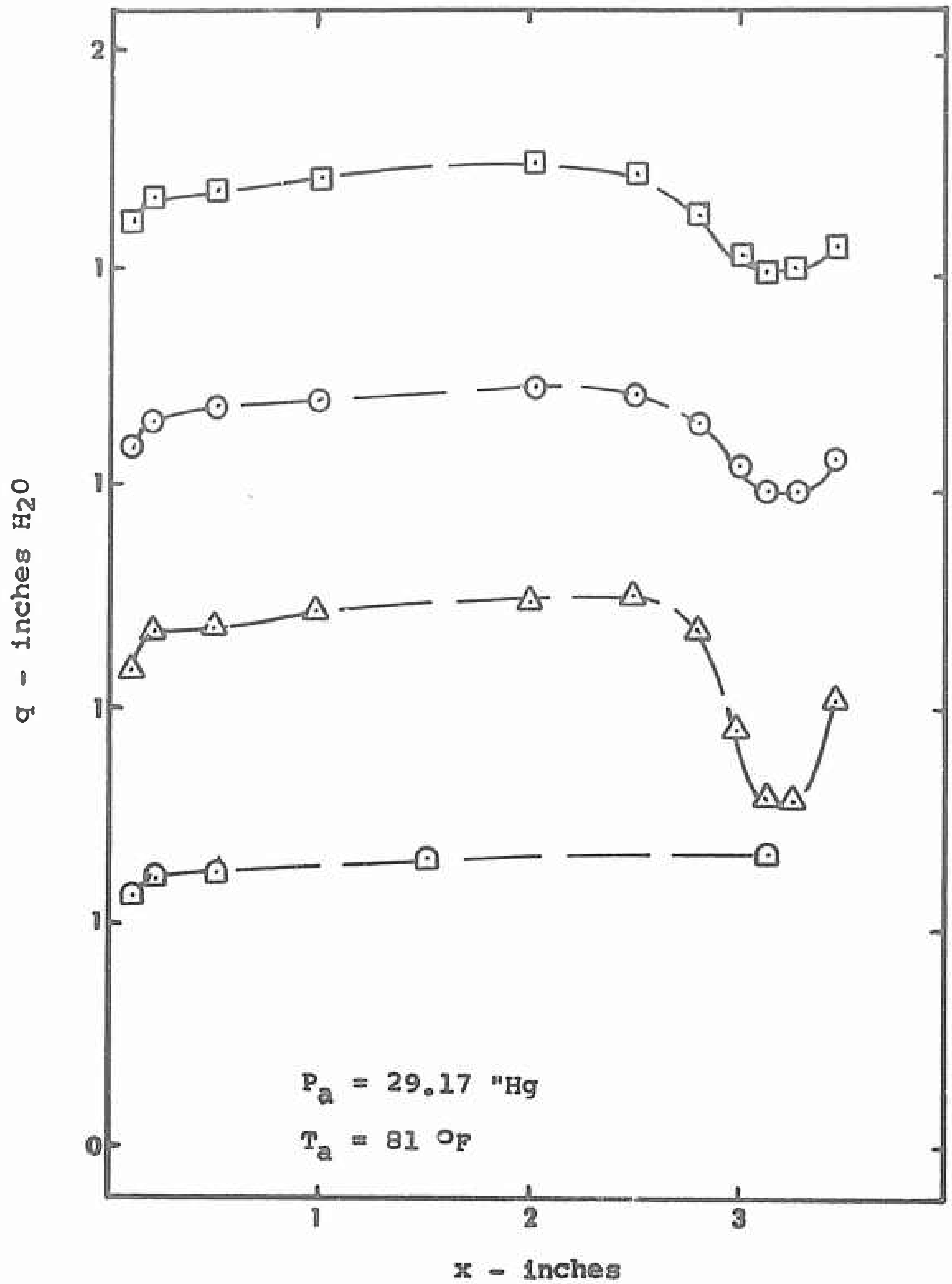

Figure 13

Dynamic Pressure vs. Distance from Wall

Cyl. A V = 79.2 fps I^2R/L = 293.0 Btu/hr-inch

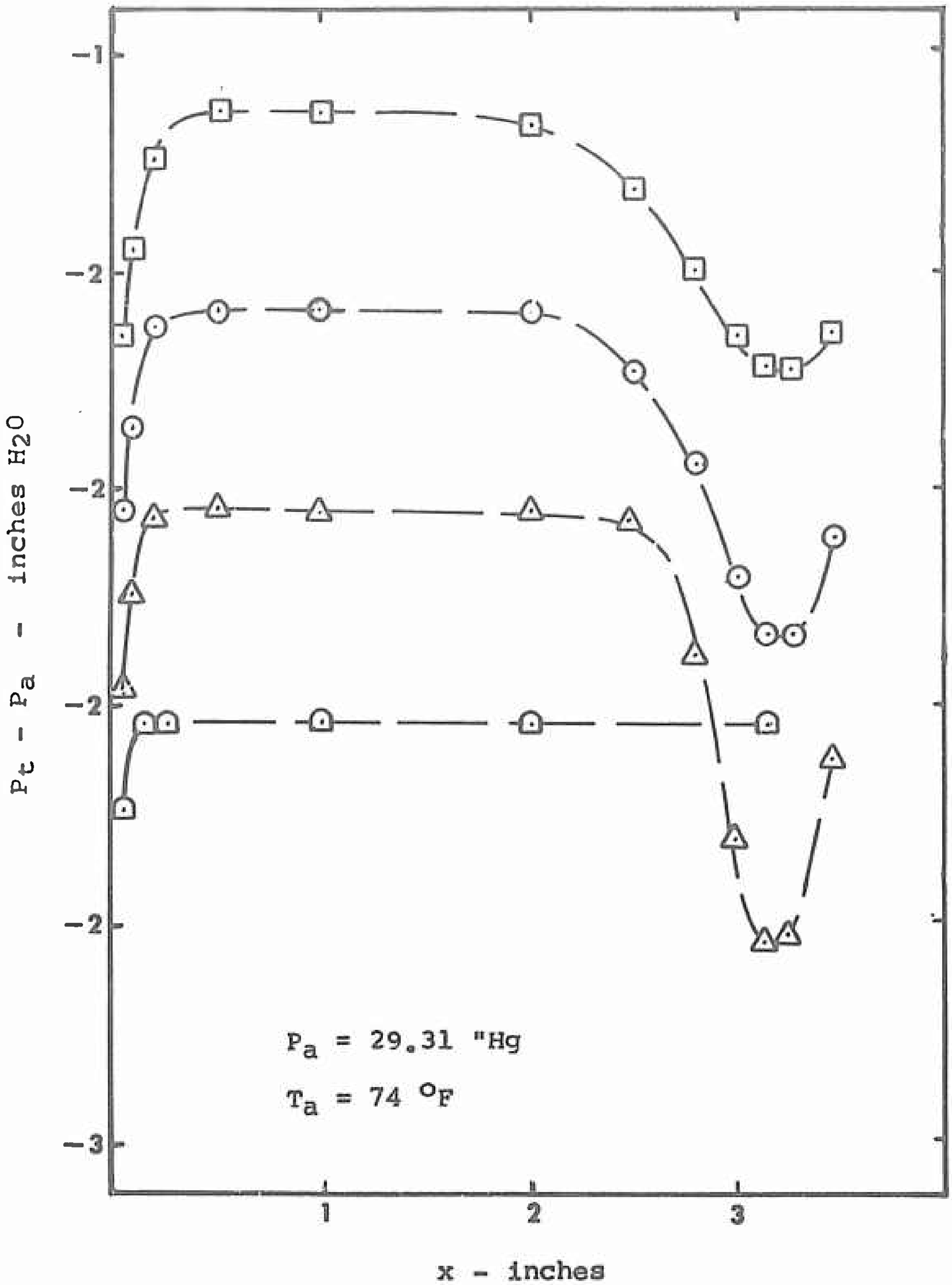

Figure 14

Total Pressure minus Atmospheric Pressure
vs. Distance from Wall

Cyl. A V = 119.6 fps I^2R/L = 0 Btu/hr-inch

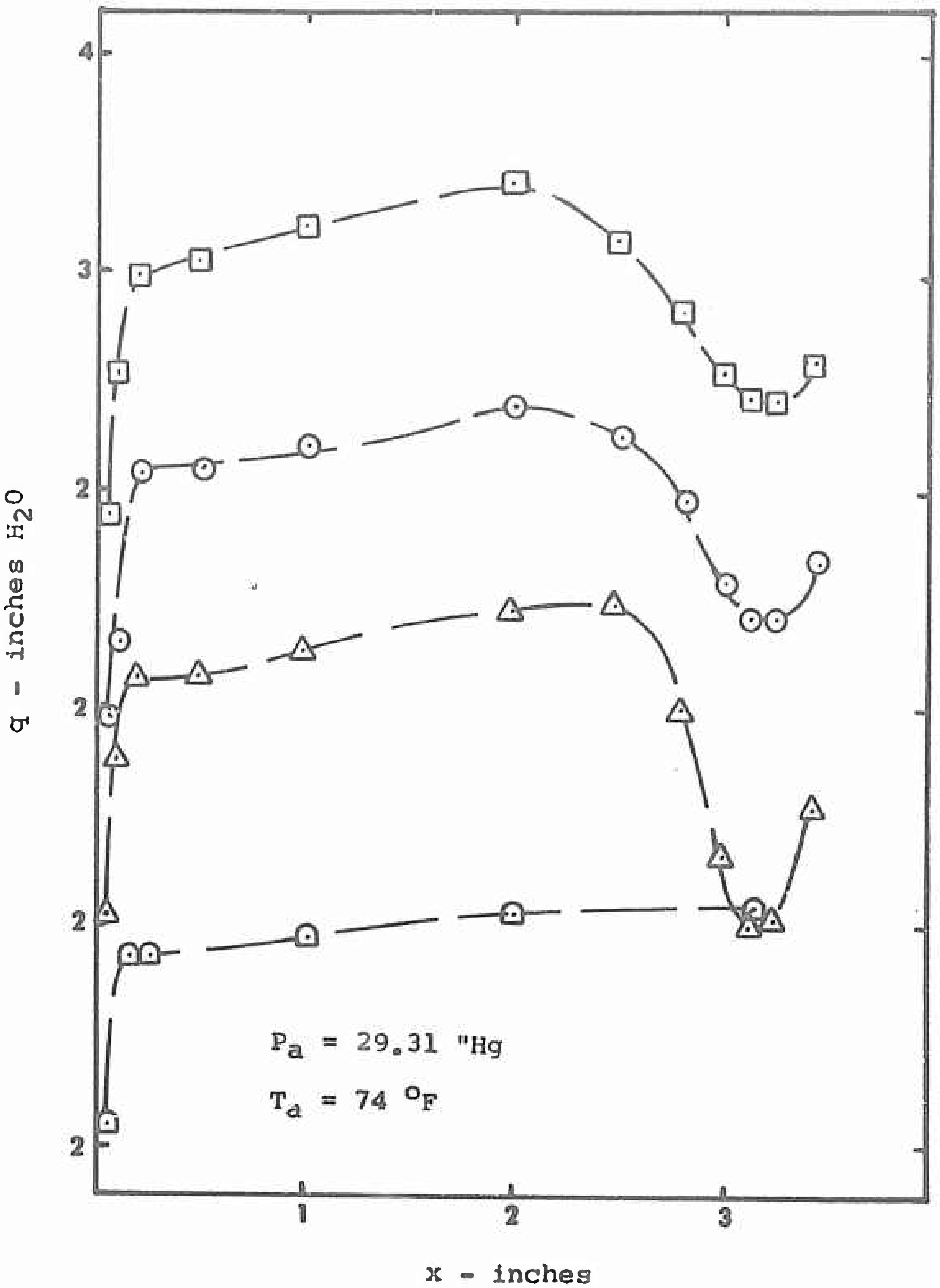

Figure 15

Dynamic Pressure vs. Distance from Wall

Cyl. A V = 119.6 fps I^2R/L = 0 Btu/hr-inch

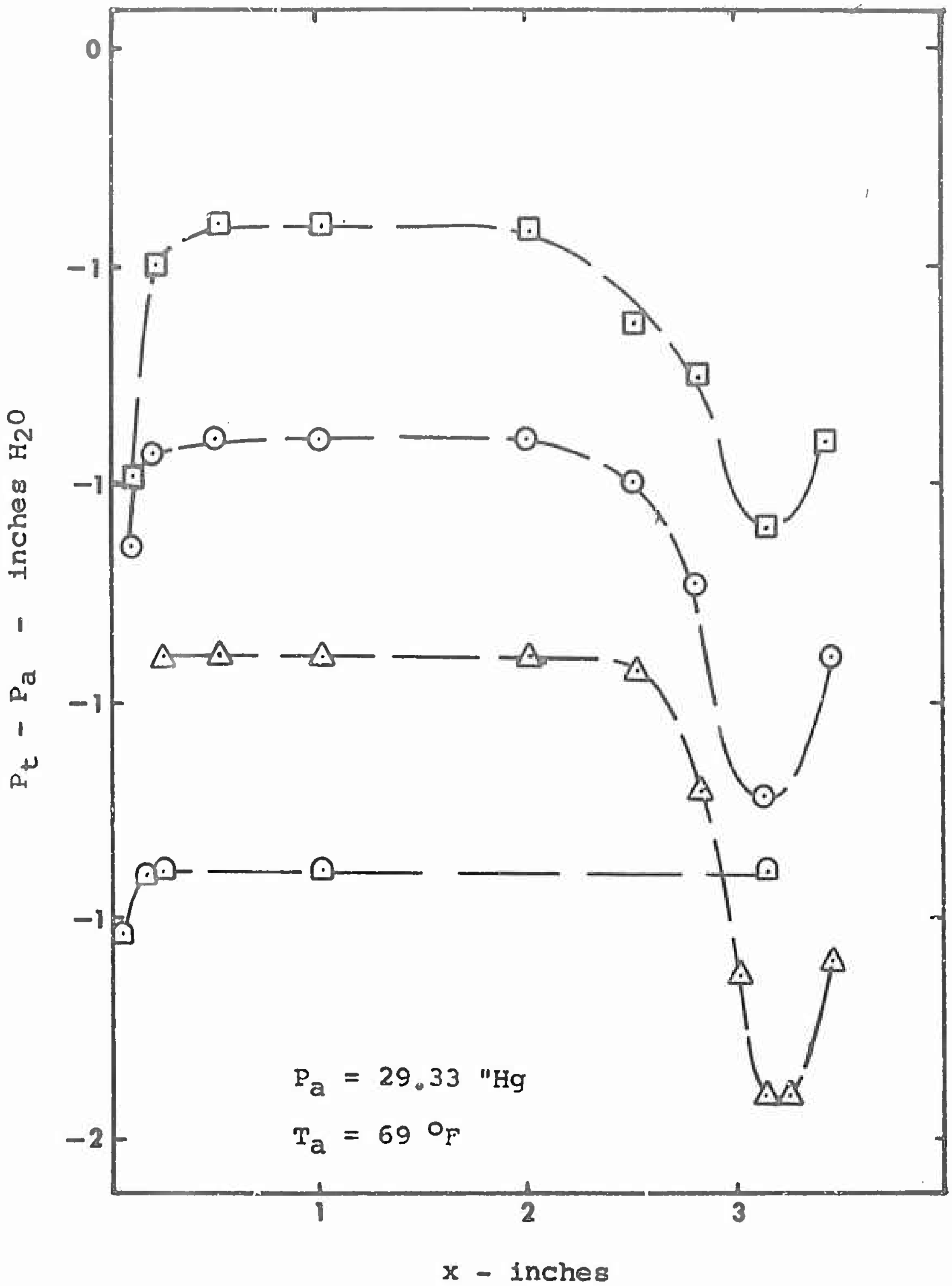

Figure 16

Total Pressure minus Atmospheric Pressure
vs. Distance from Wall

Cyl. A V = 119.4 fps I^2R/L = 127.0 Btu/hr-inch

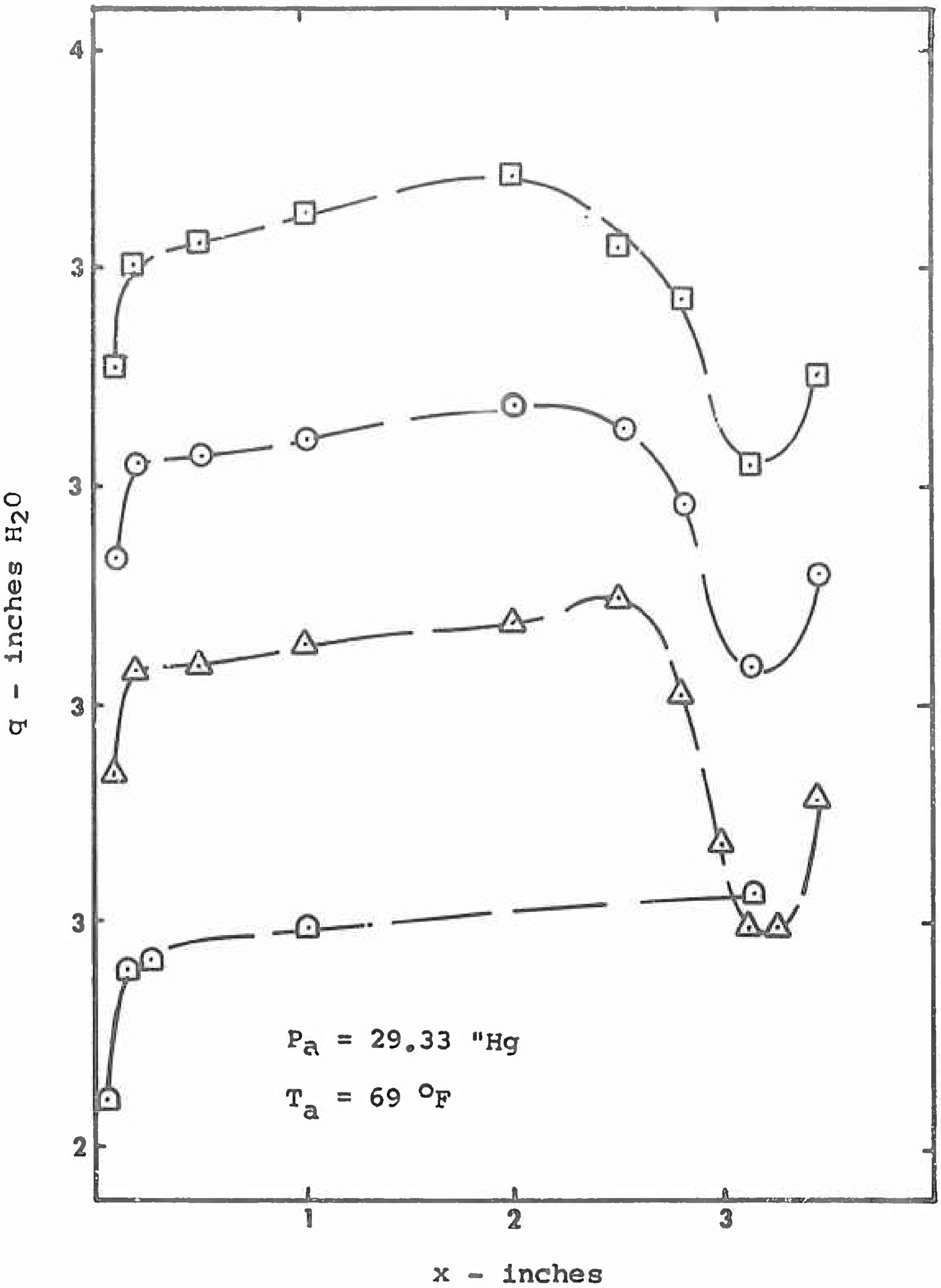

Figure 17

Dynamic Pressure vs. Distance from Wall

Cyl. A $V = 119.4$ fps $I^2R/L = 127.0$ Btu/hr-inch

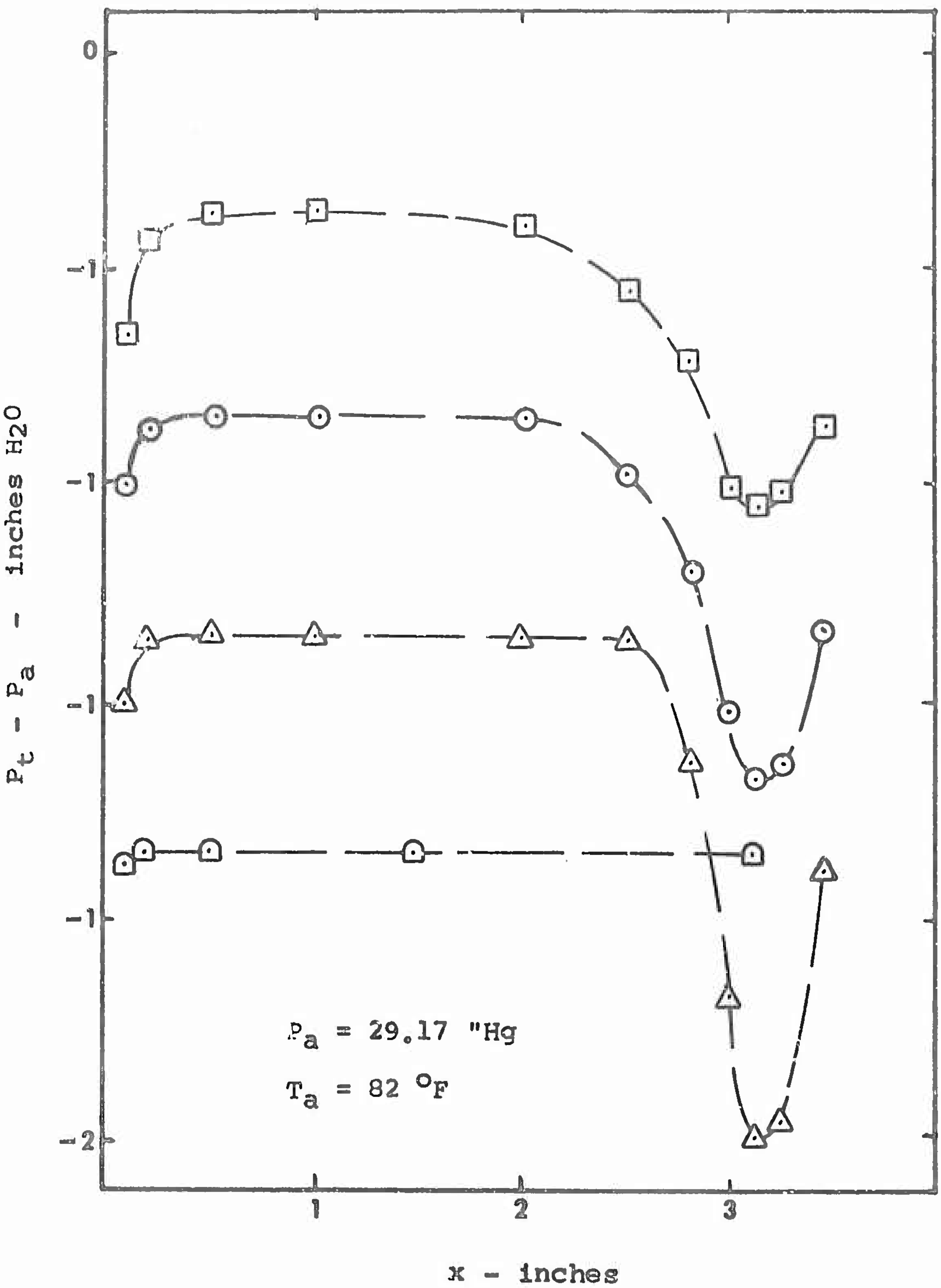

Figure 18

Total Pressure minus Atmospheric Pressure vs. Distance from Wall

Cyl. A V = 119.4 fps I^2R/L = 292.0 Btu/hr-inch

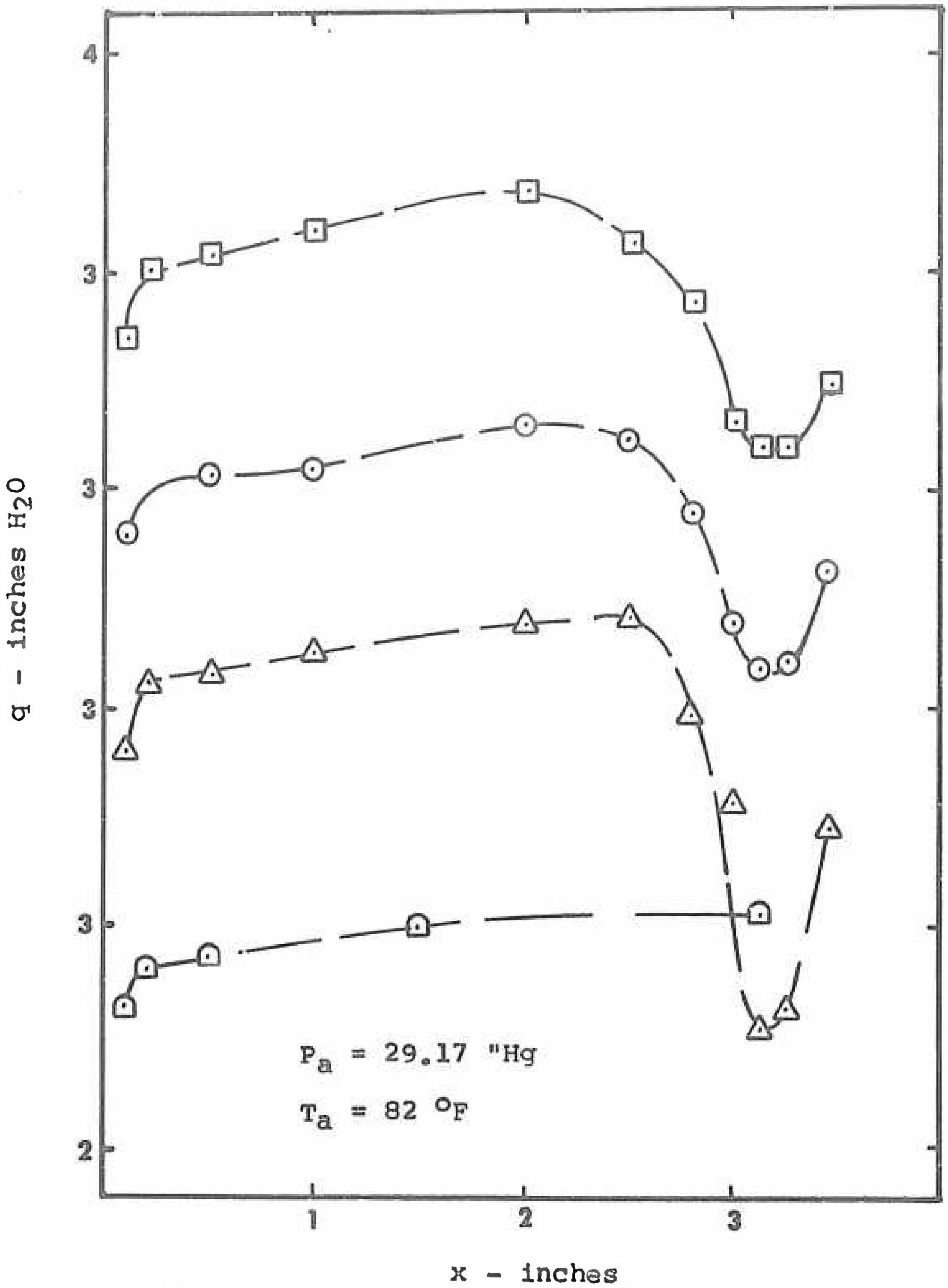

Figure 19

Dynamic Pressure vs. Distance from Wall

Cyl. A V = 119.4 fps I^2R/L = 292.0 Btu/hr-inch

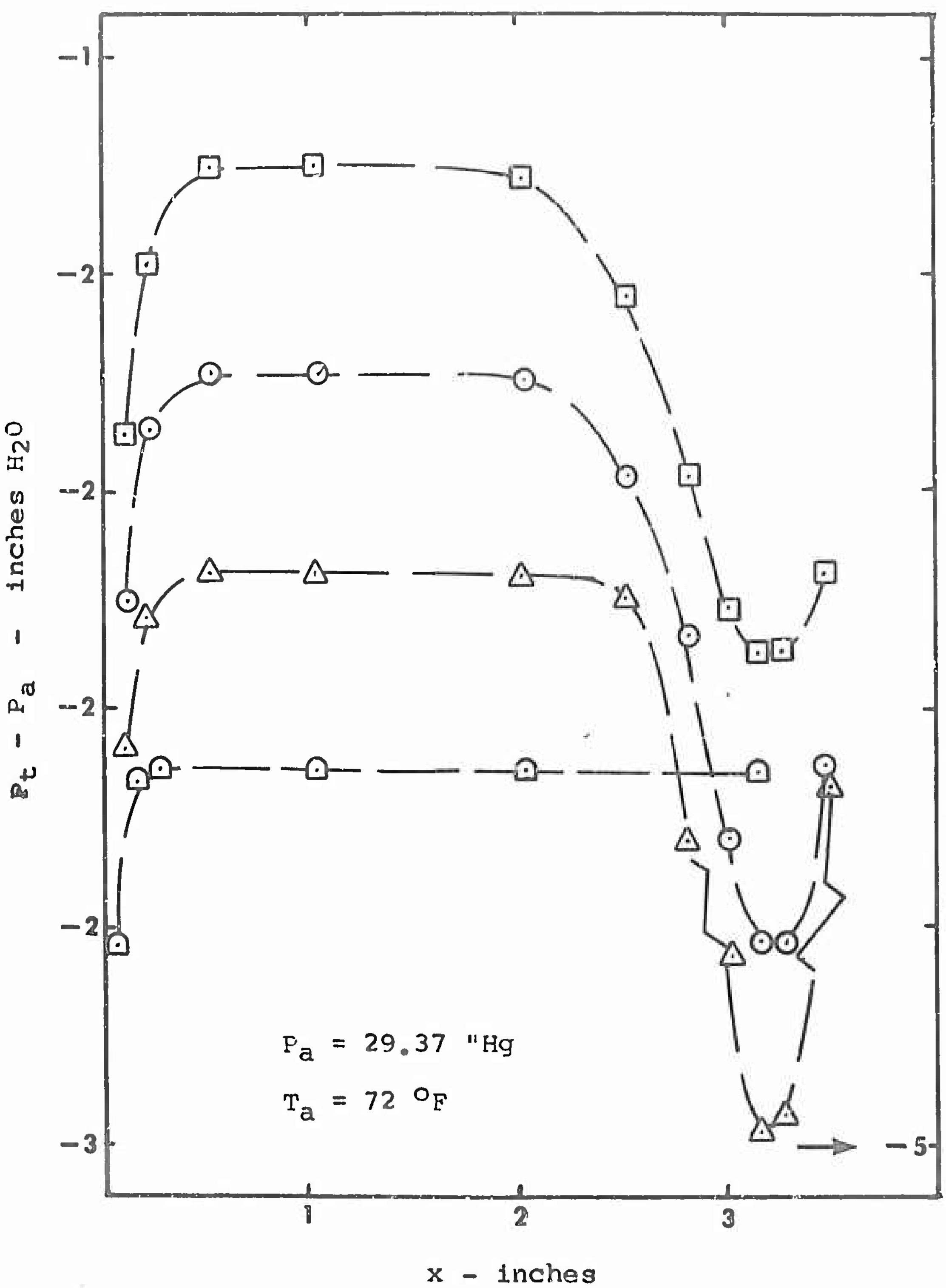

Figure 20

Total Pressure minus Atmospheric Pressure
vs. Distance from Wall

Cyl. A V = 159.2 fps I^2R/L = 0 Btu/hr-inch

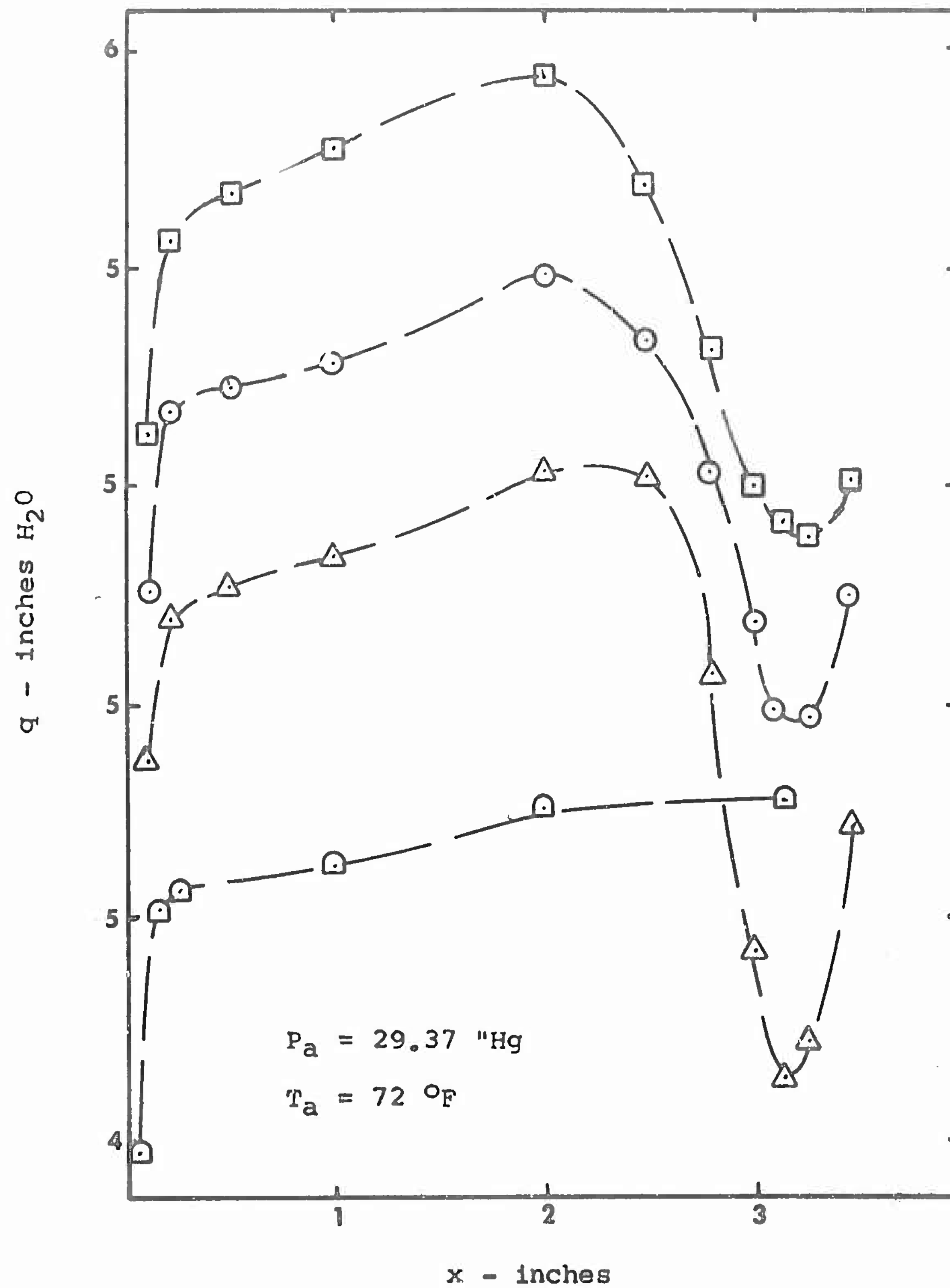

Figure 21

Dynamic Pressure vs. Distance from Wall

Cyl. A V = 159.2 fps I^2R/L = 0 Btu/hr-inch

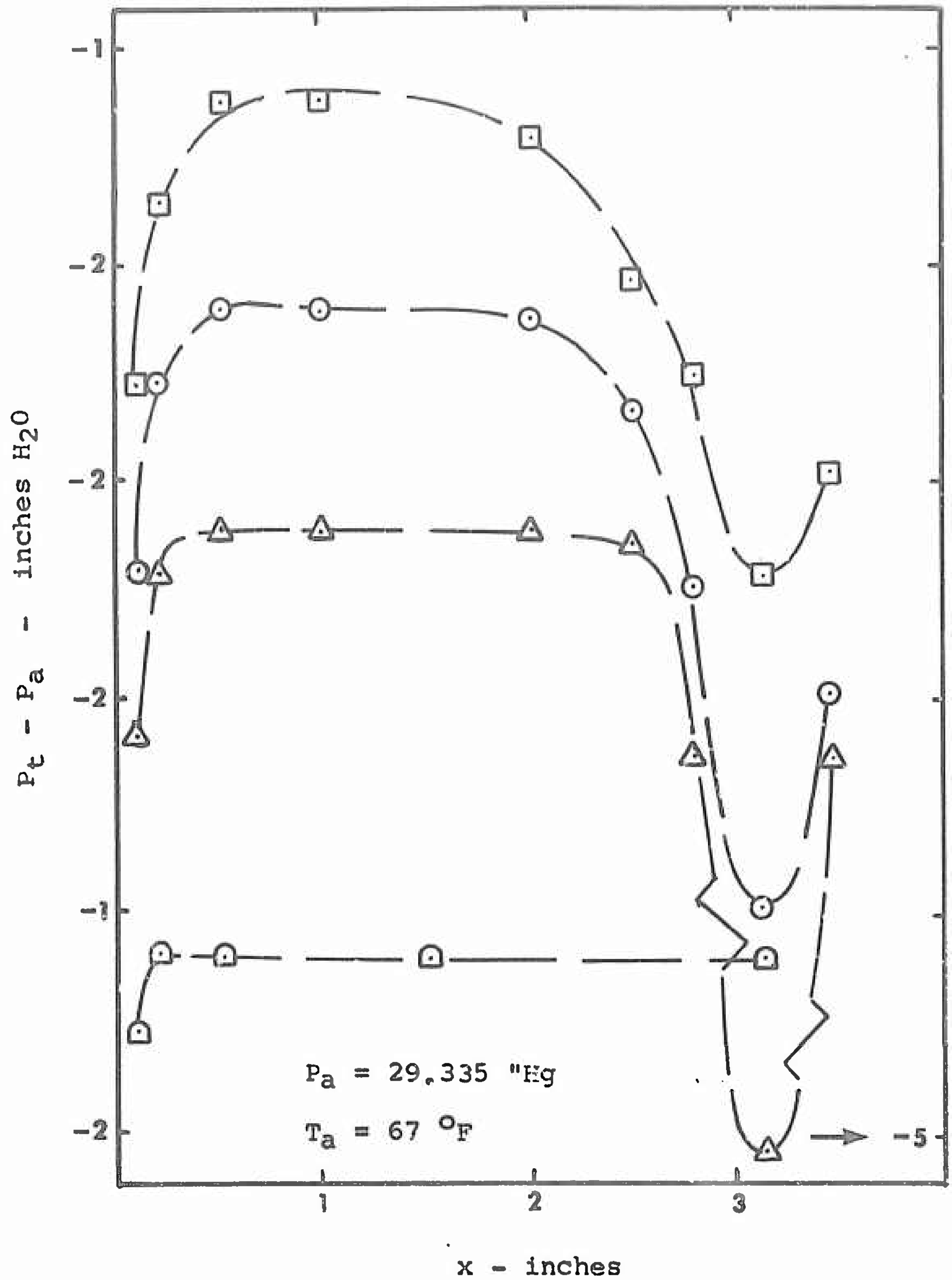

Figure 22

Total Pressure minus Atmospheric Pressure
vs. Distance from Wall

Cyl. A V = 161 fps I^2R/L = 126.7 Btu/hr-inch

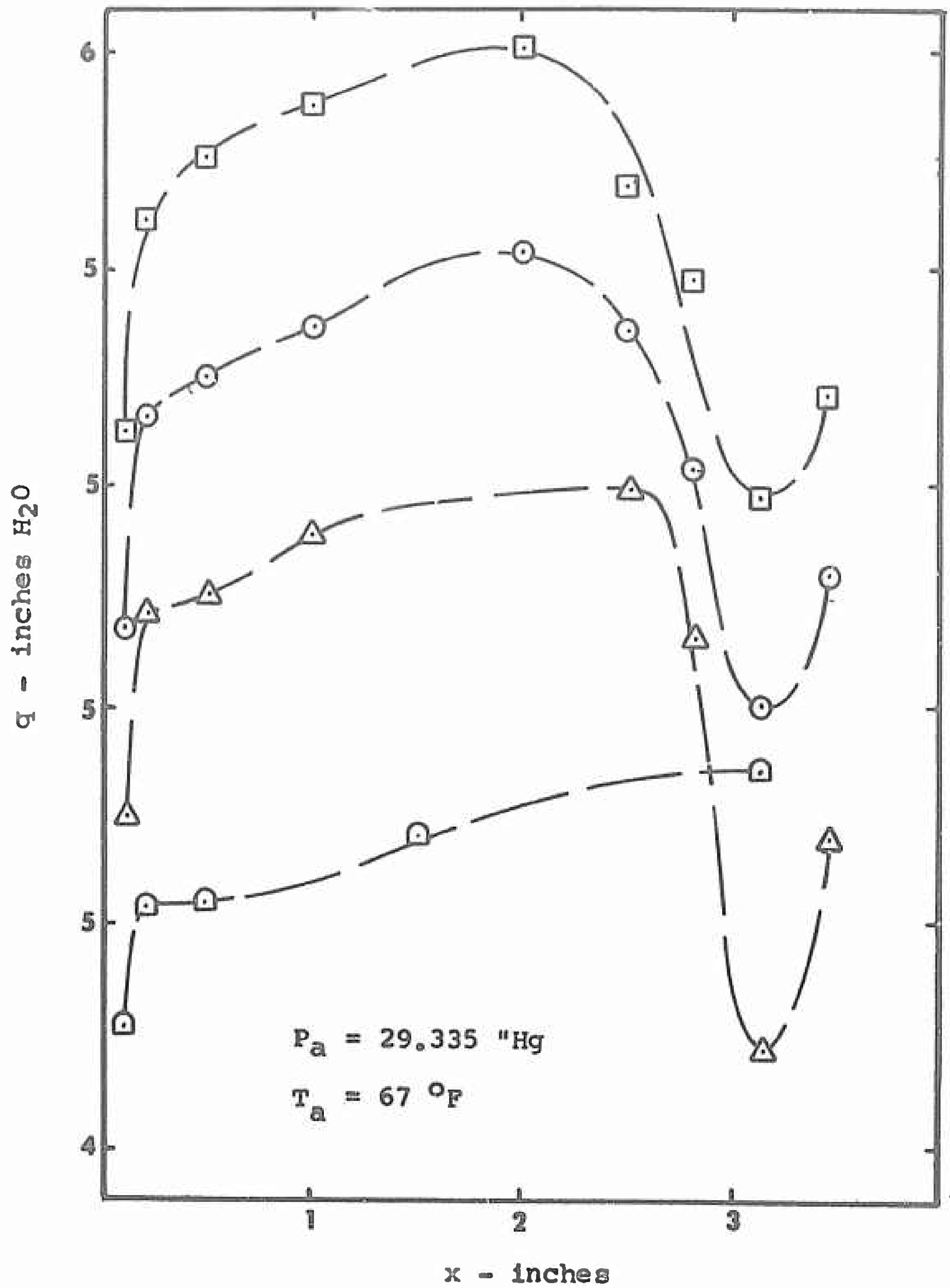

Figure 23

Dynamic Pressure vs. Distance from Wall

Cyl. A   V = 161 fps I^2R/L = 126.7 Btu/hr-inch

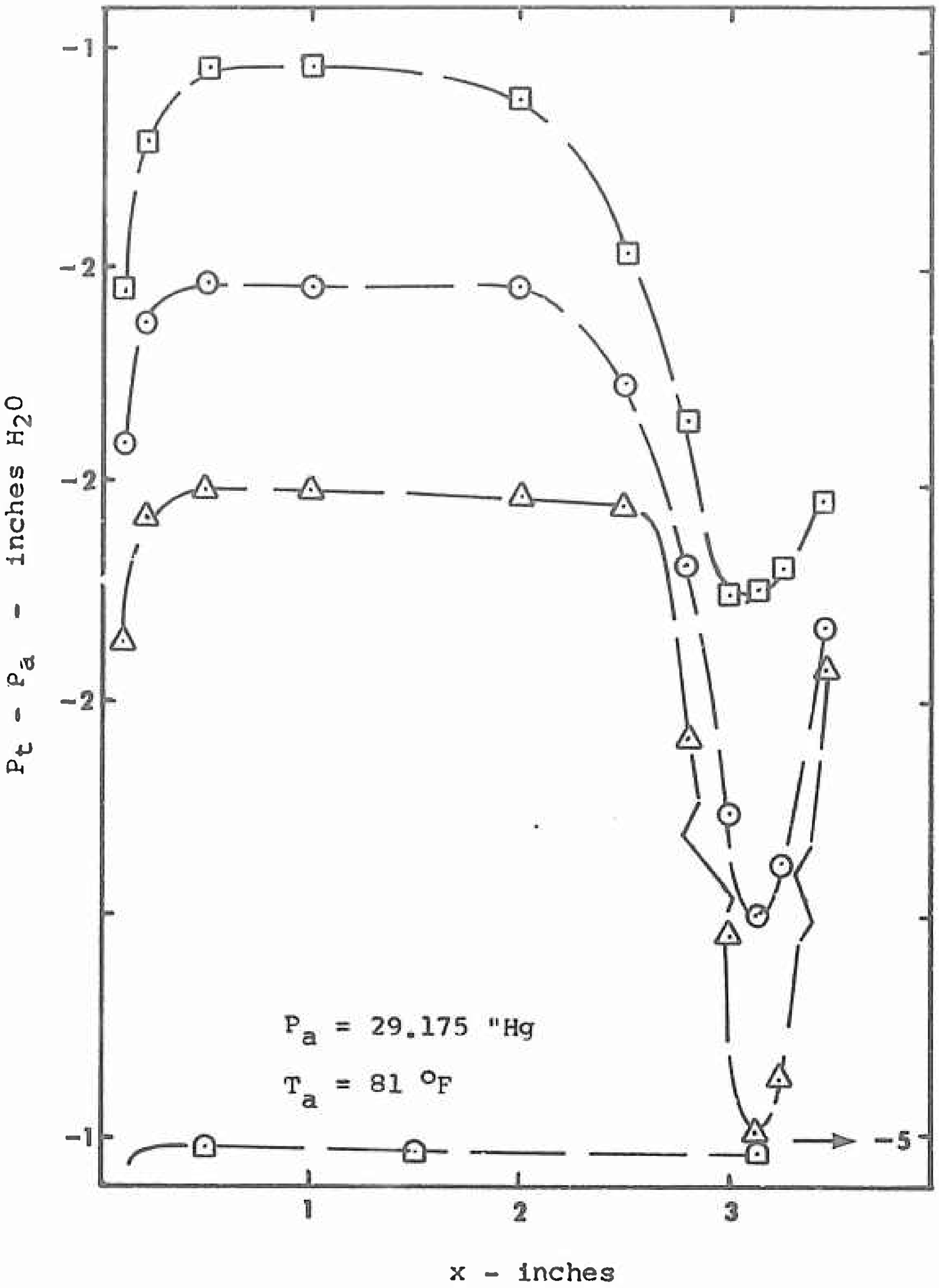

Figure 24

Total Pressure minus Atmospheric Pressure
vs. Distance from Wall

Cyl. A V = 158.1 fps I^2R/L = 290.5 Btu/hr-inch

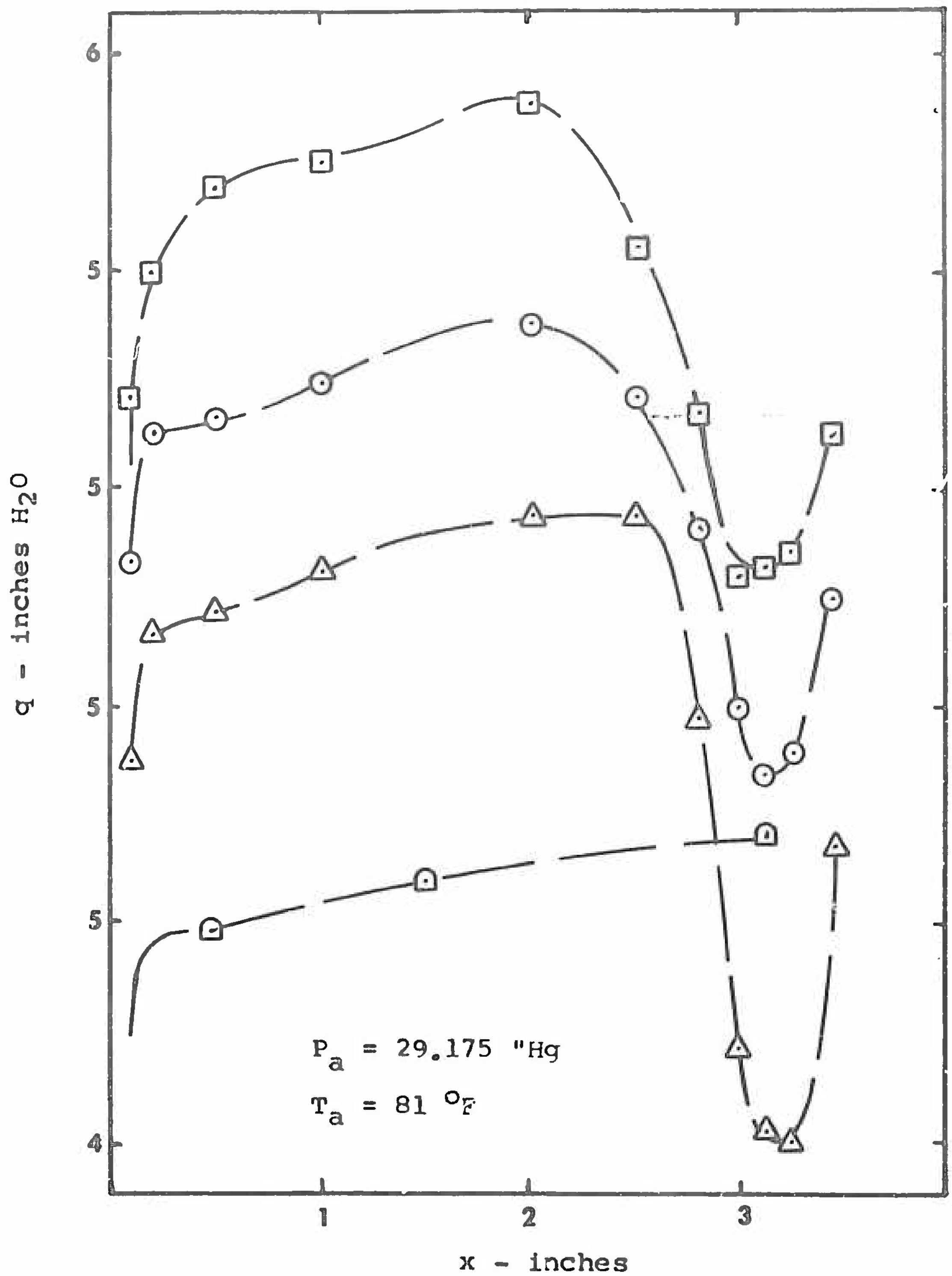

Figure 25

Dynamic Pressure vs. Distance from Wall

Cyl. A V = 158.1 fps I^2R/L = 290.5 Btu/hr-inch

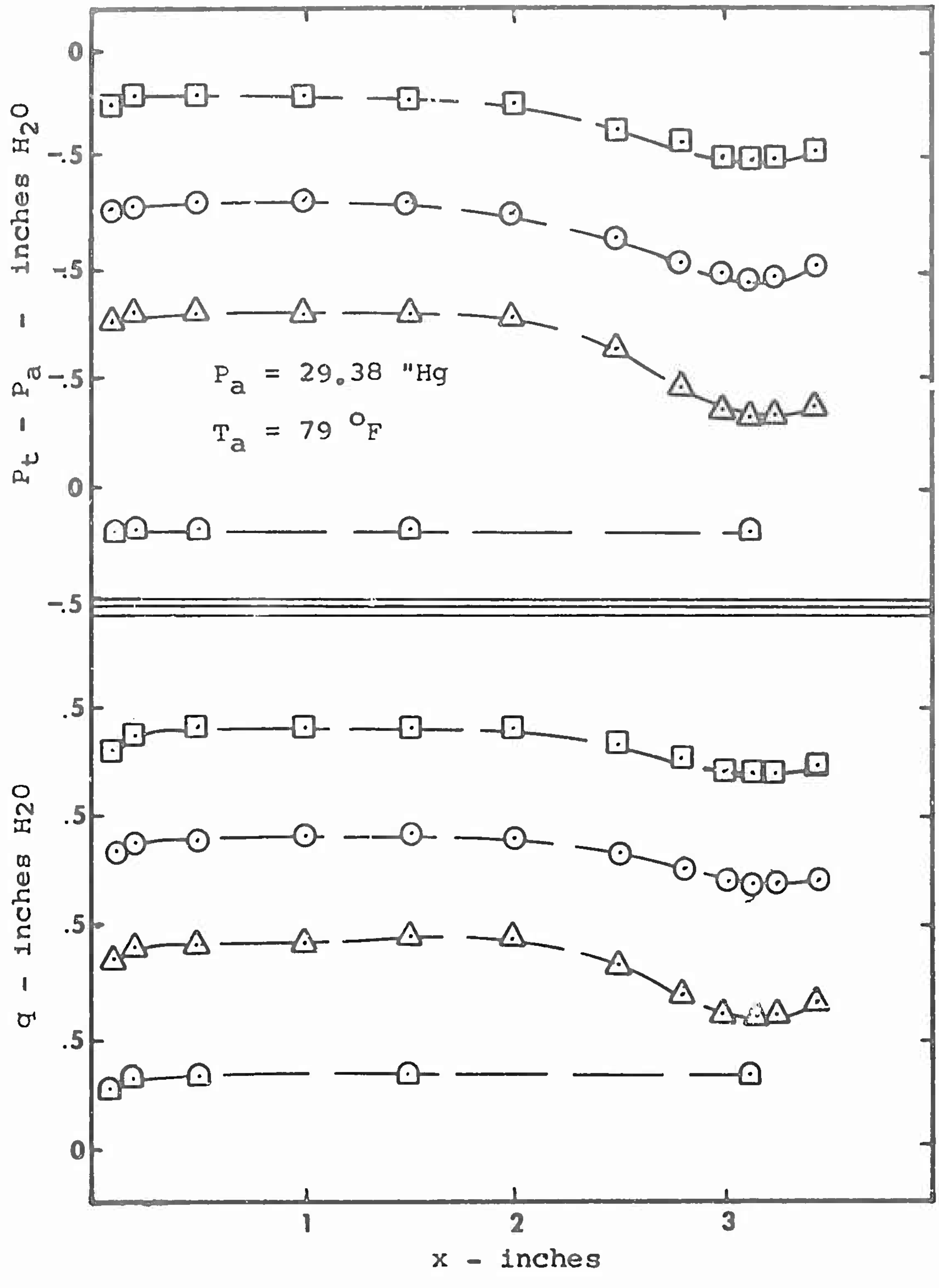

Figures 26 and 27

Total Pressure minus Atmospheric Pressure vs. Distance from Wall and

Dynamic Pressure vs. Distance from Wall

Cyl. C V = 40.2 fps I^2R/L = 0 Btu/hr-inch

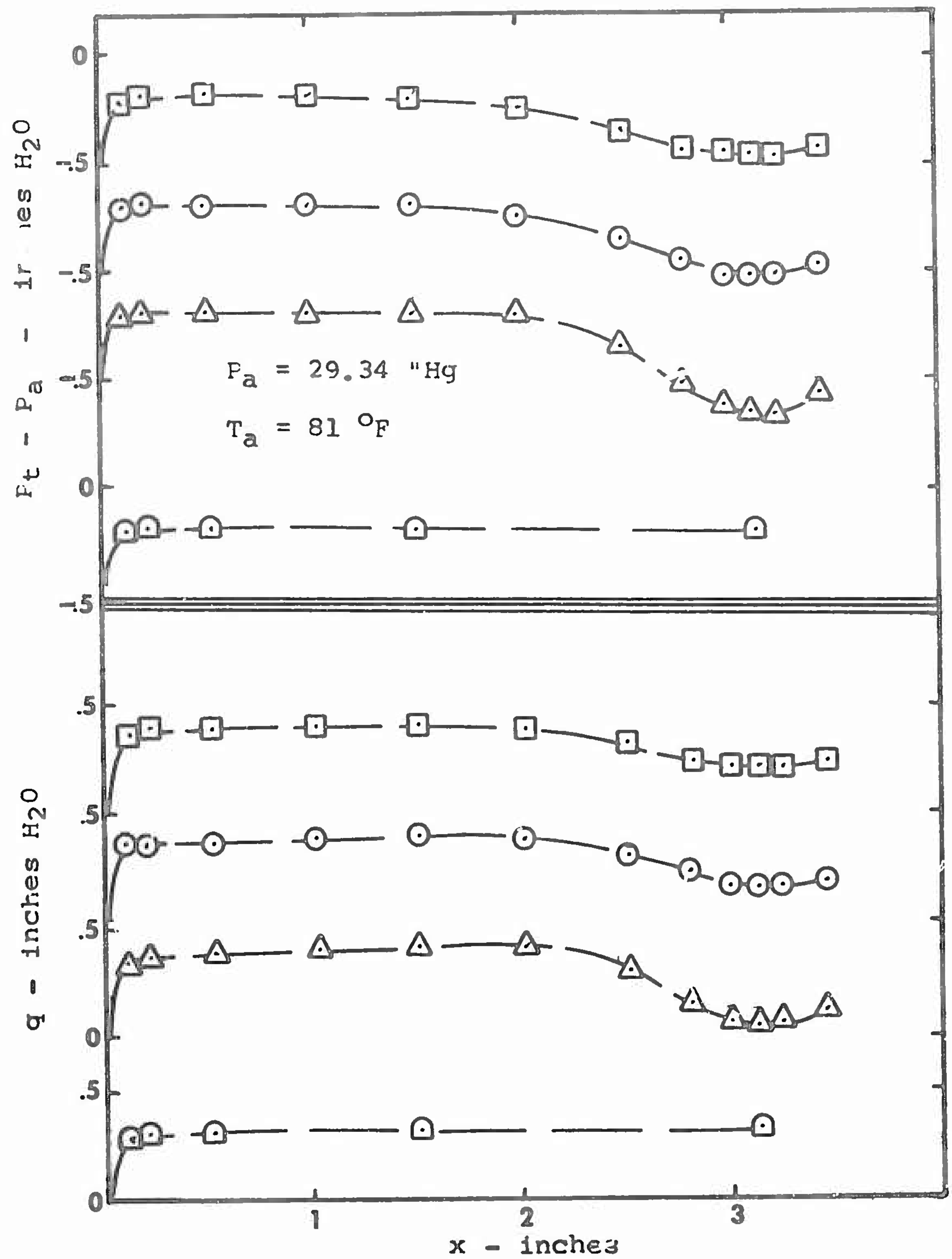

Figures 28 and 29

Total Pressure minus Atmospheric Pressure
vs. Distance from Wall and

Dynamic Pressure vs. Distance from Wall

Cyl. C V = 39.4 fps I^2R/L = 263.5 Btu/hr-inch

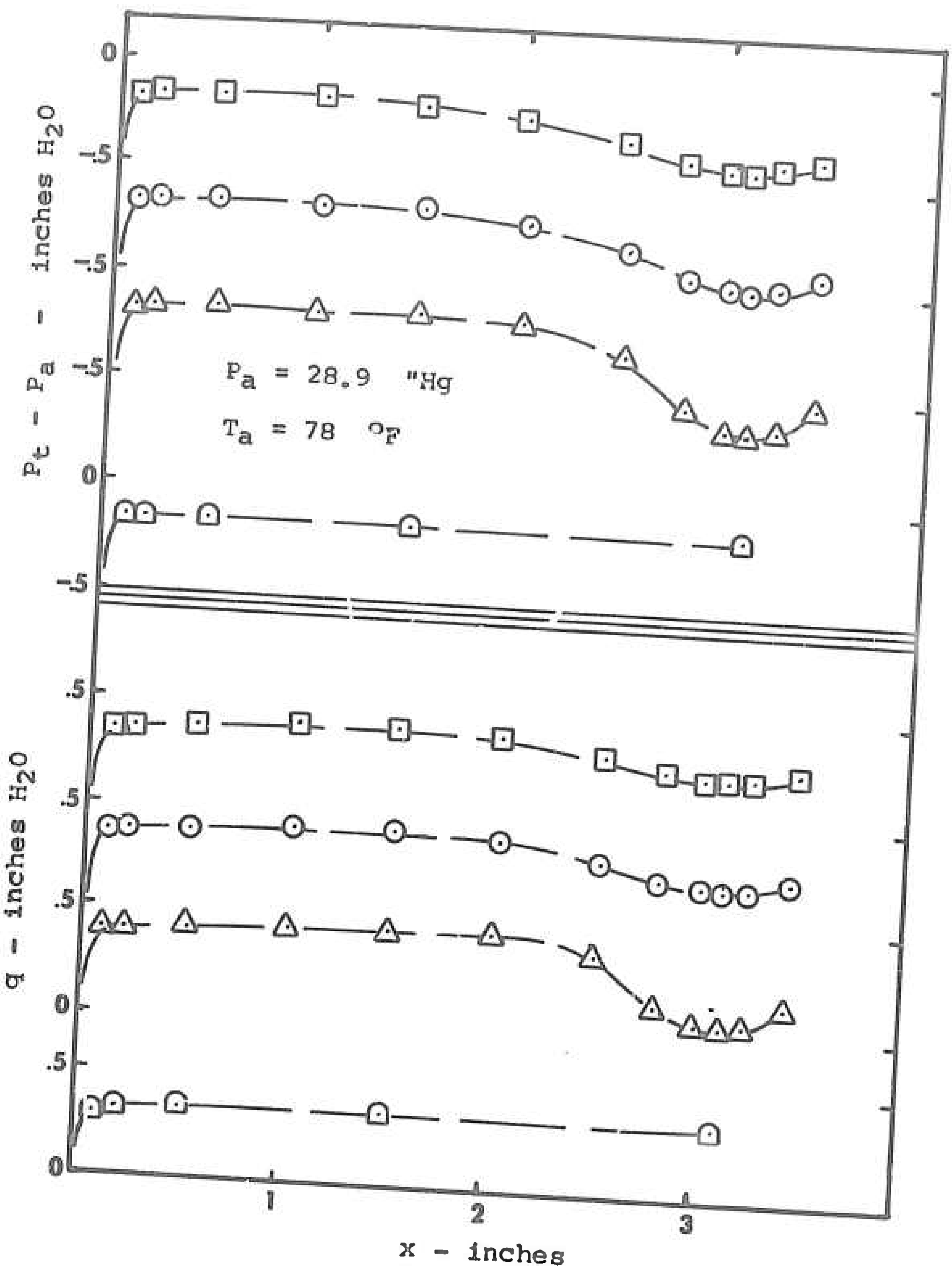

Figures 30 and 31

Total Pressure minus Atmospheric Pressure vs. Distance from Wall and

Dynamic Pressure vs. Distance from Wall

Cyl. A V = 40 fps I^2R/L = 597.0 Btu/hr-inch

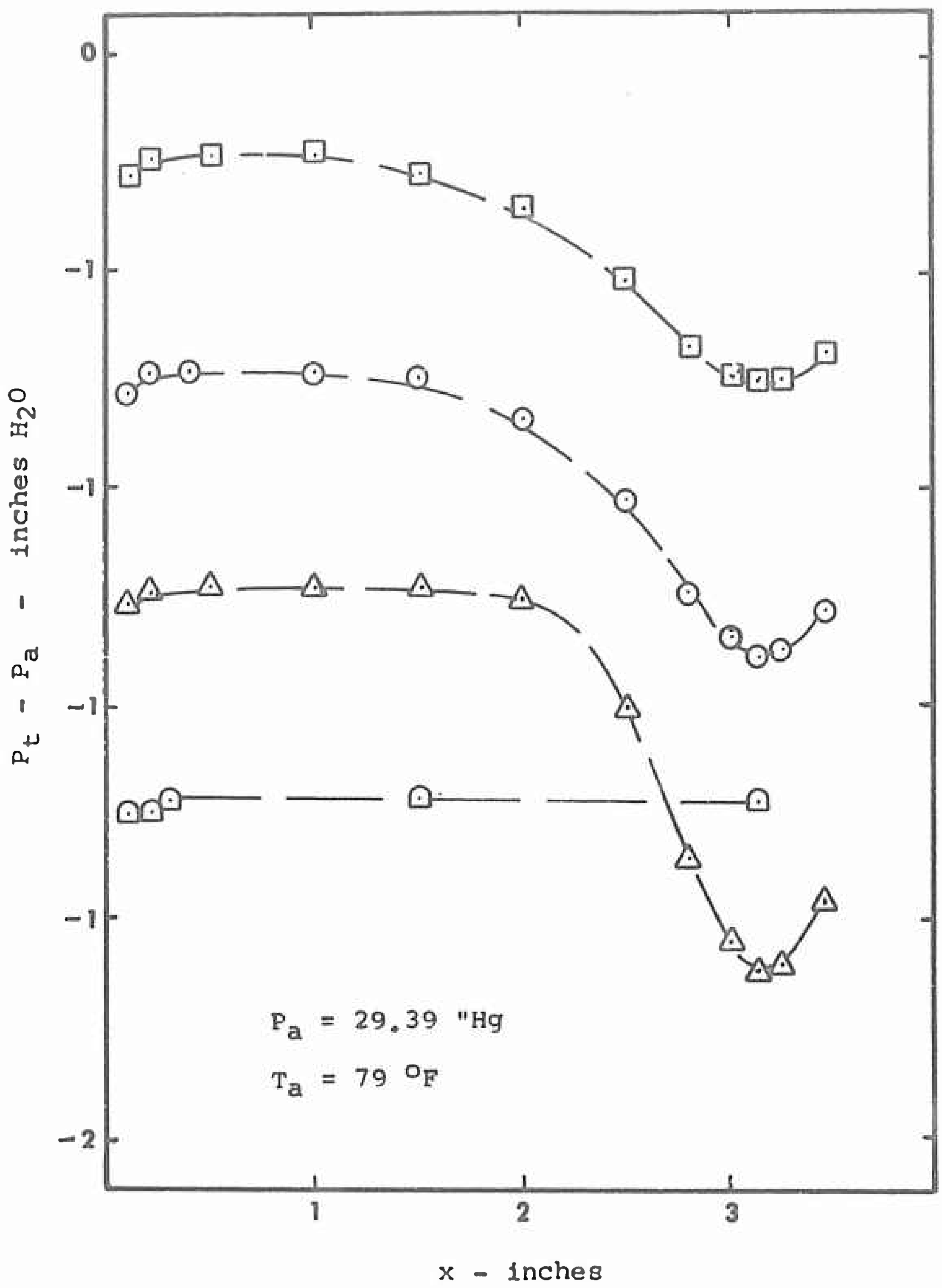

Figure 32

Total Pressure minus Atmospheric Pressure
vs. Distance from Wall

Cyl. C V = 79.1 fps I^2R/L = 0 Btu/hr-inch

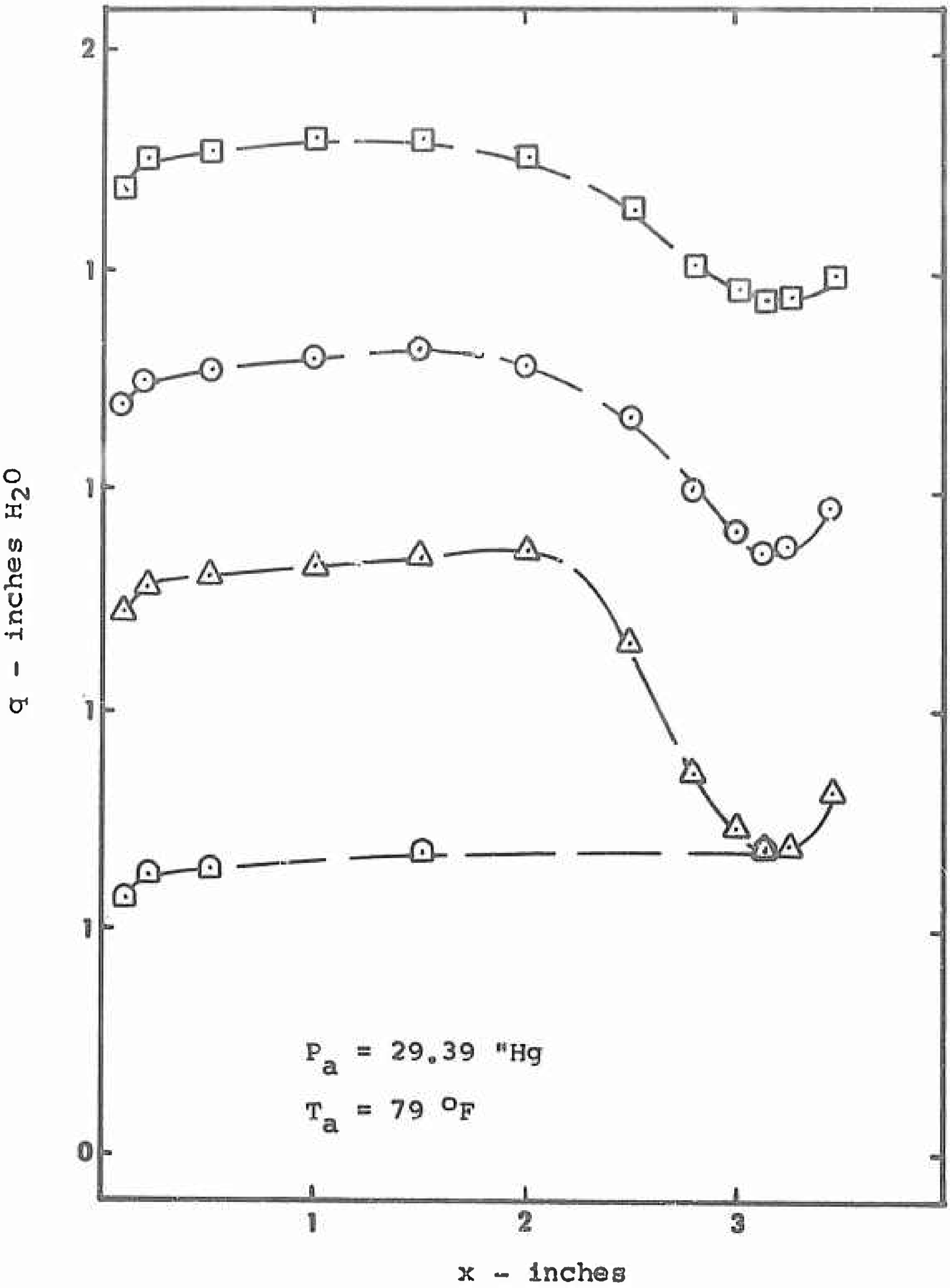

Figure 33

Dynamic Pressure vs. Distance from Wall

Cyl. C V = 79.1 fps I^2R/L = 0 Btu/hr-inch

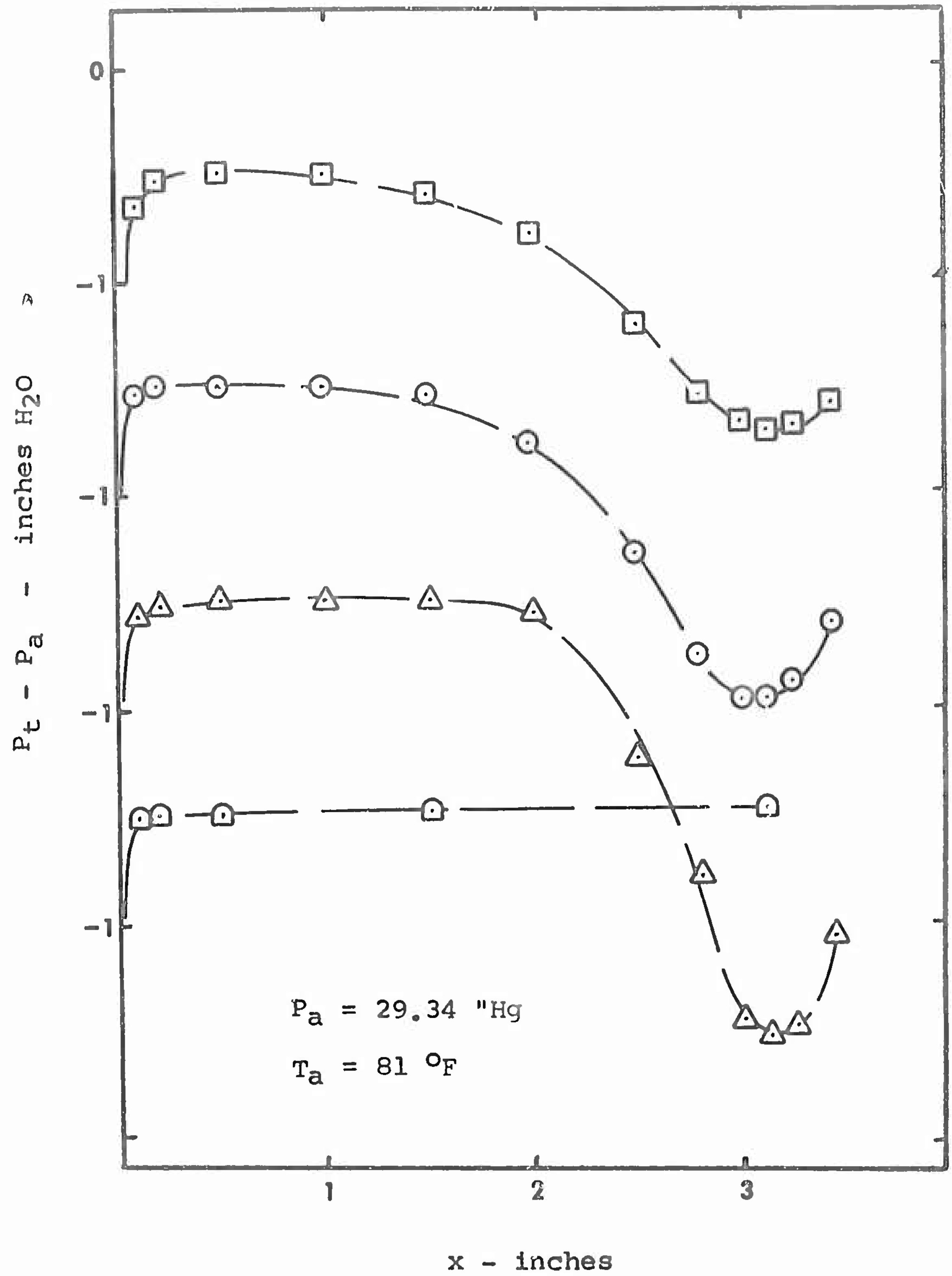

Figure 34

Total Pressure minus Atmospheric Pressure
vs. Distance from Wall

Cyl. C   V = 82.6 fps I^2R/L = 261.0 Btu/hr-inch

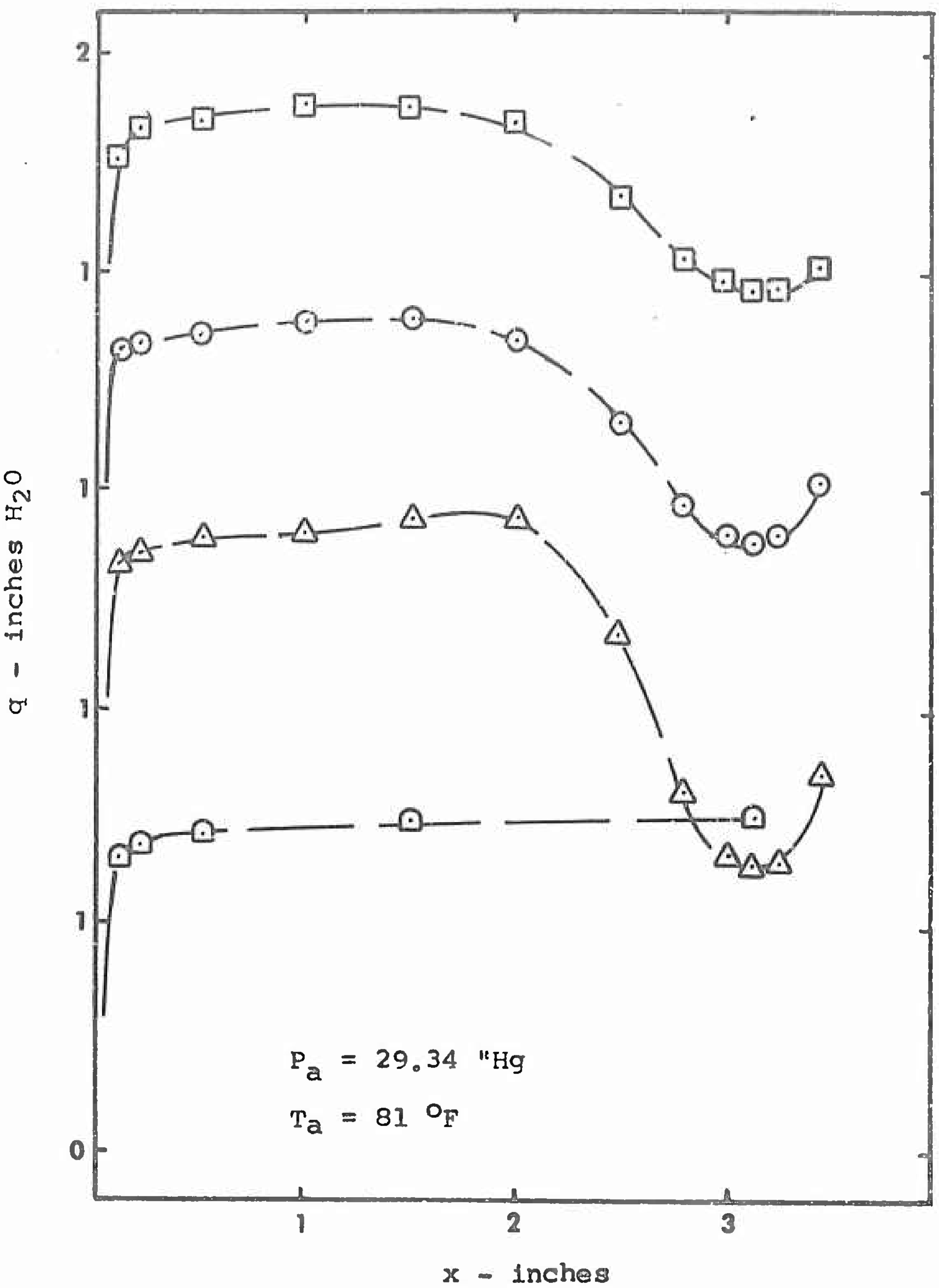

Figure 35

Dynamic Pressure vs. Distance from Wall

Cyl. C V = 82.6 fps I^2R/L = 261.0 Btu/hr-inch

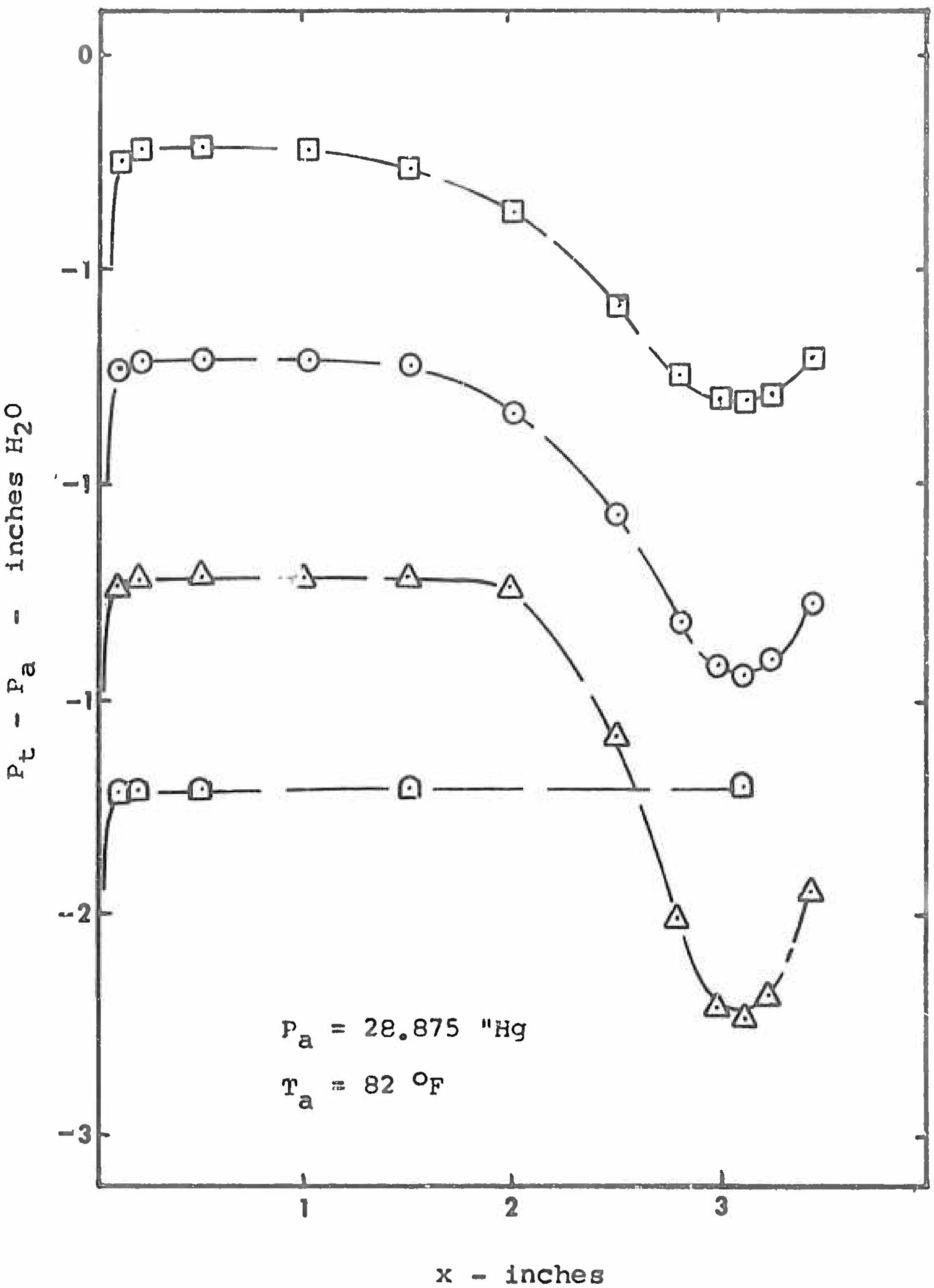

Figure 36

Total Pressure minus Atmospheric Pressure
vs. Distance from Wall

Cyl. C $\quad$ V = 82.6 fps $\quad$ I^2R/L = 598.0 Btu/hr-inch

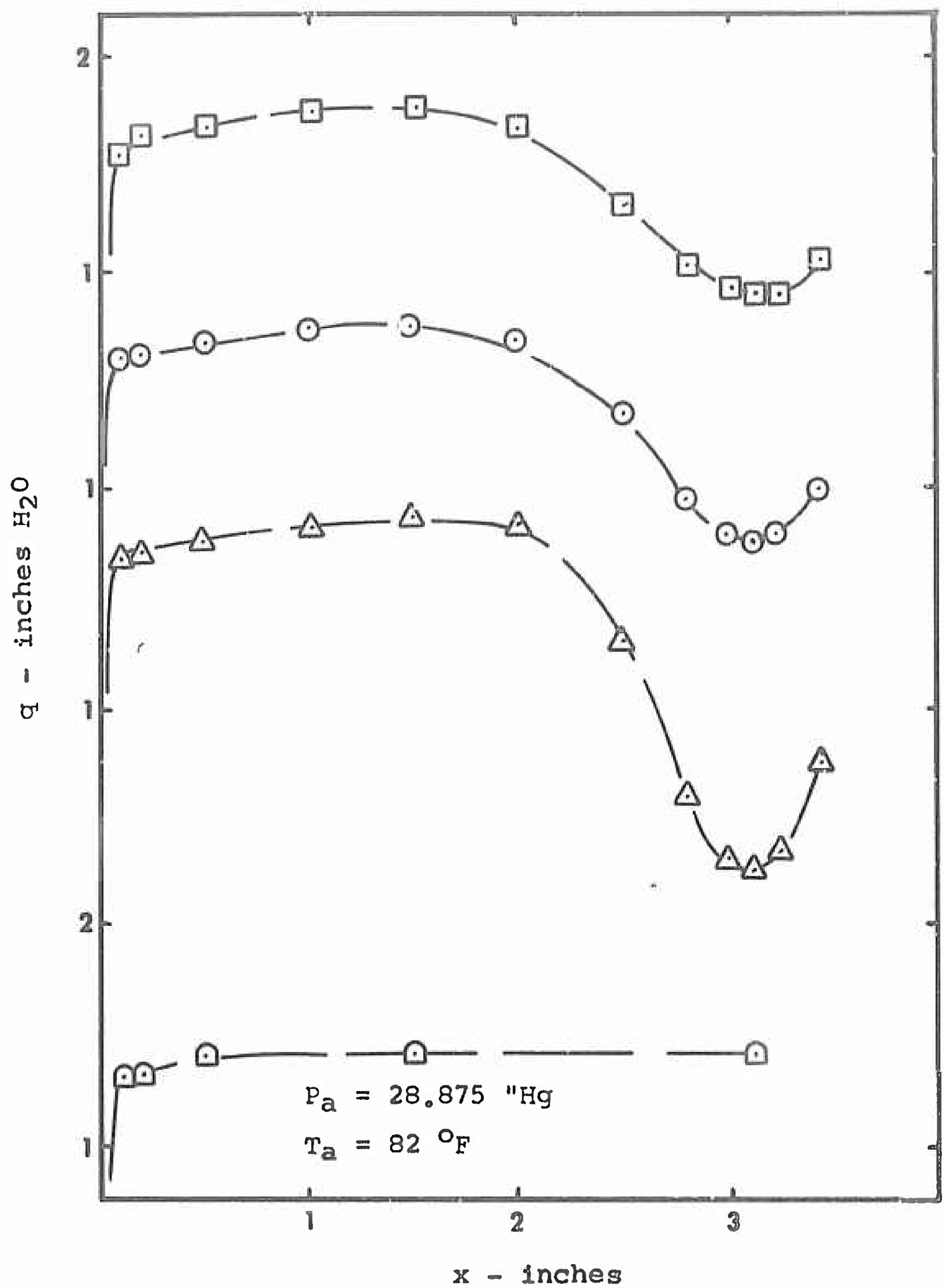

Figure 37

Dynamic Pressure vs. Distance from Wall

Cyl. C V = 82.6 fps I^2R/L = 598.0 Btu/hr-inch

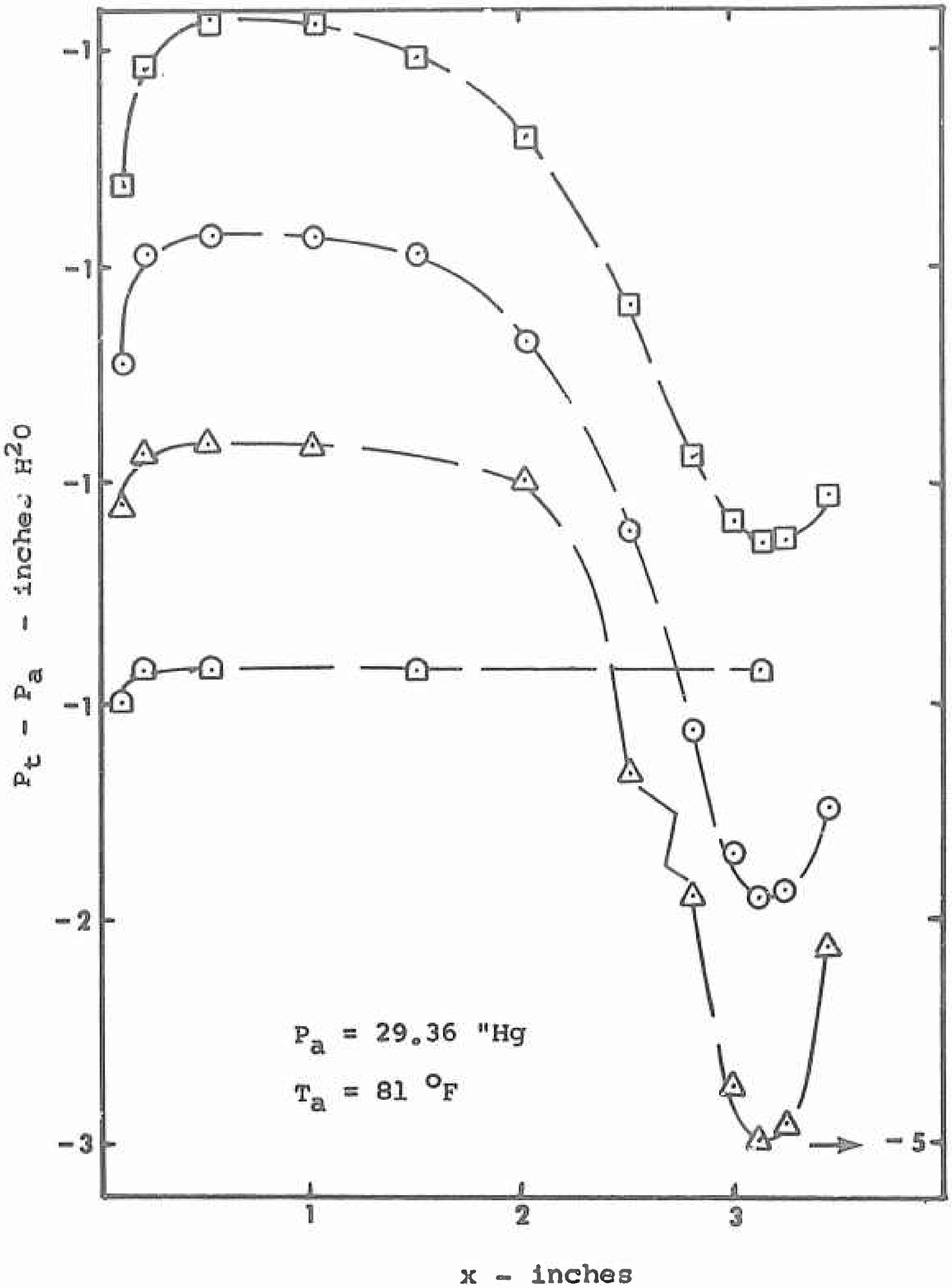

Figure 38

Total Pressure minus Atmospheric Pressure
vs. Distance from Wall

Cyl. C V = 123 fps I^2R/L = 0 Btu/hr-inch

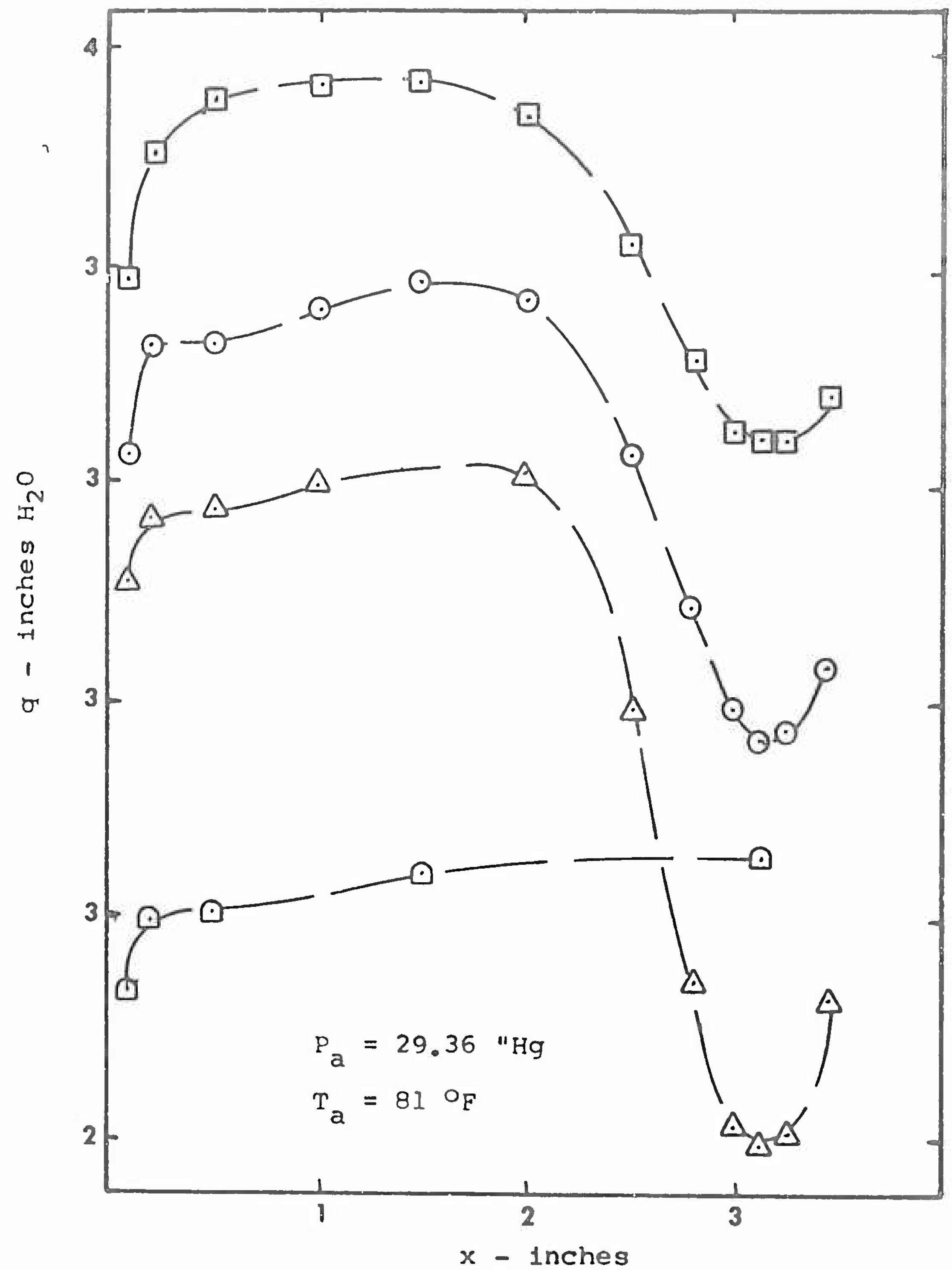

Figure 39

Dynamic Pressure vs. Distance from Wall

Cyl. C V = 123 fps I^2R/L = 0 Btu/hr-inch

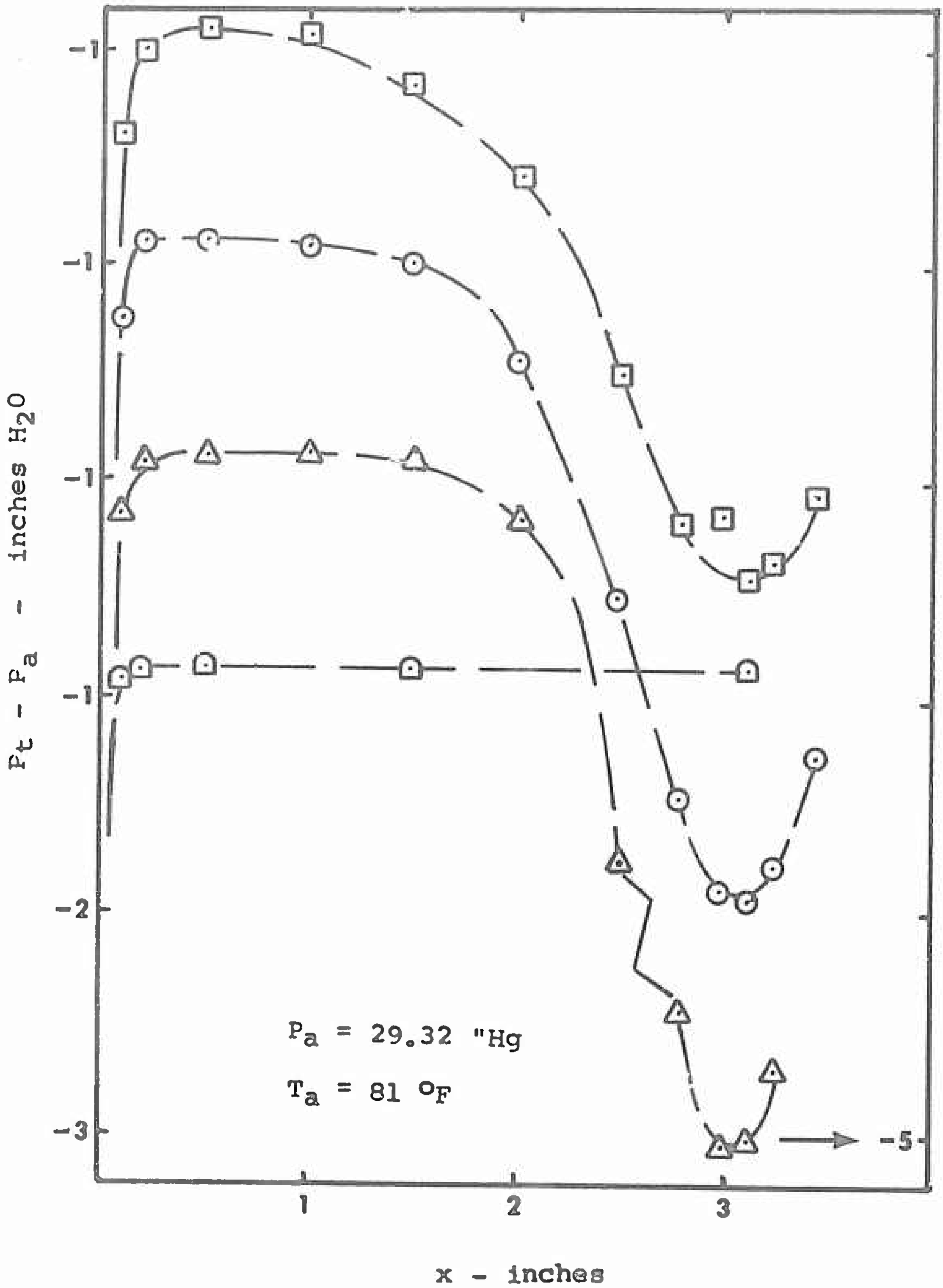

Figure 40

Total Pressure minus Atmospheric Pressure
vs. Distance from Wall

Cyl. C V = 124.6 fps I^2R/L = 260.5 Btu/hr-inch

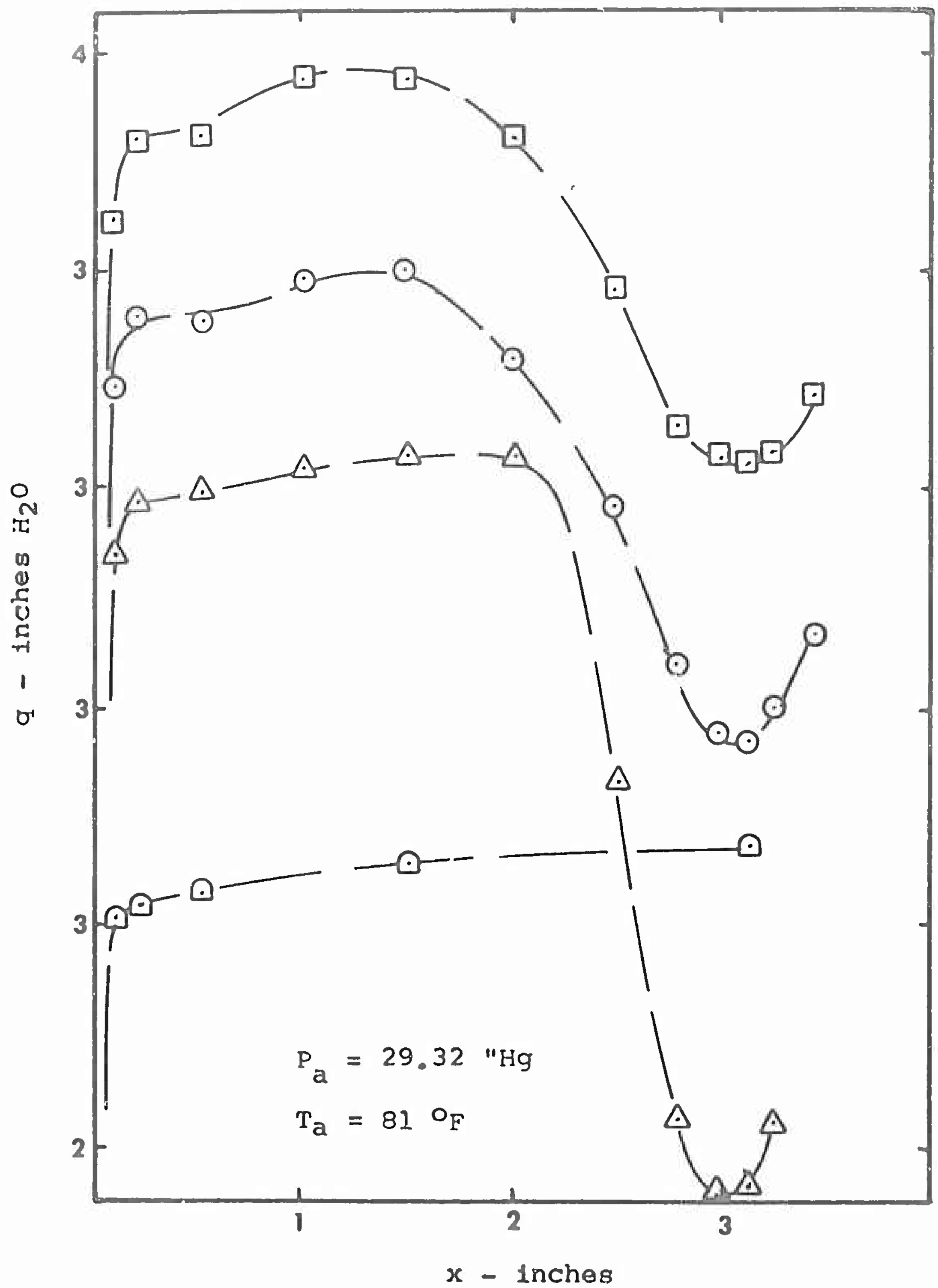

Figure 41

Dynamic Pressure vs. Distance from Wall

Cyl. C V = 124.6 fps . I^2R/L = 260.5 Btu/hr-inch

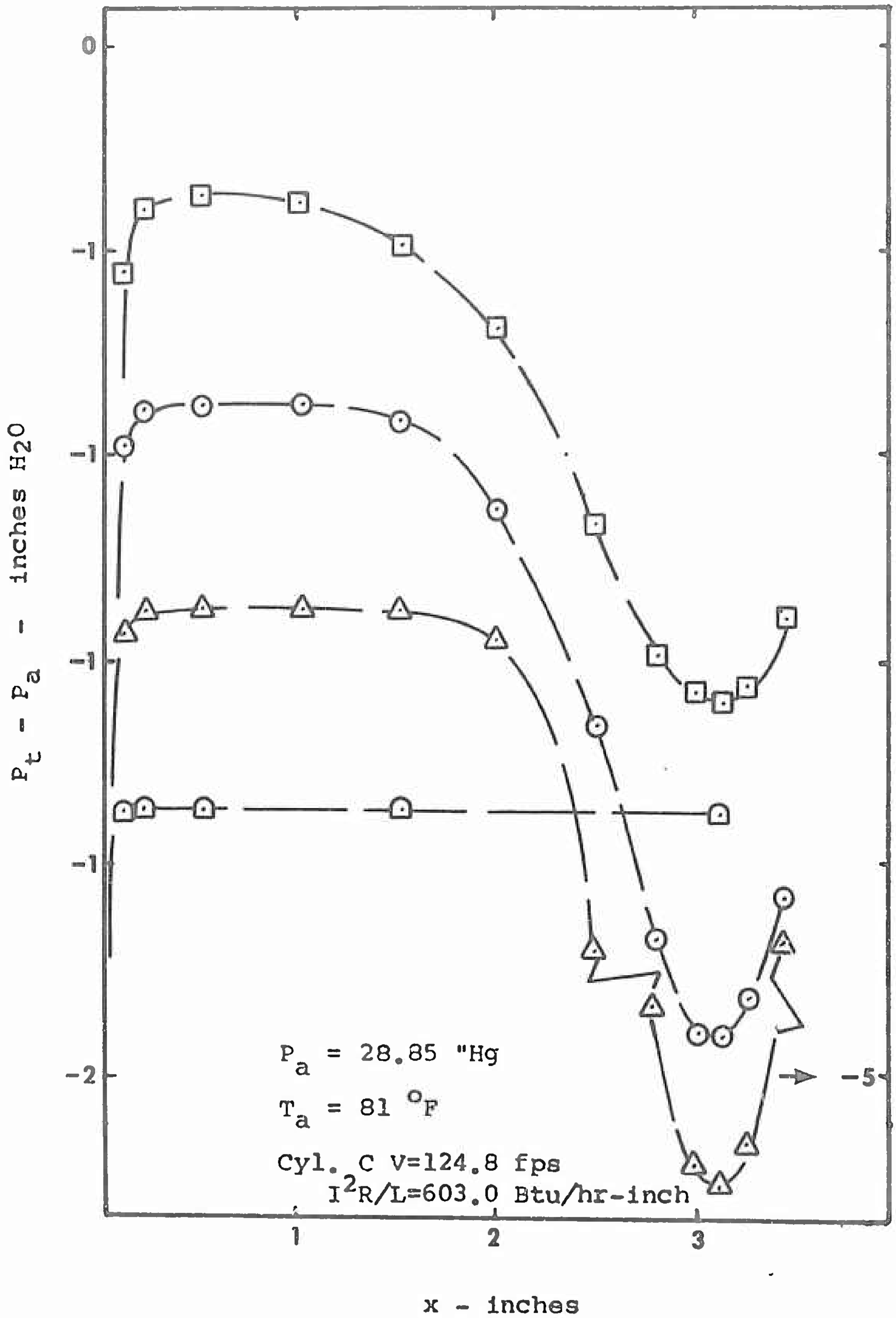

Figure 42

Total Pressure minus Atmospheric Pressure
vs. Distance from Wall

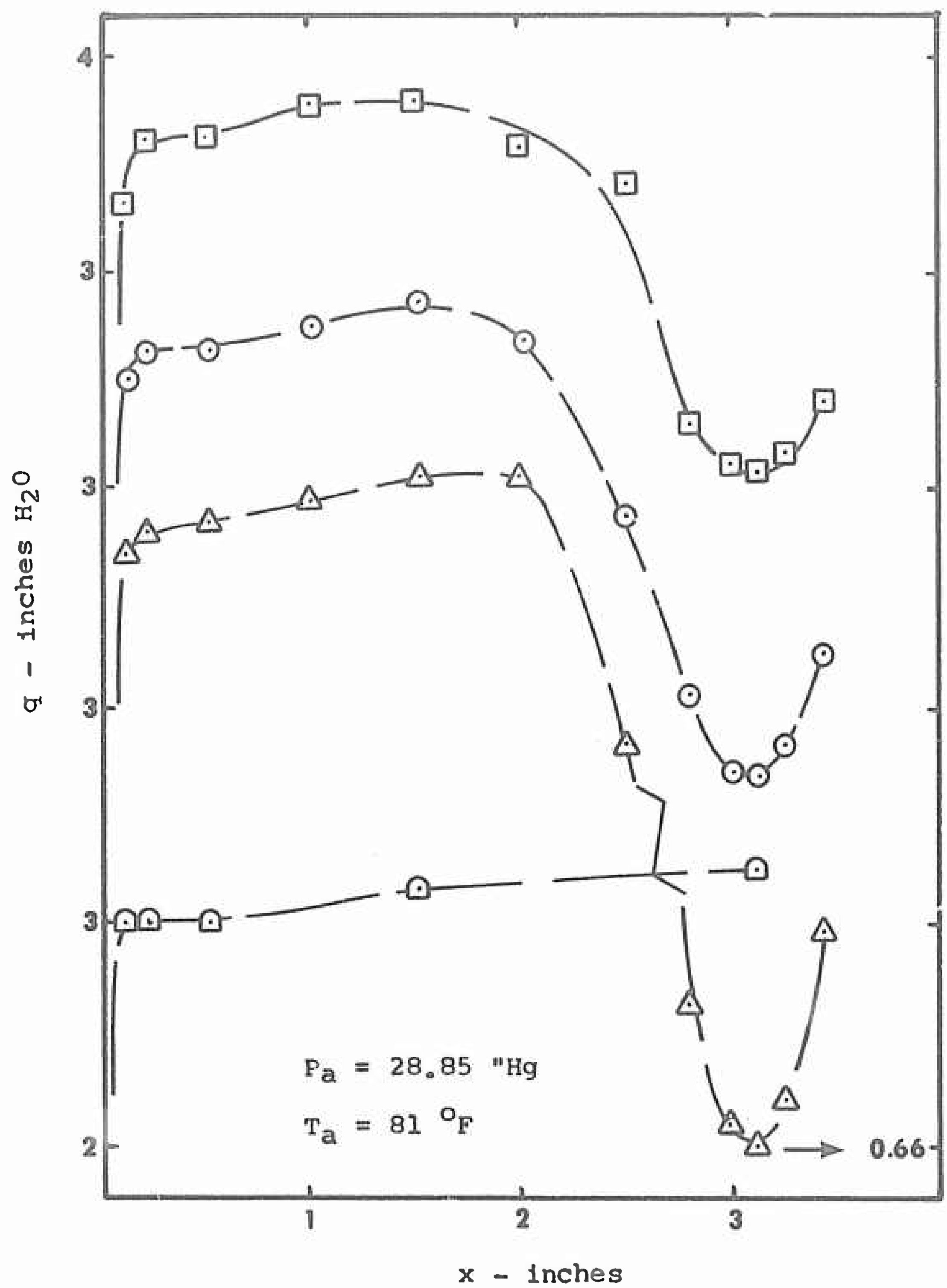

Figure 43

Dynamic Pressure vs. Distance from Wall

Cyl. C V = 124.8 fps I^2R/L = 603.0 Btu/hr-inch

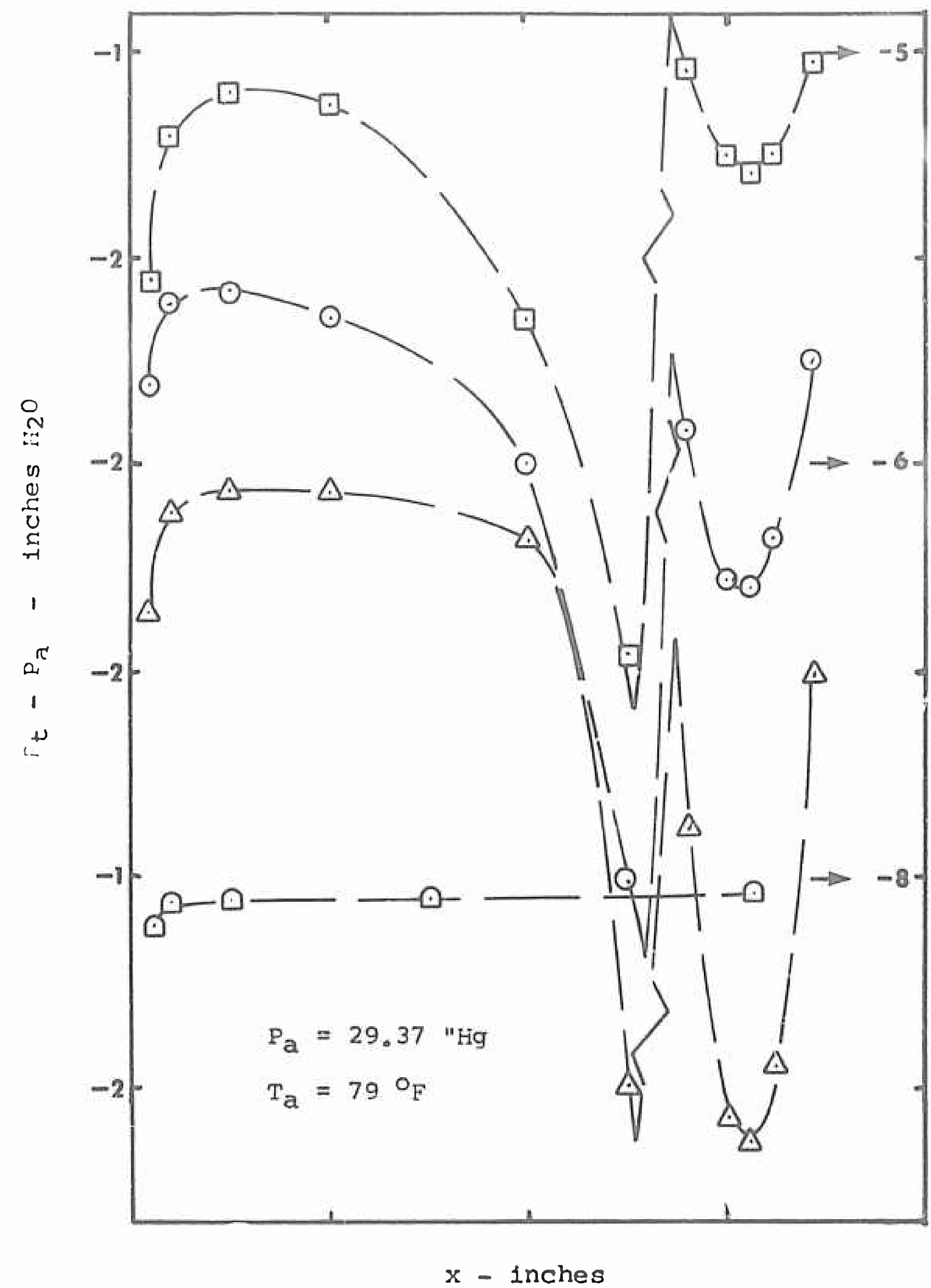

Figure 44
Total Pressure minus Atmospheric Pressure
vs. Distance from Wall

Cyl. C   V = 164.8 fps I^2R/L = 0 Btu/hr inch

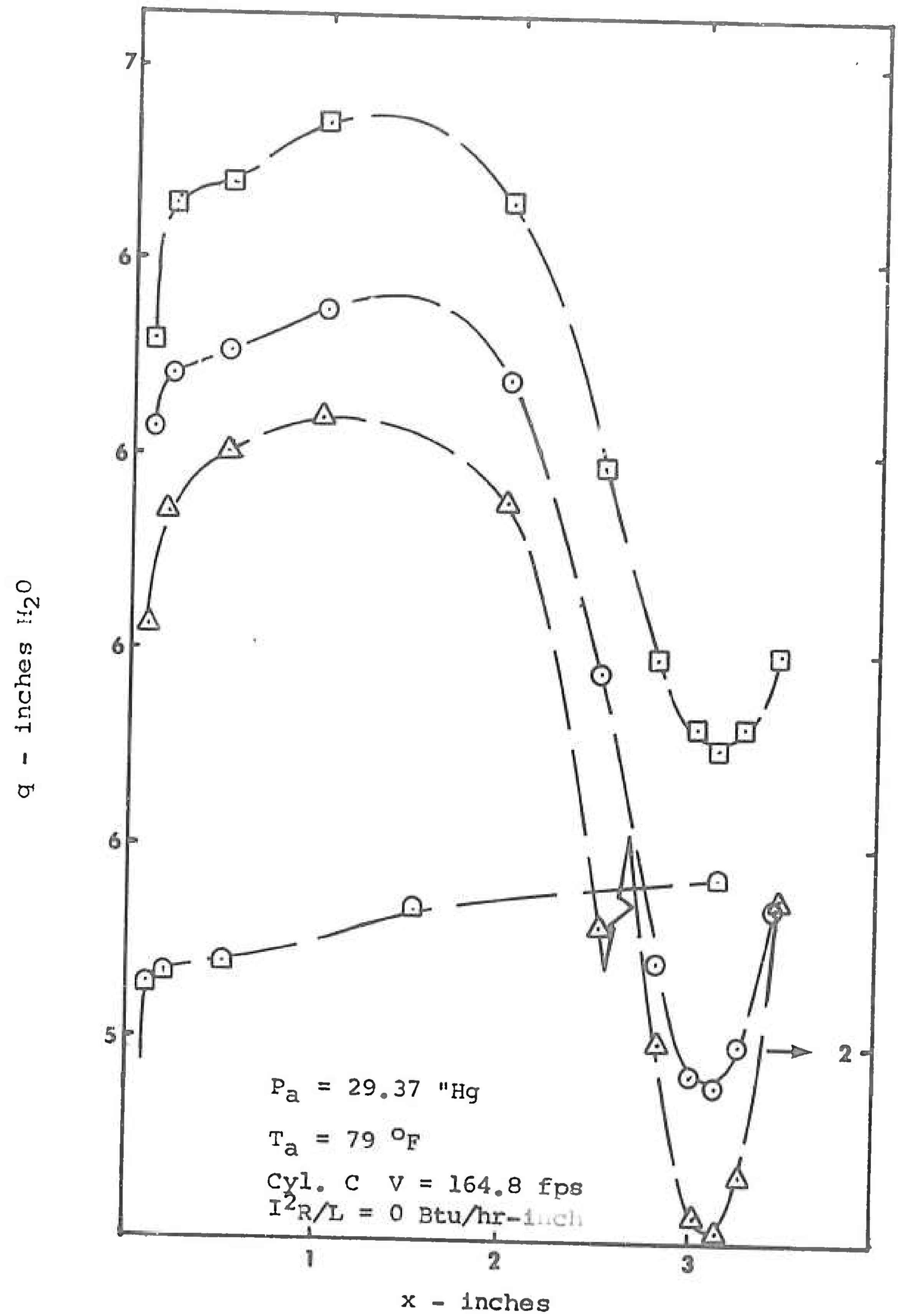

Figure 45
Dynamic Pressure vs. Distance from Wall

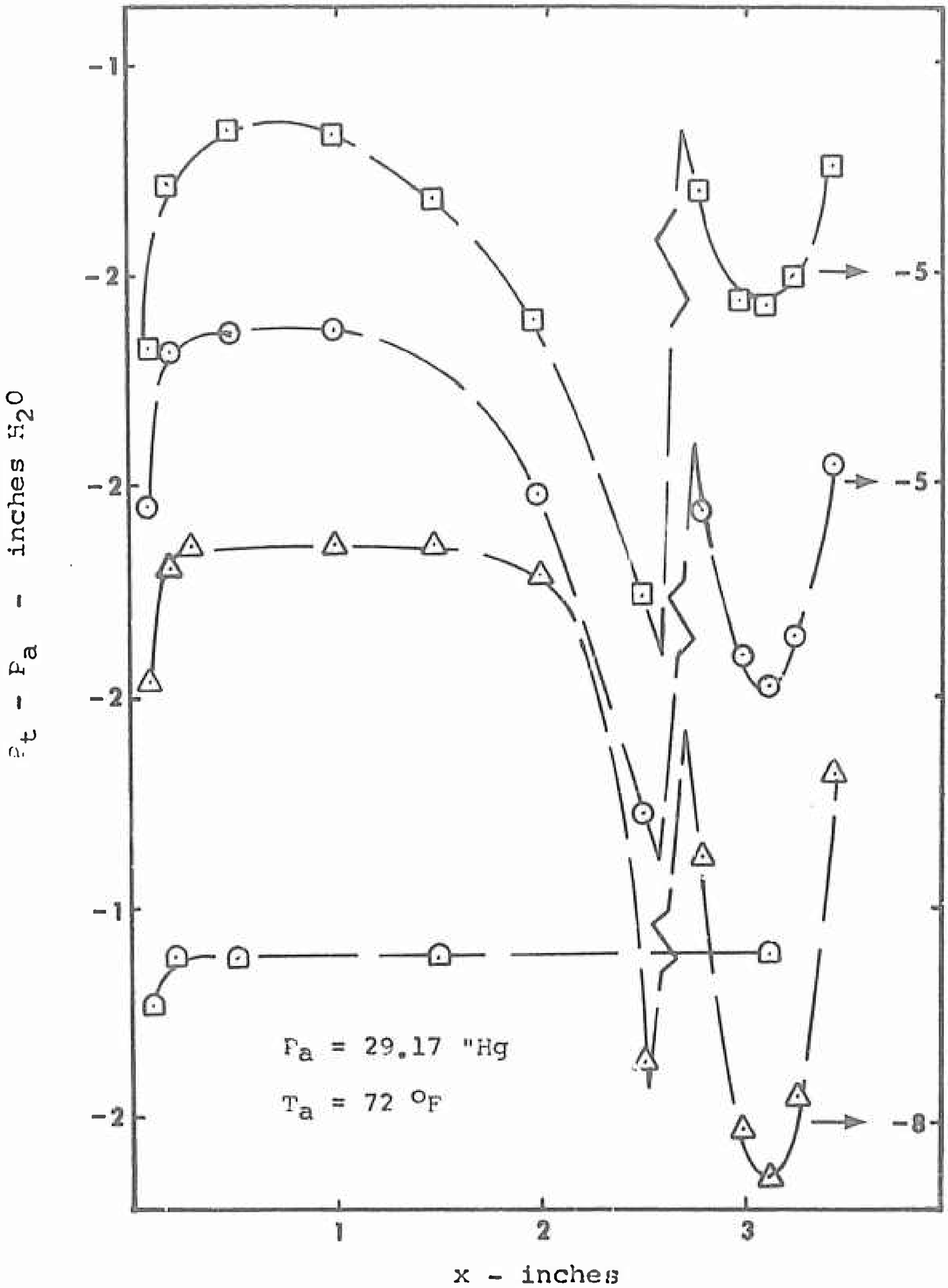

Figure 46
Total Pressure minus Atmospheric Pressure
vs. Distance from Wall

Cyl. C $V = 159.5$ fps $I^2R/L = 256.0$ Btu/hr-inch

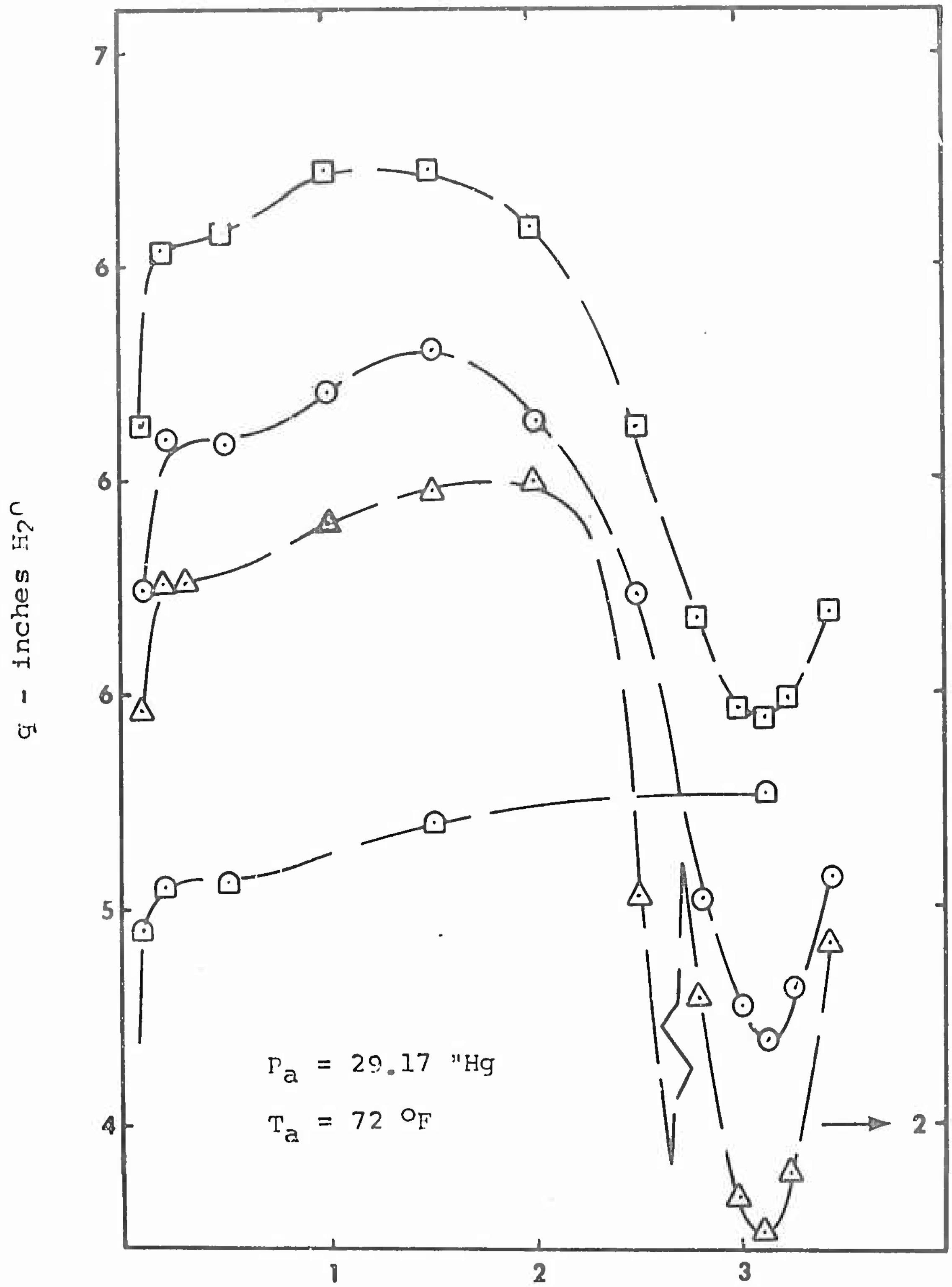

Figure 47

Dynamic Pressure vs. Distance from Wall

Cyl. C V = 159.5 fps I^2R/L = 256.0 Btu/hr-inch

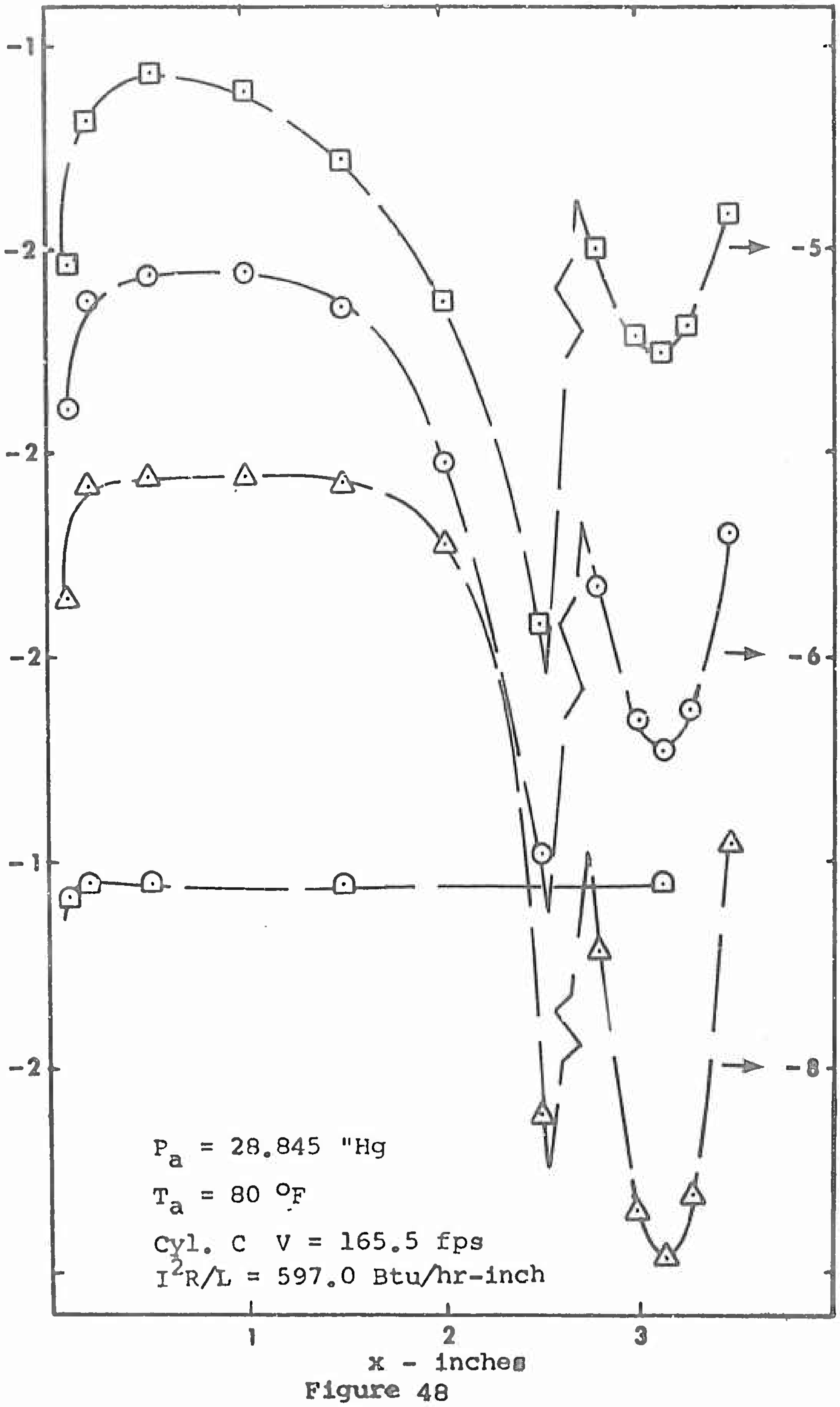

Figure 48
Total Pressure minus Atmospheric Pressure
vs. Distance from Wall

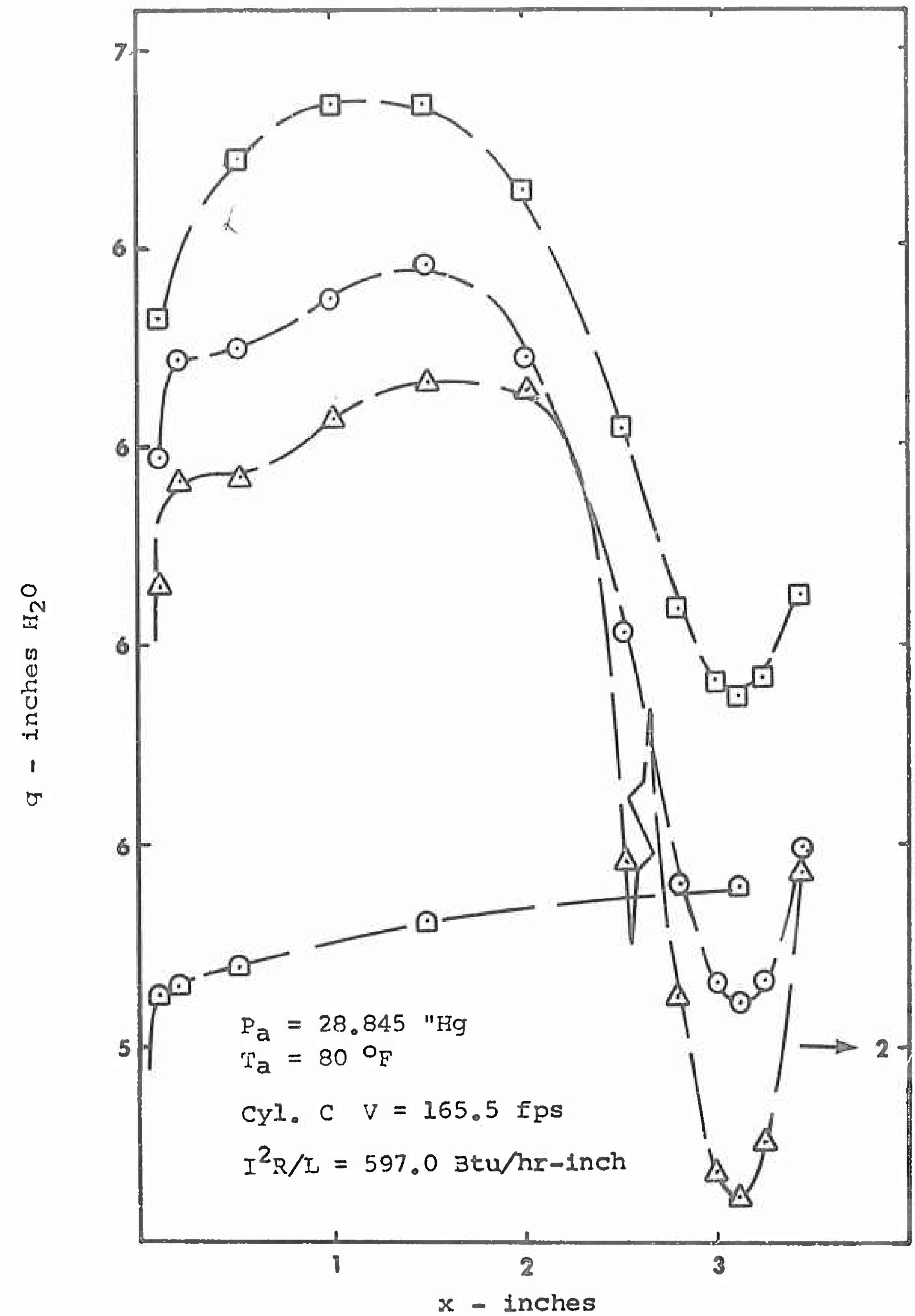

Figure 49

Dynamic Pressure vs. Distance from Wall

Appendix G

Heat Transfer Correlation

The temperature readings from the thermocouples on the cylinder surface were used to evaluate the heat transfer to the airstream by convection and to show typical temperature distributions. Temperatures were recorded on all runs at the two different heating rates, i.e., $I \approx 4.1$ amps and $I \approx 6.15$ amps. The results are presented in Figures G-1, G-2, and G-3, and in Table I.

These results are discussed here as an appendix rather than in the main text, because of the large variations in temperature between the four thermocouples when they were rotated to the same circumferential location. Since the data has obvious variations and is too numerous to check in detail, a random sampling of the temperatures indicated by the thermocouples at the 90, 180, 270, and 360 degree locations (Fig H-12) gave variations from 5% to 13% (based on the average) in thermocouple temperature. The same discrepancies are illustrated by examining Figures G-1 and G-2 for symmetrical temperature readings at points 90 degrees from the forward stagnation point. The temperatures in Figures G-1 and G-2 are the average temperatures of four thermocouples, when rotated to the location designated, except as noted. The discrepancies may be exaggerated at 90-degree points, because the local character of the boundary layer is uncertain. Giedt in-

dicates that either separation or transition from laminar to turbulent flow occurs in the 90-degree region (Ref 12:727).

Other physical causes of error are construction and installation. First, the iron-constantan thermocouples were not annealed, nor were they soldered or welded to the nichrome ribbon. As the cylinder was heated, the contact between the thermocouples and the nichrome may have varied because of thermal expansion.

Second, there was no thermal barrier inserted inside the mica tube to separate the thermocouple lead wires and the bare nichrome ribbon, which exited the top of the cylinder together. Consequently, a lead wire may accept some heat transfer from the heated nichrome ribbon. After exiting the top of the cylinder, the lead wires were connected to a terminal board since they were quite short. A terminal board was used (rather than spot welding) to attach the extension wires to the lead wires, because it was necessary to use a larger diameter wire. The larger diameter wire was used so that the proper external resistance (10 ohms) for the commercial temperature gauges would not be exceeded. The terminal board connections were within six inches of the exit, so the possibility of a thermal gradient across these connections is very likely. This creation of a new junction and electric potential may give an erroneous temperature reading, which may vary for each thermocouple.

Third, the accuracy of the commercial temperature

gauges is only 2% of their full scale (1500°F).

Fourth, location of each thermocouple junction at exactly 90 degrees from the other adjacent two is difficult and some error must be expected.

Fifth, slippage of the cylinder while the turning mechanism was being operated was a constant problem, because of the continual weakening of the mica under prolonged heating (see discussion under Pressure Drag Coefficient).

These errors place some doubt in the accuracy of data. To correct for some of these errors, the calculations were made by disregarding spurious temperature readings, as discussed later under determination of average wall temperature.

Heat transfer data is presented in Figure G-3 as mean Nusselt number versus Reynold's number (both based on cylinder diameter) where properties are evaluated at the arithmetic average temperature of the cylinder surface and free stream. The Nusselt number contains the mean convective heat transfer coefficient, $\bar{h}_c$, between the cylinder wall and the free stream.

To obtain $\bar{h}_c$, the following formulation and assumptions were made. The total power supplied equals the heat losses. This is discussed under Theoretical Considerations as a heat balance. Rewriting the heat balance yields

$$I^2R = \bar{h}_c\ (\pi dL)\ (\bar{T}_{cyl}-T_\infty) + \pi dL\ \epsilon\sigma(\bar{T}_{cyl}^4-T_{tw}^4)+Q_k+Q_{fc}$$

where I is the current, R is the resistance of the nichrome ribbon evaluated at $\bar{T}_{cyl}$, d is the outside diameter of the cylinder, L is the length of the cylinder in the tunnel, $\bar{T}_{cyl}$ is the average cylinder wall temperature, ϵ is the emissivity of the cylinder surface, σ is the Stefan-Boltzmann constant, T_{tw} is the tunnel wall temperature, Q_k is the heat lost by conduction from the cylinder to the tunnel walls, and Q_{fc} is the heat lost by free convection from the interior of the cylinder to the atmosphere.

The resistance, R, at $\bar{T}_{cyl}$ was obtained from (Ref 7). The average cylinder surface temperature, $\bar{T}_{cyl}$, was determined by averaging all temperature readings obtained when the cylinder was rotated in increments through 360 degrees. Not included were those readings that were obviously in error. Temperature readings disregarded included those which indicated room temperature at high heating rates, those which had large discrepancies from the other thermocouples, and those which did not indicate the proper change when velocity or heating rate were changed. The number of readings averaged varied from a minimum of 16 with only one thermocouple operating to as high as 98 with all four thermocouples operating.

Free-stream temperature, T_∞, was assumed equal to atmospheric temperature, T_a, which was measured by the

thermometer on the front face of the hexagonal inlet.

The emissivity, ϵ, used was 0.72 (bright nichrome) for the low heating rate ($I \approx 4.1$ amps) and 0.97 for the high heating rate ($I \approx 6.15$ amps) (Ref 22:475). The oxidized value was used for high heating rates because a visual check showed an oxidized deposit shortly after the start of those tests. The emissivity of mica, which is 0.84 @ 200°F (Ref 43:190), was considered. However, since the surface characteristics of mica changed with prolonged heating (it became whitish after the shellac binding it was boiled off), it was not included in the calculations. The mica exposed between the nichrome ribbon accounted for 18% or less of the total surface area at mid-length of the cylinder; so, if the emissivity of mica remained at 0.84, the error induced by not calculating an average emissity based on area is 3%.

Tunnel wall temperature, T_{tw}, was assumed equal to atmospheric temperature T_a. No thermocouple was installed to measure actual tunnel wall temperature, and, at maximum heating, the tunnel walls were only slightly warm to the touch of the hand.

Heat lost by conduction, Q_k, was assumed negligible because the nichrome ribbon was wound at greater spacing intervals near the tunnel walls (which generates less heat in that area) and the thermal conductivity of mica is approximately 1 Btu/hr-ft-°F in the temperature range encountered (Ref 14:681).

Heat lost by free convection, Q_{fc}, was assumed small and a method for computing free convection losses from the inside of a cylinder in (Ref 20:346) was used to check this assumption. A calculation was made using cylinder C, the highest heating rate, and the lowest velocity. An inside wall temperature of $(\overline{T}_{cyl}/2)$ was used, because the thermal conductivity of mica (perpendicular planes @ 122°F) is 0.25 Btu/hr-ft-°F (Ref 22:450). Calculation showed Q_{fc} to be approximately 7% of the I^2R heating, and indicates the maximum order of magnitude. This free convection analysis neglects the internal wiring and blockage at the bottom of the cylinder, which severely restricts the airflow out of the top of the cylinder, and may further lower the free convection losses.

When Q_k, Q_{fc}, and $Q_{r,fs}$ are considered negligible, and the heat generated per one-inch length of cylinder is considered, the equation becomes

$$I^2R/L = \overline{h}_c(\pi d)\,(\overline{T}_{cyl}-T_\infty) + \pi d\,\epsilon\,\sigma(\overline{T}_{cyl}{}^4-T_\infty{}^4)$$

where T_∞ is used to indicate T_a. After $\overline{h}_c$ was obtained from the equation, $\overline{Nu} = \overline{h}_c D/k_f$ was calculated with k_f evaluated at the film temperature, $T_f = (\overline{T}_{cyl}+T_\infty)/2$.

Likewise, Reynold's number was calculated with properties evaluated at the film temperature. The V used in Reynold's number is the upstream centerline velocity calculated from measurements by the pressure probe, and is not corrected for tunnel blockage.

Results are plotted in Figure D-3, against a correlation curve by Douglas and Churchill (Ref 6:26).

The largest discrepancies in Nusselt number were with cylinder A @$I \approx 6.15$ amperes, i.e., the smallest diameter cylinder and highest heating rate. In this test, only one or two thermocouples were operating properly, so it appears the temperature error may have been large. If the measured temperatures were considered high, the discrepancy may be explained as follows. A higher than actual temperature would result in an erroneously high radiation heat loss correction. A recomputation, using a lower $\overline{T}_{cyl}$, would result in a lower radiation heat loss, and, consequently, a higher convective heat transfer rate, Q_c. A lower $\overline{T}_{cyl}$ would also result in a lower $(\overline{T}_{cyl}-T_\infty)$. Since $\overline{h}_c = (Q_c/A)/(\overline{T}_{cyl}-T_\infty)$, a higher Q_c and lower $(\overline{T}_{cyl}-T_\infty)$ would result in a considerably higher $\overline{h}_c$. The mean Nusselt number would increase significantly, since k_f also decreases with a decrease in $\overline{T}_{cyl}$. The increase in Reynold's number would be slight since (μ_f/ρ_f) is approximately proportional to $T_f^{7/4}(^oR)$, and T_f decreases only one-half of the decrease in $\overline{T}_{cyl}$, if T_∞ remains constant.

Another possible source of temperature error may be caused by the close proximity of the thermocouples to the heated nichrome ribbon. This test situation (smallest cylinder, highest current) was the extreme situation for heat build-up on the inside of the cylinder. The loss of two thermocouples was caused by either excessive heat or

direct contact with the nichrome ribbon. The remaining two thermocouples probably had large thermal gradients at the terminal board connections.

The rest of the data in Figure D-3 falls on or slightly below the reference line of Douglas and Churchill, which is a recorrelation of data collected by Hilpert and other investigators (Ref 6:26). The overall correlation of this data indicates that the approaching free-stream air has the low turbulence level for which the inlet was designed and that the cylinder has low conduction and free convection losses.

Other temperature data obtained are listed in Table I. In this table, $\overline{T}_{cyl}$ is the average of all temperatures recorded for a particular run when the cylinder was rotated through 360 degrees in 10, 15, or 30 degree increments. $\overline{T}_{cyl}^{*}$ is the average of the temperatures in Figures G-1 and G-2 for the run designated, $T_{cyl,min}$ is the minimum temperature recorded by any thermocouple in that run when the cylinder was rotated; $T_{cyl,max}$ is the maximum. Table I reveals that $\overline{T}_{cyl}$ and $\overline{T}_{cyl}^{*}$, agree amazingly close in this Reynold's number range ($2.835 \times 10^3 \leq Re_f \leq 5.24 \times 10^4$). Examination of Figure 9-9 in (Ref 20:410) indicates that the 90-degree points are located near or at the minima and maxima of the Nusselt number and their locations may be coincidental in yielding close to average temperature. The small error between $\overline{T}_{cyl}$ and $\overline{T}_{cyl}^{*}$ indicates that only four thermocouple readings such as those in Figures G-1 and G-2 may

yield the average cylinder temperature. In this study, $\overline{T}^{*}_{cyl}$ was within 2% of $\overline{T}_{cyl}$ on all tests run, except for two tests on cylinder C at $I \approx 6.15$ amps. In these two test (40 and 80 fps) slippage was a major factor, but $\overline{T}^{*}_{cyl}$ was within 2.5% and 5% respectively of $\overline{T}_{cyl}$.

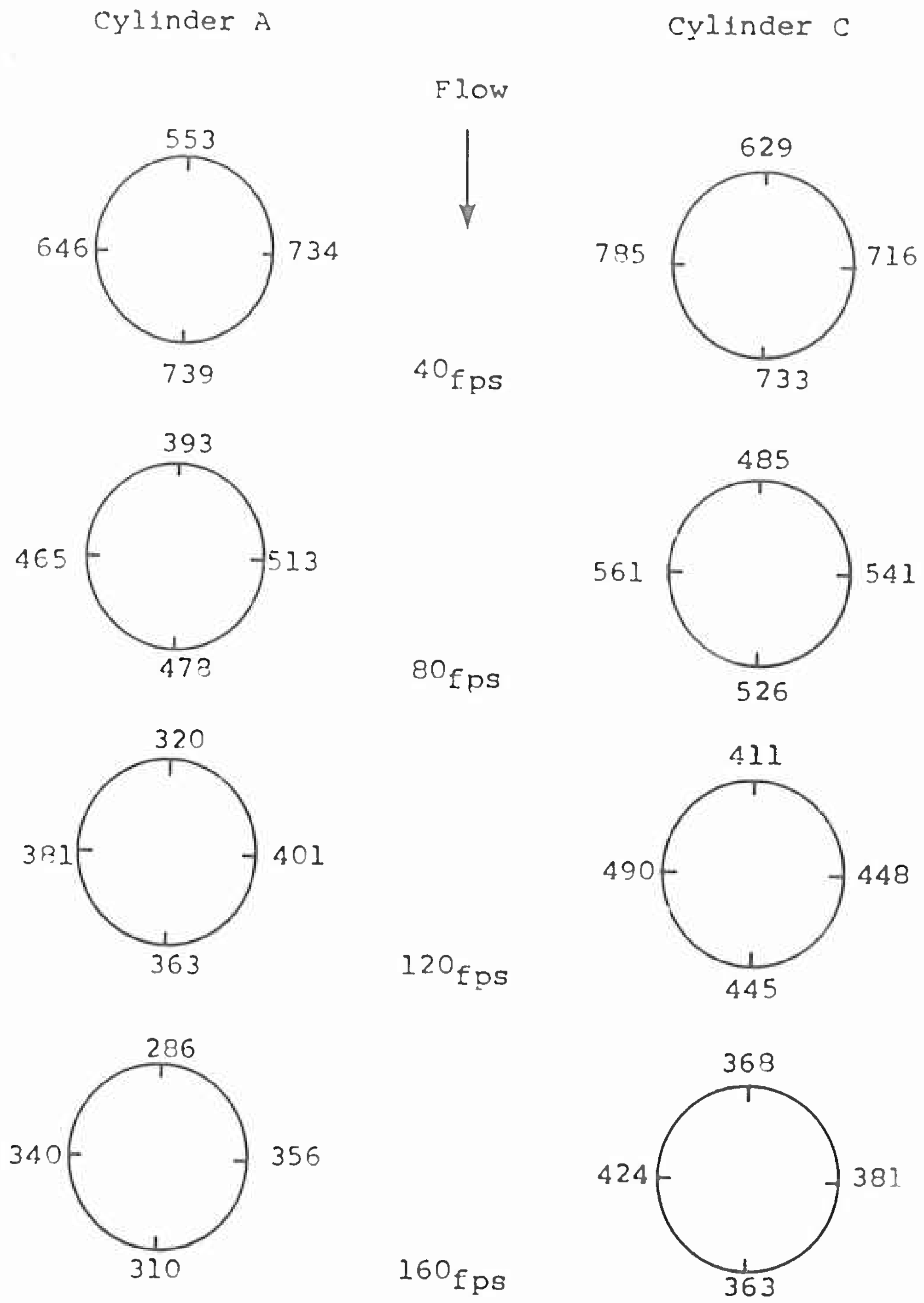

Figure G-1

Cylinder Surface Temperature $-^{o}F$ ($I \approx 4.1$ a.)

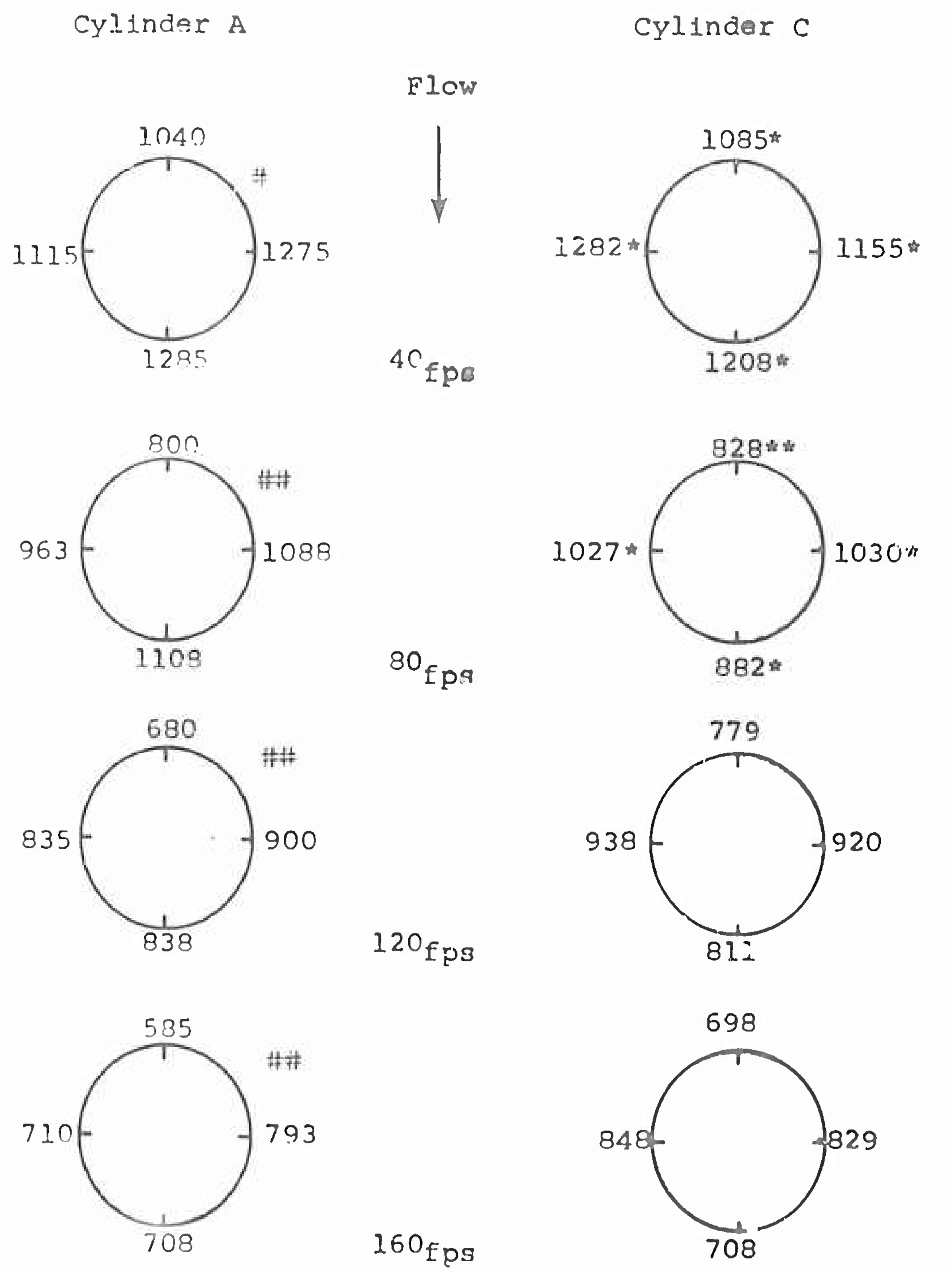

only one thermocouple operating properly
only two thermocouples operating properly

* one thermocouple disregarded as reading too low
** two thermocouple disregarded as reading too low

Figure G-2

Cylinder Surface Temperature - ^{o}F ($I \approx 6.15$ a.)

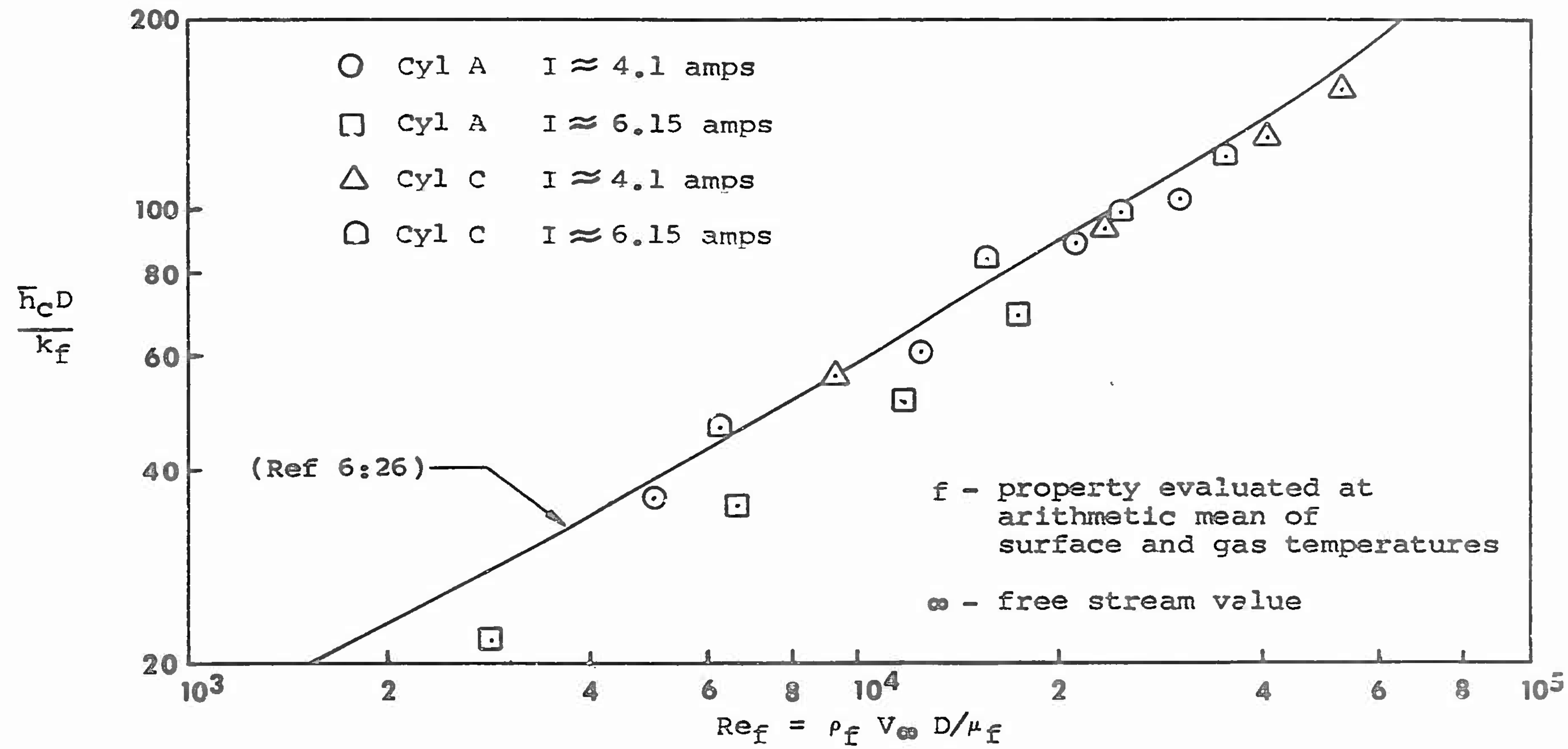

Figure G-3

Mean Nusselt Number vs. Reynold's Number

Table I
Heat Transfer Correlation Data

Cyl.	V fps	I amp.	E volts	$\overline{T}_{cyl}$ °F	$\overline{T}_{cyl}^{*}$ °F	T_{cyl}, min. °F	T_{cyl}, max. °F	Re x104	Re_f x104	$\overline{Nu}_f$
A	40	0	0	-	-	-	-	0.987	-	-
	80	0	0	-	-	-	-	1.974	-	-
	120	0	0	-	-	-	-	2.96	-	-
	160	0	0	-	-	-	-	3.96	-	-
	40	4.1	62	654	668	520	760	0.991	0.5	36.2
	80	4.115	62	465	462	370	540	1.99	1.24	60.6
	120	4.11	61.9	371	366	310	440	3.0	2.105	89.2
	160	4.115	62	324	323	275	380	4.01	3.0	105.2
	40	6.115	94	1154	1179	1000	1345	0.958	0.2835	21.75
	80	6.115	94	982	990	765	1175	1.92	0.664	35.5
	120	6.115	94	819	813	650	980	2.88	1.173	51.0
	160	6.11	94	702	699	560	860	3.82	1.73	68.4
C	40	0	0	-	-	-	-	2.08	-	-
	80	0	0	-	-	-	-	4.0	-	-
	120	0	0	-	-	-	-	6.31	-	-
	160	0	0	-	-	-	-	8.42	-	-
	40	4.09	116.1	716	716	600	820	2.06	0.923	55.85
	80	4.105	117.6	538	528	460	640	4.3	2.32	97.0
	120	4.12	117.15	448	449	380	530	6.5	4.03	130.6
	160	4.10	116.4	387	382	320	460	8.33	5.27	156.0
	40	6.155	182	1147	1159	920	1365	2.015	.619	46.6
	80	6.14	181.5	919	922	750	1090	4.15	1.545	83.55
	120	6.16	182	856	862	740	1000	6.24	2.45	99.1
	160	6.155	182.25	771	771	630	880	8.3	3.54	123.2

Appendix H
Photographs and Sketches of Apparatus

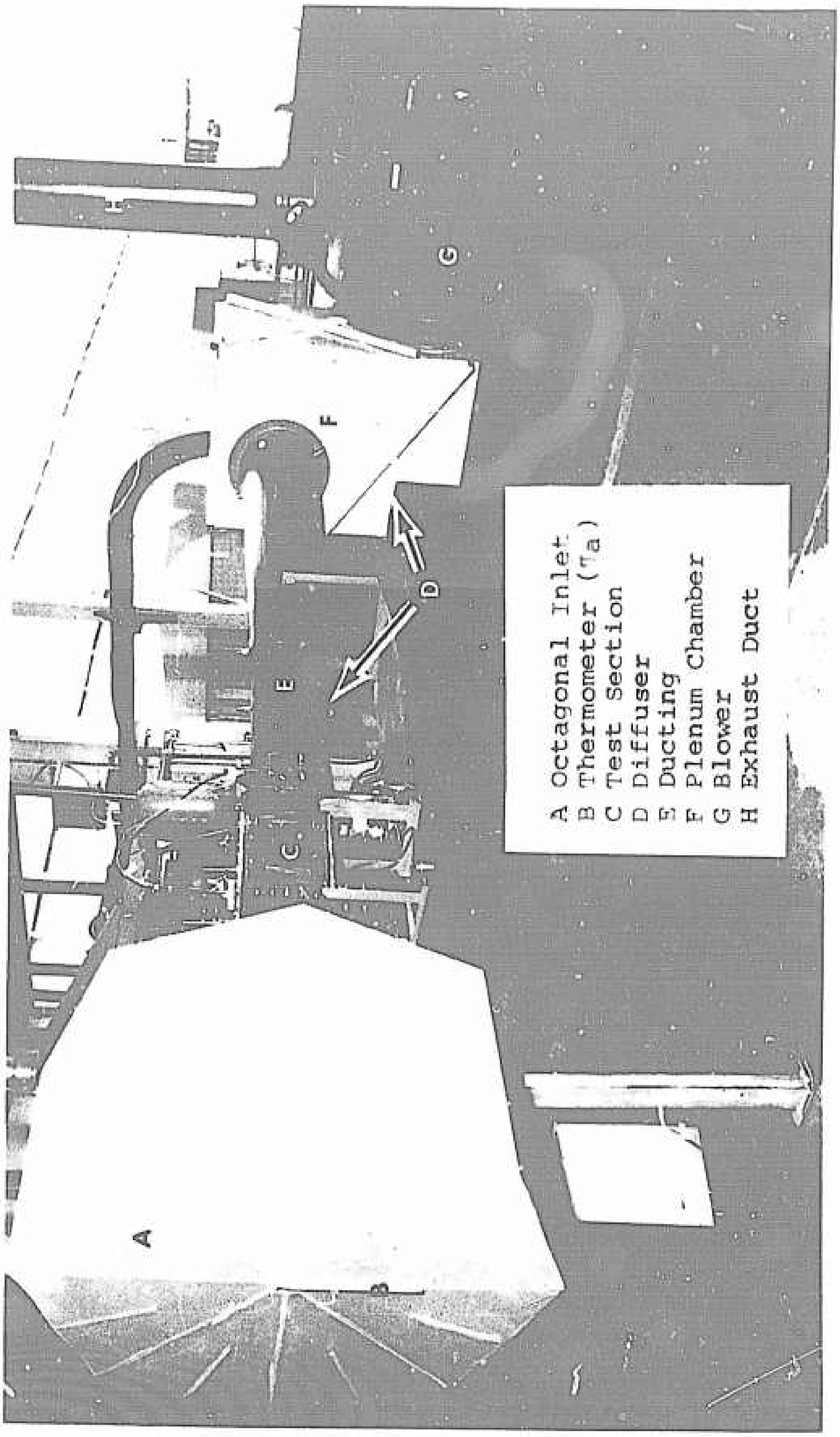

Figure H-1

Complete Wind Tunnel

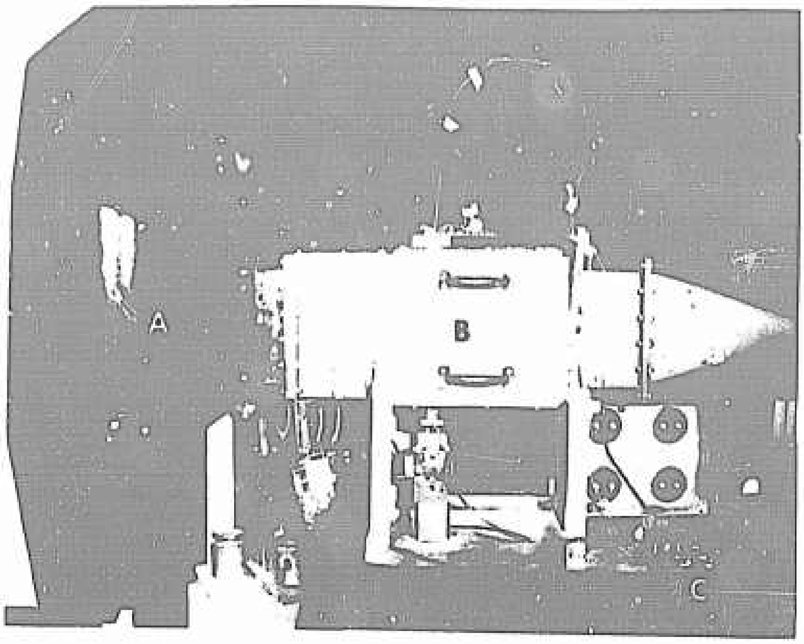

A. Contractor
B. Test Section
C. Power Supply
   Hook-up
D. Wire Cable

Figure H-2
Test Section with Outer Plate and Shield

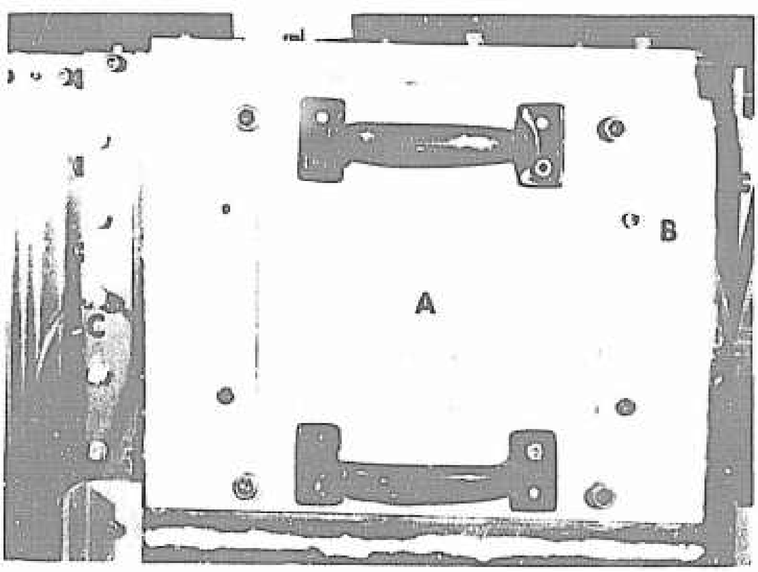

A. Shield
B. Outer Plate
C. Wall Static
   Pressure Tap

Figure H-3
Test Section (Shield Inserted)

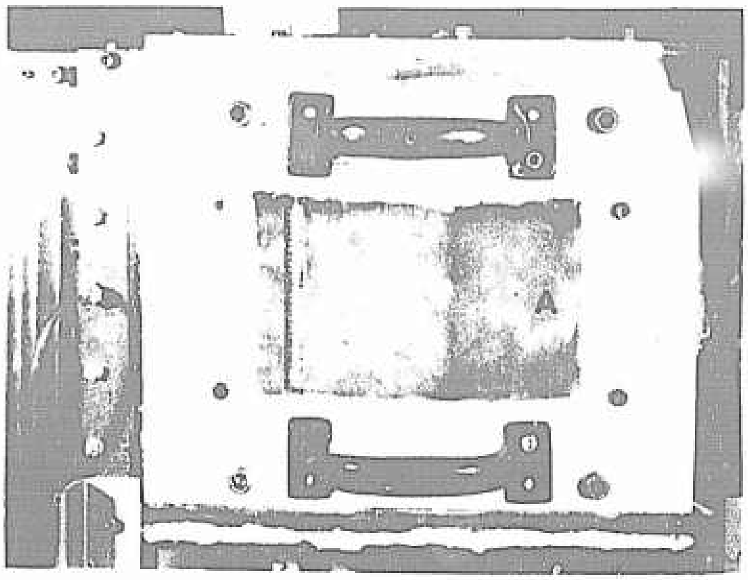

A. Plexiglass
Inner Plate

Figure H-4
Test Section (Shield Removed)

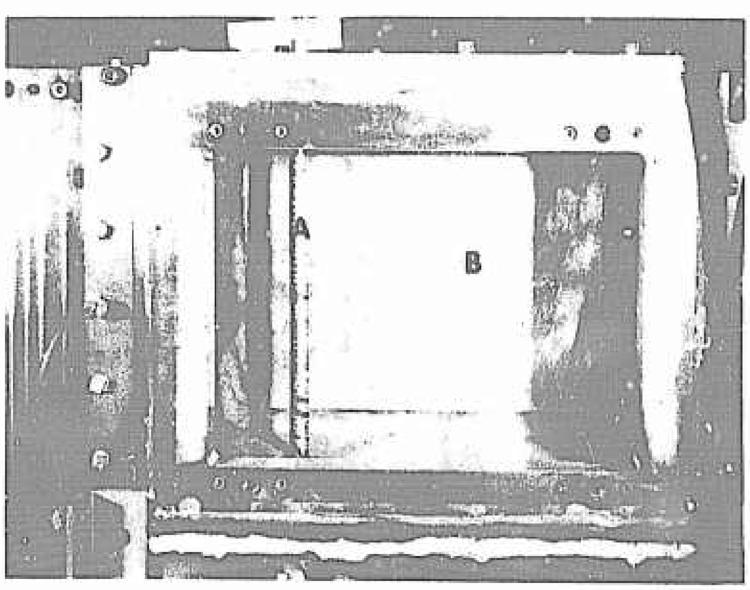

A. Cylinder A
B. Outer Plate
with Probe
Ports

Figure H-5
Test Section (Inner Plate Removed)

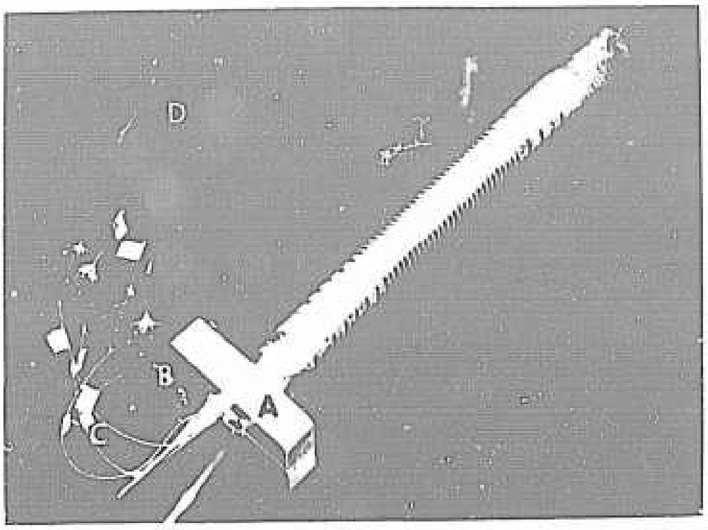

A. Phenolic Block
B. Terminal Board
C. Thermocouple Lead Wires
D. Thermocouple Extension Wires

Figure H-6
Cylinder C

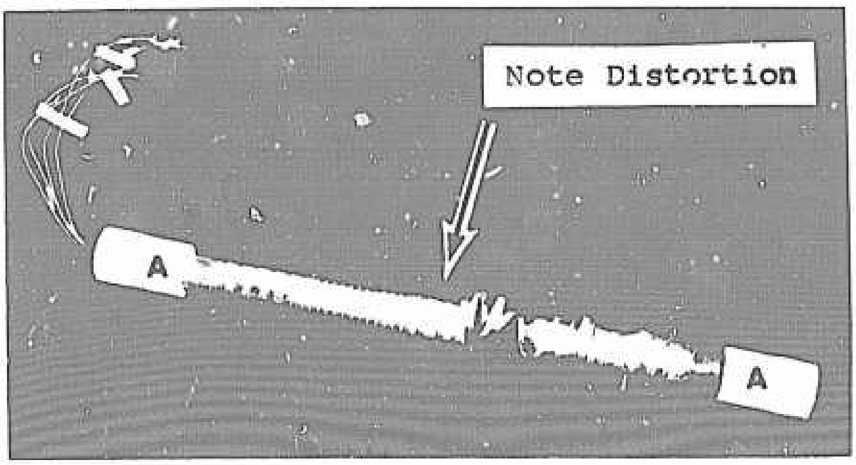

A. Teflon Bushings

Figure H-7
Cylinder B

(Note: Cylinder was broken while removing it from wind tunnel)

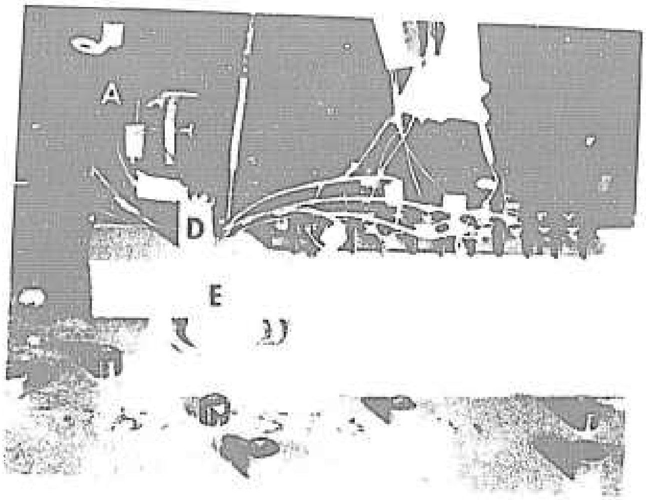

A. Wire Cable
B. Pressure Tube
C. Nichrome Ribbon
D. Copper Blocks
E. Phenolic Block
F. Terminal Board

Figure H-8
Cylinder Mounted in Upper Tunnel Wall

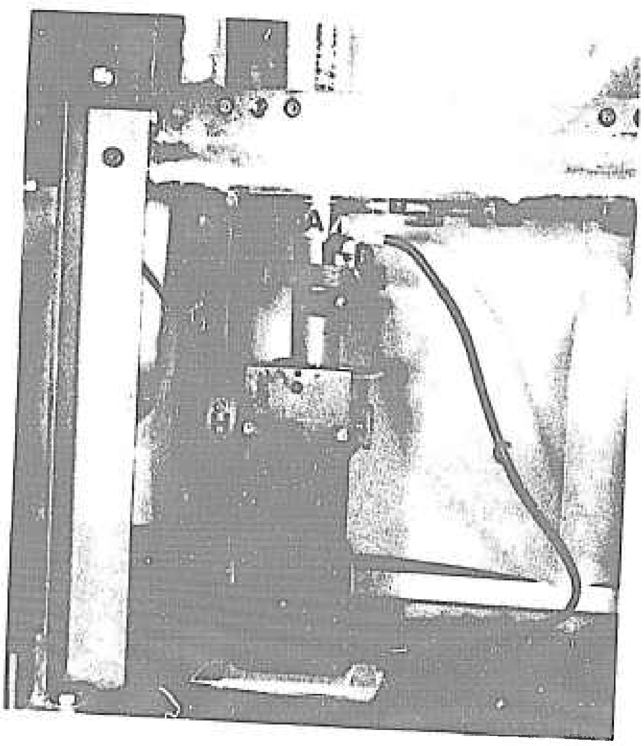

A. Clamp
B. Phenolic Block
C. Wire Cable
D. Copper Blocks
E. Nichrome Ribbon
F. Glass Tubing
G. Compass Scale
H. Crank (to rotate cylinder)

Figure H-9
Cylinder Mounted in Lower Tunnel Wall

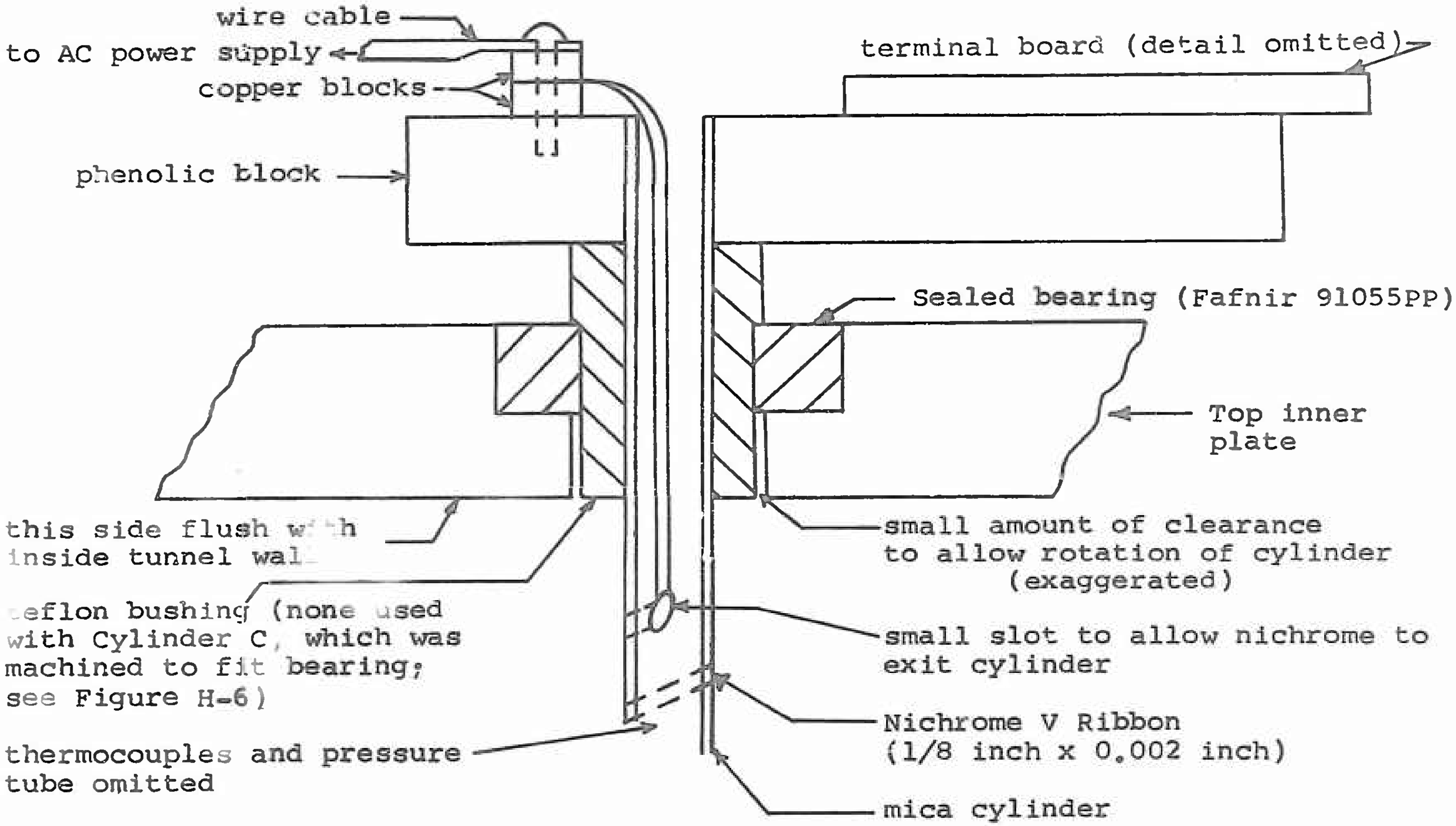

Figure H-10

Cross-Section Sketch of Cylinder Mounted in Upper Tunnel Wall
(see also Figure H-8)

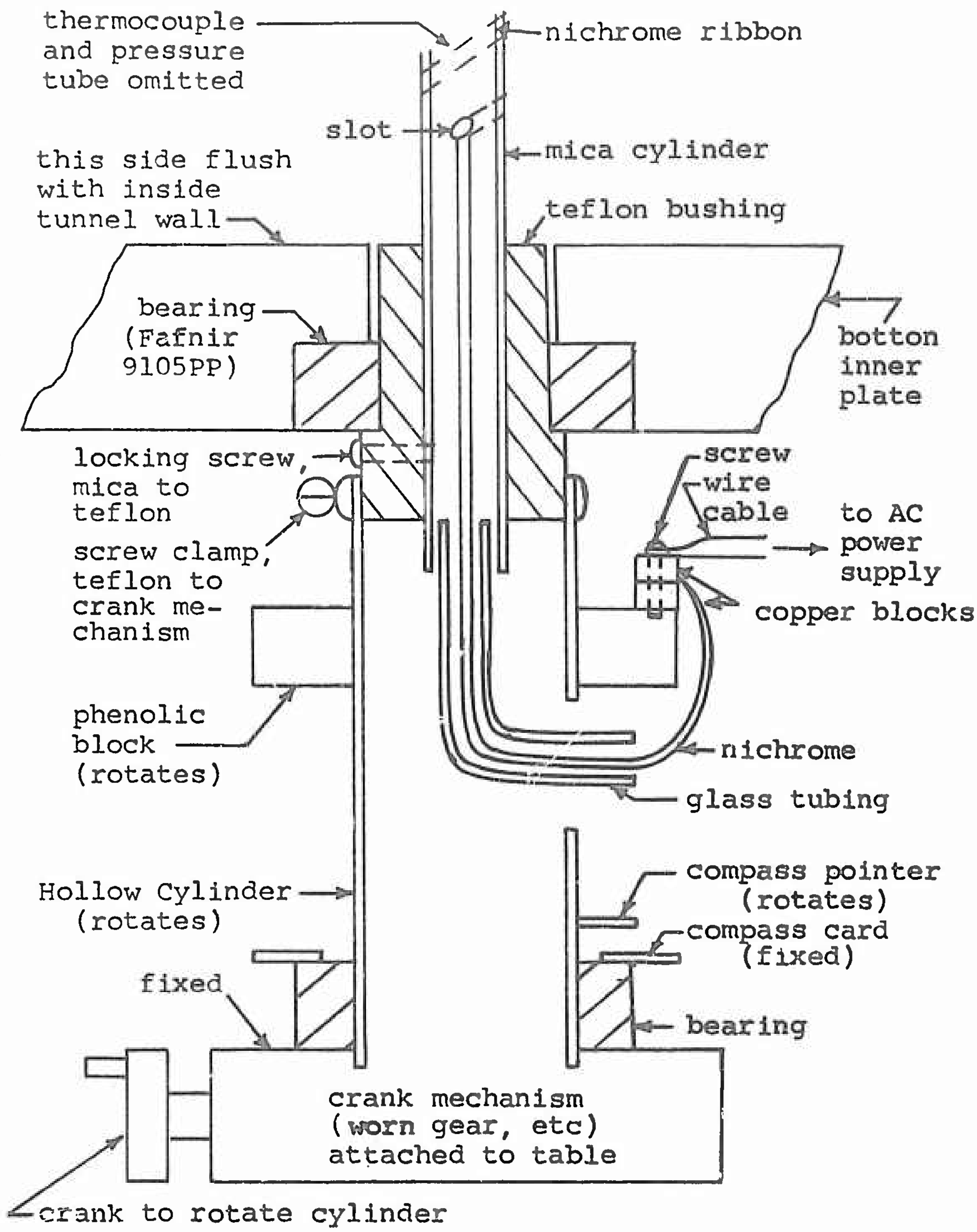

Figure H-11

Sketch of Cross Section of
Cylinder Mounted in Lower Tunnel Wall
(see also Figures H-9 and H-14)

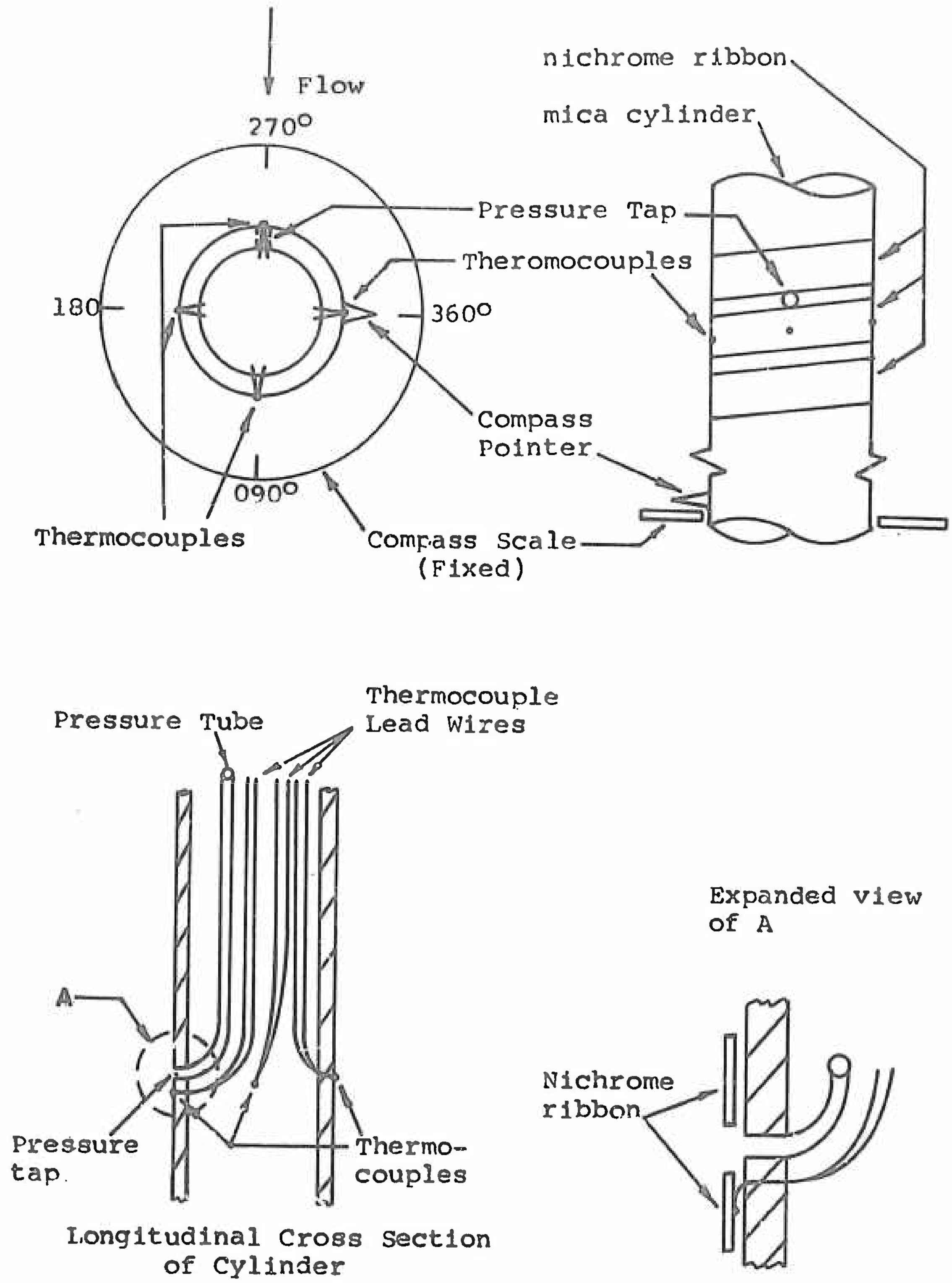

Figure H-12
Sketches of Cylinder Showing
Location of Thermocouples
and Pressure Tap

A Honeywell Strip Chart Recorder
B Ammeter
C Voltmeter
D Thermocouple Switching Junction
E Thermometer
F Cylinder Thermocouple Pyrometers
G Switch for Motorized 220-Volt Rheostat
H 110-Volt Rheostat
I Three-Hole Probe
J Slant Manometer
K Vertical Manometer

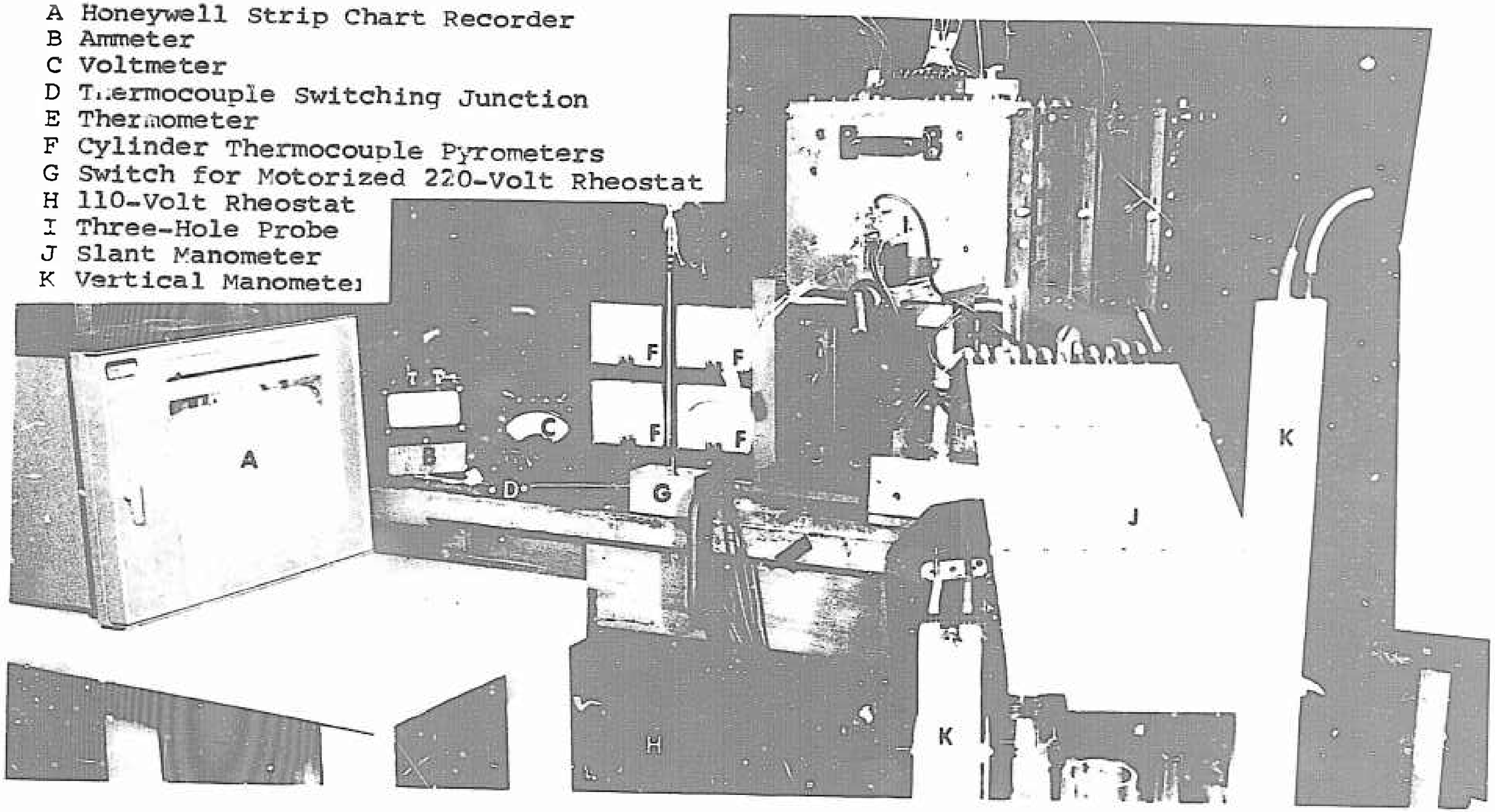

Figure H-13
Instrumentation

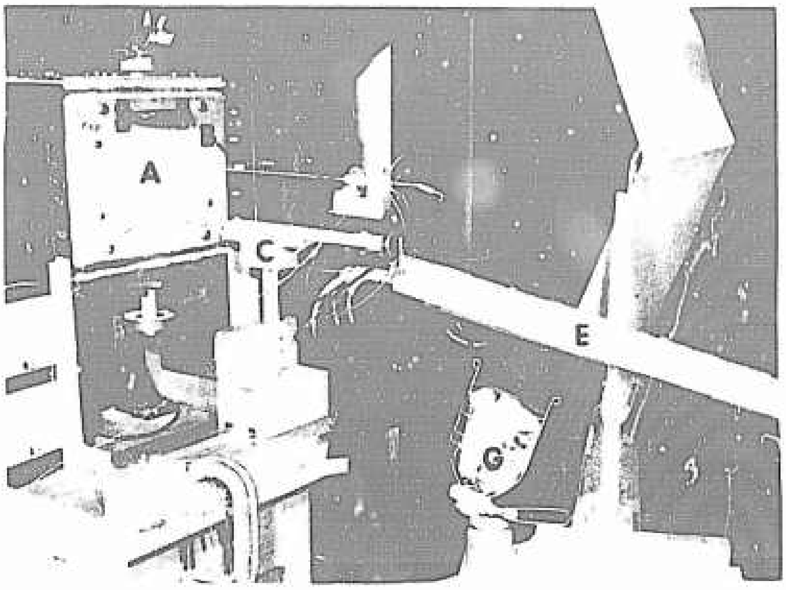

A. Downstream Probe Station
B. Probe Station "C"
C. Traverse Mechanism
D. Three-Hole Probe
E. Slant Manometer
F. Protractor
G. Light

Figure H-14
Three-Hole Probe Mechanism and Slant Manometer

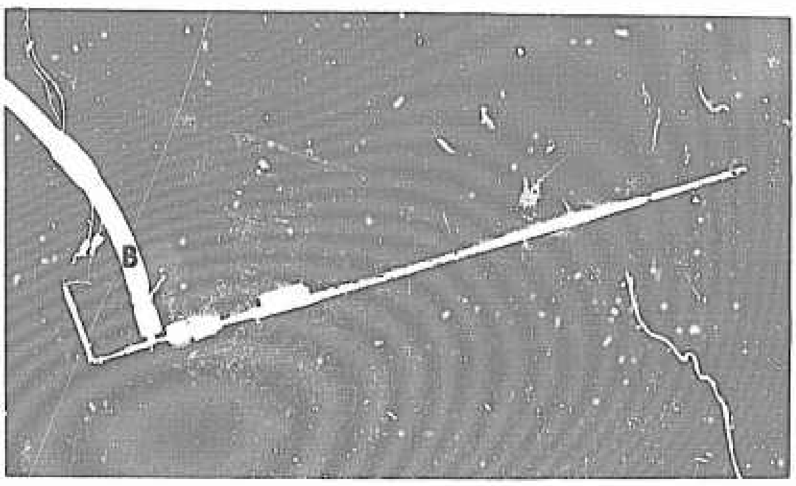

A. Thermocouple Leads
B. Hose (to vacuum pump)
C. Aluminum Foil
D. "O"-Ring Seal
E. Inlet Orifice

Figure H-15
Aspirated Probe

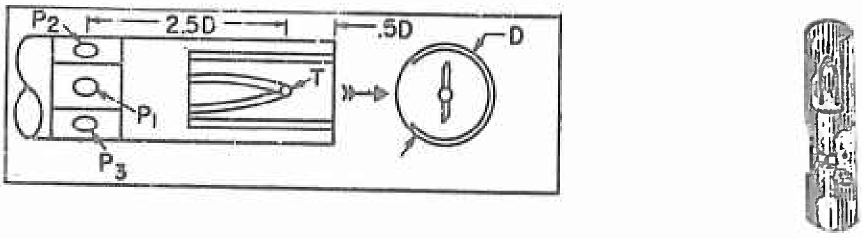

Figure H-16
Sensing Tip of Three-Hole Probe
with Thermocouple (D=0.156")

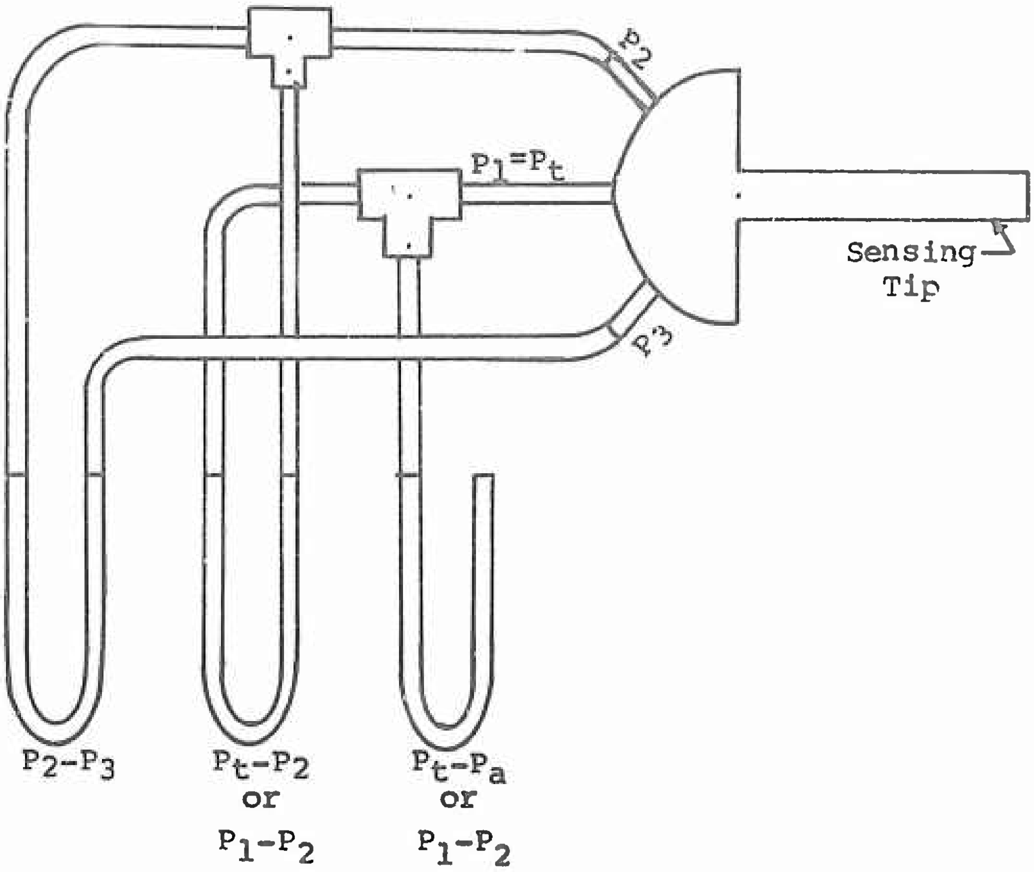

Figure H-17
Sketch of Pressure Tap Hook-Up
for Three-Hole Probe

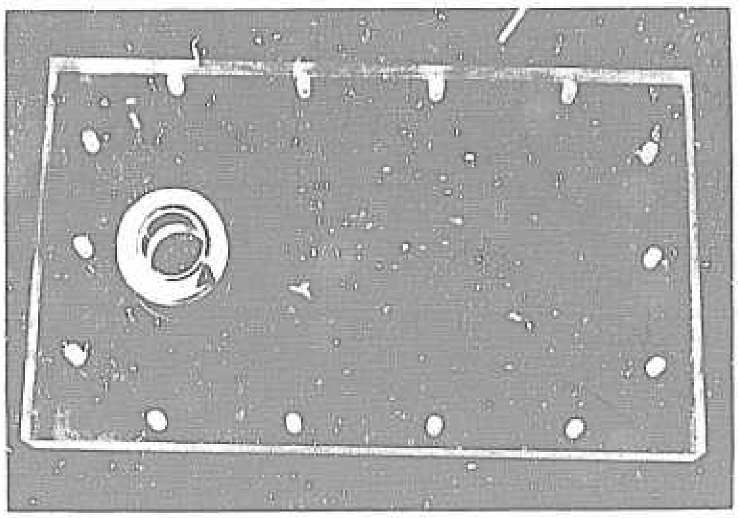

A. Bearing

Figure H-18
Plexiglass Tap Inner Plate
(not used)

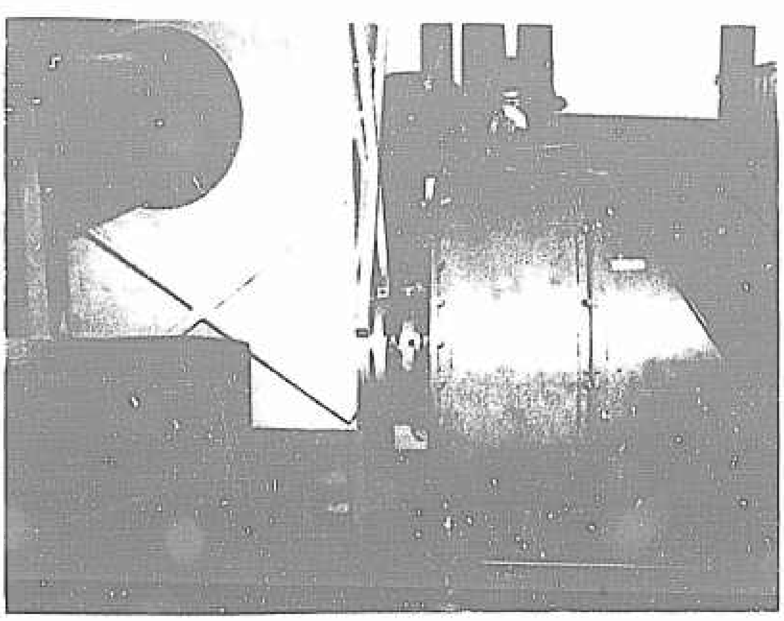

A. Butterfly Valve
B. Adjusting Crank
C. A.C. Motor
D. Connection (Plenum Chamber to Blower)

Figure H-19
Close-up of Diffuser and Blower

Appendix I

Power Supply and Instrumentation

The hook-up of the power supply that delivers current to the nichrome section, and the instrumentation which was used to obtain pressure and temperature data is discussed in this appendix.

The power to heat the nichrome ribbon was regulated by a 110-volt rheostat (Fig H-13). The attachment of the cables to the terminal board, the nichrome ribbon, the ammeter, and the voltmeter are shown in Fig H-2, which is an accepted standard hookup for these items. Later a 220-volt rheostat (not shown) with motorized control was used to regulate the power supplied to the largest cylinder, cylinder C (see Table I for voltage requirements). The length of the cable from the terminal board to the cylinder was adequate to permit a 360-degree rotation of the cylinder.

The thermocouple lead wires in the cylinder exit the cylinder at its upper end and are attached to an offset terminal board because of their short length. The same type wire, but of slightly larger diameter, (diam. = 0.016 inches) was used to connect the terminal board to the direct reading temperature pyrometer and to insure that the 10-ohm external resistance required by the pyrometer would not be exceeded. The temperature pyrometers used were current-type meters manufactured by American Precision Instruments,

Inc. These meters require the current produced by the thermocouple junction in order to indicate thermocouple temperature. Their accuracy is 2% of full scale deflection (1500°F).

The cylinder pressure tap, a stainless steel tube, also exits through the top opening of the cylinder and is connected by rubber tubing to both the slant and vertical manometers (Fig H-13). Clamps were used to block the lines to the slant manometer, when pressure exceeded the limitations of the slant manometer.

The slant manometer (Figs H-13 and H-14) used was modified from one previously used in another experiment. A longer, wider panel for holding seven U-tube manometers was secured to the existing panel. A plastic protractor was attached and a plumb line was strung from the center of the protractor. The slant angle of the panel could then be read directly. Calibration of the slant manometer is discussed in Appendix J.

The three-hole probe has three pressure outlets which are also connected by tubing to the slant manometer (Fig H-13). The chromel-alumel thermocouple leads of the three-hole probe were attached to a thermocouple switching junction (for use in conjunction with the aspirating probe). The leads from the switching junction were directly connected to a Honeywell strip-chart recorder.

Miscellaneous instrumentation included vertical manometers, two thermometers, and a barometric pressure

gauge. The extra vertical manometers were used when pressure difference exceeded the limits of the slant manometer (Fig H-13). One thermometer, located next to the pyrometer, was used to set the pyrometer temperature with thermocouples disconnected (Fig H-13). The other one was located on the front face of the inlet to measure the temperature of the air entering the tunnel (Fig H-1).

Appendix J

Preliminary Testing

As this was the first investigation using the aforementioned tunnel, cylinders, and probe, a large number of preliminary tests were run. These tests were run to check the adequacy of the apparatus and instrumentation, and to gain familiarity with the characteristics of the wind tunnel, probe, and cylinders. Cylinder B was used during the preliminary tests.

First test was the calibration of the slant manometer. The manometer face panel was rotated to a position 75-degrees from the vertical as indicated by the attached protractor. Pressure lines were connected from one side of each manometer tube and from one side of a commercial draft gauge (Meriam Inst. Type G9-6, Serial No. A-434, range: 0-4 inches H_2O) to a common pressure source. The common pressure source was a flexible plastic bottle held in a vise. The bottle was squeezed by the vise to provide pressure. To find the 15-degree slant angle desired for testing, all seven manometer-tube readings were averaged but it was not until the glass tubes were flattened against the plexiglass that the error in each tube was reduced to less than 1% of the commercial gauge. For this error, the indication of the protractor scale attached to the slant manometer was 74-3/4 degrees from the vertical.

The second test was to determine the operational

characteristics of the three-hole probe (Fig H-17). Specifically, the test was to determine what difference between the indicated static pressures, P_2 and P_3, could be tolerated for accurate pressure measurement of the indicated dynamic pressure, (P_1-P_2). Preferably, the probe is rotated until $P_2=P_3$ and then the readings of the other two manometers, (P_1-P_2) and $P_1-P_a)$, are recorded. The manufacturer indicates that $P_2 = P_3$ is not a necessity for accurate measurement and that pressure measurements taken at a yaw angle of ± 3 degrees, i.e., $P_2 \neq P_3$, will be within 1% of those measurements taken with $P_2 = P_3$ (Ref 40). Tests in this wind tunnel showed that the difference, P_2-P_3, could be as much as ± 0.2 inches indicated on the 15-degree slant manometer (approx. $\pm .05$ inches H_2O actual pressure) for negligible error in other pressure measurements. To compensate for $P_2 \neq P_3$, the following formula, suggested by the manufacturer, was used:

$$(P_1-P_2)_{P_2=P_3} = (P_1-P_2)_{measured} + \frac{(P_2-P_3)measured}{2}$$

where the subscript, $P_2=P_3$, will be dropped, and (P_1-P_2) will be the corrected value at $P_2=P_3$. From the calibration chart (Fig C-1), with $\theta = 0$, and Mach number < 0.15, the value of the ratio:

$$\frac{P_2 - P_s}{P_t - P_s} = 0.073 \text{ (extrapolated)}$$

is read where P_t effectively equals P_1. After algebraic manipulation and use of

$$P_t = P_s + (1/2)\,\rho V^2 = P_s + q$$

the result is

$$q = \frac{P_1 - P_2}{1-0.073} = \frac{P_1 - P_2}{0.927}$$

If the bottom graph on the calibration chart is referred to, it is easily seen than a small change in Mach number has little effect on the value of the ratio, $(P_2-P_s)/(P_t-P_s)$, and on the last equation.

Total pressure is obtained directly from the manometer, (P_t-P_a), where P_t is total pressure and P_a is atmospheric pressure outside the tunnel. Actually, this manometer indicates P_1-P_a, but P_1 effectively equals P_t (calibration not shown; $(P_1-P_a)/q \leq .005$) so that (P_1-P_a) effectively equals (P_t-P_a).

For the purposes of calculation, the pitch angle, θ, was assumed zero. While this may certainly be valid upstream, the flow may turn into the wake behind the cylinder, and θ may be different from zero. If the ratio, $(P_2-P_s)/(P_t-P_s)$, is assumed to vary in the same proportion with Mach number for $\theta \neq 0$ as the ratio does for $\theta = 0$ (Fig C-1), the maximum error in computing q is approximately 3%.

The third check was a comparison of upstream static wall pressure from a tap previously drilled (Fig H-3)

against static pressure calculated from the three-hole probe measurements. With the probe at the centerline of the tunnel a typical difference between the two static pressures was 0.06 inches H_2O. A removable pressure tap was made in an attempt to check static pressure downstream. This removable tap could be inserted at any downstream probe station. However, the static pressure between probe and this wall tap did not agree as well as it did upstream. This was due to the variation in thickness of the tunnel wall and, consequently, the impossibility of maching a single tap which would be flush with the tunnel wall at all downstream probe stations. If the tap is not flush with the tunnel wall, a considerable error in static pressure may result because of secondary flow about the tap (Ref 2:59). Also, since the static pressure in the wake behind the cylinder changes laterally, no accurate check could be made with the three-hole probe. To avoid collection of doubtful data, use of the pressure tap was discontinued.

The fourth check was a check on symmetry of flow on either side of the vertical centerline of the tunnel. Upstream of the cylinder, total variation of total pressure across the tunnel, with the probe 0.1 inch or more from the tunnel wall, was approximately 0.01 inches H_2O for a dynamic pressure equal to 3.20 inches H_2O. Total variation in dynamic pressure was greater because of the effect of depth of immersion. This is discussed under Probe Errors. Variation in dynamic pressure across the tunnel, when at

least 0.5 inches from the tunnel wall, was 0.18 inches H_2O. Variation was less than 0.09 inches H_2O when the probe was immersed half the tunnel width or less. Downstream variations in total and dynamic pressures were almost identical to those measured upstream.

While conducting these tests, four phenomena were noticed, namely, a reverse flow area behind the cylinder, fluctuations in the flow, a long time constant of the three-hole probe, and the appearance of fluid bubbles on the cylinder. Probing at the first probe station downstream of the cylinder resulted in a negative indicated dynamic pressure. At first this was accepted, but for later tests it was decided to conduct all probing outside of the reverse flow region of the wake. Some fluctuations also occurred downstream of the cylinder, when close to the cylinder and inside the wake. Observed fluctuations were ± 0.01 to $\pm .02$ inches H_2O. Upstream of the cylinder no fluctuations were observed.

While tests were being conducted with zero current through the nichrome ribbon, it became evident that the probe had a long time constant, usually one or two minutes and up to five minutes for the larger pressure changes. Two reasons for this long time constant were: 1) the small size of the probe orifices (approx. 0.020 inch diameter), and 2) the long length of tubing from the probe to manometer. The length of tubing was reduced to the minimum possible length, and this did result in some im-

provement. Because of the long time constant it was decided to probe only one-half of the tunnel and to limit the number of probe stations and data points, but to retain enough to define the pressure curves across the tunnel. This required 12 points per probe station. This indicates that at least one-half hour is required to traverse one probe station. Measurements at four probe stations plus cylinder surface temperature and pressure measurements, require about three hours. Since four upstream velocities were used, total run time, including warmup and stabilization, exceeded twelve hours for a particular cylinder at a particular heating rate, provided no other difficulties, such as slippage, were encountered. The effect of this long run time is discussed under Pressure Drag Coefficient.

When the cylinder was first heated, dark bubbles of fluid appeared on the circumference of the cylinder between the nichrome ribbon. The fluid was thought to be the shellac that was used to bind the layers of mica together. Evidently, the heat was forcing the fluid to the surface, where the airstream eventually swept it away.

In addition to these tests, the amount of current that the nichrome ribbon could accept without failing was required. Preliminary burnout tests were conducted by forcing current through six-inch horizontal strips cooled only by free convection. Burnout current was 12 to 17 amperes. Cylinder B was used to determine burnout under actual tunnel conditions. A current of 4.1 amperes re-

sulted in smoke emanating from the interior of cylinder B (probably burning shellac) and in shellac bubbles on its circumference. Both the smoke and bubbles gradually disappeared during testing. Testing was accomplished at 40, 80, 120 and 160 fps. Measurements were taken with the three hole probe at four probe stations (one upstream and three downstream). After completion of these tests, current was gradually increased until at eight amperes (approximately half that of burnout in strip tests) the nichrome ribbon failed at the upper slot where the nichrome was bent to enter the interior of the cylinder.

Appendix K

Probe Errors

Two known errors of the three-hole probe are: 1) the interference and calibration error of the probe, and 2) the total pressure error in a strong total pressure gradient (Ref 40).

Introduction of the probe into the tunnel interferes with the free-stream flow. This effect is compensated for by calibration of the probe. This three-hole probe was calibrated by the manufacturer at a 1.5-inch immersion in a 3-inch passage to agree with wall static pressure at the same cross section. It can be shown using continuity of flow and Bernoulli's equation that as probe immersion depth increases, the velocity at the probe sensing orifice increases, and static pressure decreases. At this 1.5-inch immersion, the probe is calibrated according to the formula:

$$\frac{P_2 - P_s}{P_t - P_s} = c$$

where $P_2 = P_3$ and is indicated static pressure; P_s is actual static pressure, P_t is total pressure, and c is a calibration constant which depends on local Mach number and pitch angle. Solving the equation for P_s yields

$$P_s = \frac{P_2 - cP_t}{1-c}$$

To show the error in P_s which results from the use of this

probe, it is necessary to consider a hypothetical situation. Consider a wind tunnel of constant rectangular cross sectional area with no obstructions and with a fully developed turbulent velocity profile. Assume that P_t is constant across the tunnel outside the boundary layer and that the probe is calibrated at the centerline by use of the previously given formula. Insert the probe to the tunnel centerline and calculate P_s. Now decrease the immersion of the probe in the tunnel. Since the indicated static pressure (P_2) must now increase according to continuity requirements and Bernoulli's equation, P_s calculated by the calibration equation will be higher than true P_s. This erroneously high P_s causes an equally erroneous low dynamic pressure. The magnitude of this error is given by the manufacturer as 5% from mean static pressure for a probe diameter of 0.120 inches with the greatest variation within 10 probe diameters of the wall. The probe used in this investigation was a 0.156-inch-diameter probe, so the error would be slightly larger. Examination of the dynamic pressure curves obtained in this investigation reveal that the higher velocity curves are depressed within 10 probe diameters (1.56 inches) of the wall. Part of this variation may also be the normal profile, one of which is drawn by Schlichting (Ref 30:617). No method of correction was given by the manufacturer, so actual error would be difficult to estimate.

The second error is caused by strong total pressure

gradients, such as near walls or in the wake of the flow behind a body. The probe reads a higher total pressure at these positions, because the flow turns toward the lower pressure side of the probe before it enters the probe. The actual total pressure at this probe position is less than the measured total pressure. Consequently, the total pressure curve of the wake is wider and the total pressure curve near the wall is also decreased. The manufacturer states that in practical use the maximum shift of the total pressure curve toward the higher pressure is practically constant and equals 0.53 probe diameters (Ref 40). This correction was not applied to the total pressure curves in this investigation, because the manufacturer gave no other guide for applying the correction.

Appendix L

Wind Tunnel Boundary Corrections

Wind tunnel boundary corrections considered in this investigation were buoyancy, solid blocking, and wake blocking (Refs 25, 29, and 30).

The buoyancy correction is the normal drop in static pressure along the wind tunnel axis. The maximum bouyancy correction computed was -0.0375 inches H_2O per inch by use of the first equation on page 274 of (Ref 29) with K=0.40 and q=5.85 inches H_2O (corresponds approximately to 160 fps). Pankhurst states the buoyancy effects on drag calculations is usually very small (Ref 5:347). This correction was ignored, since no tests were run to check it and relative results were primarily considered in this study.

Solid and wake blocking were considered together. Various formulas in (Refs 25, 29, and 30) gave values from .0052 to .05 for $\beta = \frac{\Delta V}{V}$ where β is blockage correction, ΔV is the velocity to be added to upstream measured velocity, and V is measured upstream velocity. The formula mentioned by all three references in various forms is

$$\beta = \frac{1}{4} \frac{(\text{cross-sectional area of model})}{(\text{cross-sectional area of tunnel})}$$

(Ref 25:334;29:291;30:56). This results in β = .02 for cylinder A and β = .04 for cylinder C. These corrections were not applied, except to correct the pressure drag

coefficient, because the author decided they would confuse the findings of this study. Since the last two corrections are constant for a given cylinder and velocity, the corrections do not influence relative findings.

Appendix M

Wind Tunnel Components

The inlet, test section, diffuser, and blower are discussed in this appendix.

The inlet consists of a specially designed octagonal chamber attached to a rectangular contraction section of ducting (Fig D-1). The air first flows through ordinary nylon parachute cloth which is attached to the eight sides of the chamber and the front face. After entering the chamber, the air passes through a rectangular opening in the back face into a rectangular contracting inlet, which converges to the cross-sectional area of the test section. The area ratio of the nylon parachute cloth to the rectangular opening in the back face is 8.5 to 1. The area ratio (contraction ratio) of the rectangular opening to the final cross sectional area of the test section is 10:1.

The construction of the octagonal chamber is shown in Figures D-1, D-2, and D-3. In the octagonal chamber, there are eight large vanes and eight small vanes. All the vanes are attached to a one-inch thick plywood board (the back face) which is rigidly attached to the rectangular bellmouth of the original inlet. The large vanes are also attached to the center body. The principles underlying the design can be found in Appendix D.

After passing through the inlet the air immediately enters the test section (Fig H-2). The test section has a

constant cross section of 6-1/4 inches horizontally and 8-3/8 inches vertically. It is 24 inches long, and is made primarily of machined aluminum.

Access to the test section is achieved by removal of the inner and outer plates (Fig H-5). The inner plate is 1-1/8 inches thick and fits flush with the inner and outer surfaces of the permanent wall. The outer plate secures the inner plate to the permanent tunnel wall to assure a flush fit. The inner plate which faces the instrumentation has a series of 0.156 inch diameter holes drilled in it to allow entry of a pressure probe (Fig H-13). Three other probe stations are located upstream. On the opposite side of the tunnel, both an aluminum plate and a plexiglass plate were fabricated for use as inner plates.

The top and bottom inner plates are machined to permit insertion of the test cylinders and a sealed bearing (Figs H-8,h-9,H-10, and H-11). The sealed bearing allows the cylinder to be rotated and prevents air leakage into the tunnel, since the tunnel pressure is slightly less than atmospheric.

The diffuser consists of a 100 inch length of ducting and a box-like plenum chamber, to which the ducting is attached (Fig H-1). The ducting changes from a rectangular cross-section to a circular cross-section in the first twelve inches and then diverges slightly in the remaining length. This ducting enters a vertical face of the plenum chamber. The plenum chamber is constructed of

welded sheet steel. It is strengthened by x-bracing on each face to prevent collapse. The plenum chamber functions as an air reservoir to dampen out pulsations made by the blower. The exit from the diffuser is located on a vertical face and at the same height as the entrance to the blower.

The blower is a drum-like centrifugal air pump operated by a direct drive AC motor, rated at 40 horsepower and 3540 rpm (Fig H-1). The blower is 4 feet in diameter, and is connected directly to the plenum chamber. Directly above the blower is the exhaust duct and a butterfly control valve, which is adjusted by an externally attached crank mechanism (Fig H-19). The exhaust duct extends vertically up from the blower for approximately 25 feet, and then discharges to the outside atmosphere.

Vita

Jerome R. Jarcy was born [redacted] the son of [redacted] His family moved [redacted] in his early childhood and it was there that he was graduated from [redacted] in 1954. In 1959 he received the degree of Bachelor of Science in Mechanical Engineering from Loyola University of Los Angeles. He was commissioned as a Second Lieutenant in the United States Air Force and entered active duty in April 1959. Prior to attending the Air Force Institute of Technology, he was assigned to the Air Training Command where he was an instructor pilot.

Captain Jarcy is married to [redacted] and they have [redacted]

Permanent address: [redacted]

PII Redacted

PII Redacted

This thesis was typed by Mrs. Edith Wik. Graphs and sketches were drawn by Mr. Donald Wik.

UNCLASSIFIED

Security Classification

DOCUMENT CONTROL DATA - R & D

(Security classification of title, body of abstract and indexing annotation must be entered when the overall report is classified)

1. ORIGINATING ACTIVITY (Corporate author) Air Force Institute of Technology (AFIT-SE) Wright-Patterson AFB, Ohio 45433	2a. REPORT SECURITY CLASSIFICATION UNCLASSIFIED 2b. GROUP

3. REPORT TITLE
FLOW FIELD, DRAG, AND HEAT TRANSFER OF A HEATED CYLINDER IN A SUBSONIC CROSSFLOW OF AIR

4. DESCRIPTIVE NOTES (Type of report and inclusive dates)
AFIT Thesis

5. AUTHOR(S) (First name, middle initial, last name)
Jarcy, Jerome R., Captain, USAF

6. REPORT DATE	7a. TOTAL NO. OF PAGES	7b. NO. OF REFS
June 1967	146	43

8a. CONTRACT OR GRANT NO. N/A b. PROJECT NO. N/A c. d.	9a. ORIGINATOR'S REPORT NUMBER(S) AFIT Thesis GAM/ME/67-10 9b. OTHER REPORT NO(S) (Any other numbers that may be assigned this report) N/A

10. DISTRIBUTION STATEMENT

11. SUPPLEMENTARY NOTES	12. SPONSORING MILITARY ACTIVITY Thermo-Mechanics Laboratory Aerospace Research Laboratories Wright-Patterson AFB, Ohio 45433

13. ABSTRACT

In this study flow field, drag, and heat transfer characteristics of a mica cylinder heated by nichrome ribbon were investigated. Measurements were performed in a wind tunnel at velocities of 40 to 160 fps, and at heat input rates of zero to 188 Btu/hr-inch^2. Average cylinder surface temperatures ranged from 250 °F to 1100 °F above atmospheric temperature. Cylinder surface pressure distributions indicate the flow is subcritical and separation is laminar. Pressure drag was satisfactorily calculated from cylinder pressure distributions. Total and dynamic pressure distributions in the wake showed an increased depression with increased rate of heat input. Heat transfer data correlated satisfactorily with Douglas and Churchill.

DD FORM 1 NOV 65 1473

UNCLASSIFIED

Security Classification

UNCLASSFIED

Security Classification

14. KEY WORDS	LINK A		LINK B		LINK C	
	ROLE	WT	ROLE	WT	ROLE	WT
Fluid Flow						
Gas Flow						
Incompressible						
Subsonic						
Two Dimensional						
Wake						
Drag						
Heat Transfer						
Cylinders						
Crossflow						

UNCLASSFIED

Security Classification